Characterizing Petrophysical Properties of Carbonate Rocks Using Nuclear Magnetic Resonance and Complex Conductivity

By

Fan Zhang

Submitted to the graduate degree program in Geology and the Graduate Faculty of the University of Kansas in partial fulfillment of the requirements for the degree of Master of Science.

_____

Committee Chair: Dr. Chi Zhang

_____

Dr. Eugene C. Rankey

_____

Dr. Georgios Tsoflias

Date Defended: 6/17/2019

The Thesis Committee for Fan Zhang

certifies that this is the approved version of the following thesis:

Characterizing Petrophysical Properties of Carbonate Rocks Using Nuclear Magnetic Resonance and Complex Conductivity

_____

Committee Chair: Dr. Chi Zhang

_____

Dr. Eugene C. Rankey

_____

Dr. Georgios Tsoflias

Date approved: 6/17/2019

Abstract

Carbonate rocks are well known for their highly complex petrophysical behaviors due to their intrinsically heterogeneous pore geometry and wide range of pore sizes. As a result, both effective characterization of carbonate pore systems and the prediction of fluid transport in carbonate reservoirs, remains challenging. This thesis focuses on using nuclear magnetic resonance (NMR) and complex conductivity to quantify carbonate pore structure and gain insights into fluid flow and lithology of carbonate reservoir rocks at the core and log scales. In the laboratory study, integrated NMR and complex conductivity data are used to characterize porosity, pore size distribution, and surface area-to-pore volume ratio, in grainstones, packstones, and mudstones from carbonate reservoirs in Kansas. Carbonate samples with varying pore types and depositional texture are characterized according to NMR porosity, log-mean of transverse relaxation time (T_2) value T_{2ML}, real conductivity σ', and imaginary conductivity σ''. Widely used petrophysical relationships derived from NMR and complex conductivity data also are assessed, and alternative relationships appropriate for carbonate samples at laboratory scale are proposed.

Furthermore, to test the proposed petrophysical relationships at a larger spatial scale, and to exploit the potential of borehole NMR data, this study analyzes NMR well log data from Wellington, KS. This study focus on the uses of NMR longitudinal and transverse relaxation time ratio (T_1/T_2) in electrofacies characterization. Through multivariate analysis of a suite of logs (e.g., sonic slowness, photoelectric factor, etc.), the results show that T_1/T_2 ratio is uncorrelated with other logs which makes it a potentially independent indicator for rock typing. The data bear on the accuracy of predicted electrofacies using T_1/T_2 ratio, and how factors such as lithology and fluid could impact the T_1/T_2 ratio.

Extending beyond experimental observations, this work assesses and proposes new electrical and NMR petrophysical models, analyzes the factors controlling the variation within NMR logging data, and harnesses the complete NMR logging information to improve carbonate reservoir characterization. This work demonstrates the potential of combining NMR and electrical methods to advance understandings of fluid distribution and fluid flow in complex carbonate reservoirs.

Acknowledgments

First, I thank my advisor, Dr. Chi Zhang, as she provided enormous support and unwavering guidance during my graduate study. She provided me with experiences and training that have built my perspectives about academia and science. She never stopped encouraging me to continue perfecting my thesis and brought me back from the depth of decompression.

I also would like to thank my committee members: Dr. Eugene Rankey and Dr. Georgios Tsoflias. They both provided fundamental and essential comments and suggestions for improving my research and thesis writing.

I thank Dr. Qifei Niu (University of Kansas) for fruitful opinions and comments regarding experimental setting, data processing and paper writing, Dr. Lynn Watney (Kansas Geological Survey) for providing geological background about carbonate diagenesis and Dr. John Doveton (Kansas Geological Survey) for providing well data of Wellington KGS 1-32 and instructions of mathematical processes for petrophysics. A special thanks goes to students of GEOL535 for testing 12 grainstone samples. And a special credits to James Colgin for part of the CT images and digital rocks. I thank University of Kansas New Professor Funding, University of Kansas Summer Research Funding, GSA graduate student research grant and AAPG Jon R. Withrow Named Grant for supporting our research.

Finally, I thank my family and friends for their unconditional support and my significant other, Wenting, for her unfaltering emotional support and accompanies within these four years and the young ages before.

Table of Contents

Abstract ..... **iii**
Acknowledgments ..... **v**
Table of Contents ..... **vi**
List of Figures ..... **viii**
List of Tables ..... **x**
Chapter 1. Introduction **1**
Chapter 2. Geological Settings of Core Samples and Well Logs **4**
Arbuckle Group 5
Lansing-Kansas City Group 6
Chapter 3. Methodology **8**
NMR Principles 8
SIP Principles and Petrophysical Relationships 10
Permeability 12
Permeability from SIP *14*
Electrofacies 15
Step 1: PCA *19*
Step 2: Clustering *21*
Step 3: Classification *24*
Chapter 4. Core plug analysis **26**
Material and Methods 26
Sample description and preparation *26*
Geophysical measurements (NMR, SIP) *27*
Results and Discussion 28
μCT image and BET surface area *28*
Characteristics of NMR porosity and $T2$ *distribution* *29*
Characteristics of complex conductivity spectra *32*
Petrophysical properties derived from NMR and SIP *34*
a. Pore-size distribution and characteristic pore size 34

b. $Spor$ 36
c. Porosity exponent *m* from Archie's law 38
d. Permeability 40
The complexity of the pore system in carbonate *42*

Chapter 5. Logging data analysis 46
Lithofacies from core description 46
Data from NMR log 47
$\boldsymbol{T1/T2}$ ratio – a petrophysical property indicator 47
Electrofacies Classification 49
PCA *49*
Cluster Analysis *51*
Classification *52*
Predicted Electrofacies *53*
Discussion 54
Impact of lithology on $\boldsymbol{T1/T2}$ *54*
Impact of fluid on $\boldsymbol{T1/T2}$ *56*
Other controls that may fail electrofacies recognition *58*

Chapter 6. Conclusion 60
Core Analysis 60
Well Log Analysis 61

References 64
Figures 77
Tables 108

List of Figures

Figure 2.1- Dynamic well top map for Arbuckle Group

Figure 2.2- Dynamic well top map for Lansing-Kansas City Subgroup

Figure 4.1- μ-CT images of four samples

Figure 4.2- The relation between helium and NMR porosity

Figure 4.3- The T_2 distribution from NMR

Figure 4.4- The relation between NMR porosity and T_{2ML}

Figure 4.5- The frequency-dependent phase shift spectrum from SIP

Figure 4.6- The frequency-dependent complex conductivity spectrums from SIP

Figure 4.7- The pore size distribution from NMR

Figure 4.8- The relation between NMR porosity and S_{por}

Figure 4.9- The relation between S_{por} and σ''

Figure 4.10- The relation between S_{por} and $\sigma'' \cdot F$

Figure 4.11- Comparison between measured F and Archie's law with different m

Figure 4.12- The relation between NMR porosity and m

Figure 4.13- The relation between k_{air} and σ'

Figure 4.14- The relation between k_{air} and σ''

Figure 4.15- Comparison between k_{air} and k_{K-C}

Figure 4.16- The cross plot of k_{air} versus NMR porosity superimposed with T_{2ML}

Figure 5.1- Lithofacies, corresponding T_2 and T_1 distributions for a selected interval

Figure 5.2- $U_{maa} - \rho_{maa}$ crossplot superimposed with T_1/T_2

Figure 5.3- $U_{maa} - \rho_{maa}$ - T_1/T_2 3-D plot superimposed with GRTO and CT90

Figure 5.4- Pareto plot for PCA

Figure 5.5- Score plot of PCA superimposed with depth

Figure 5.6- Updated score plot with clusters and cluster centers

Figure 5.7- Comparison between geologic lithofacies and eletrofacies

List of Tables

Table 4.1- Sample information

Table 4.2- The general geophysical data of all samples

Table 4.3- The petrophysical properties that measured or calculated in this work

Table 5.1- Average values of calculated log responses

Table 5.2- Correlations, eigenvalues and variances of all principal components

Chapter 1. Introduction

Pore characteristics (such as porosity, size distribution, surface area, type, shape, and connectivity) are fundamental to understanding the subsurface heterogeneity and constituent fluid flow in reservoir rocks. Applied hydrogeologic and energy industry needs require predicting fluid transport and chemical component exchange in the pore systems of both saturated consolidated reservoir rocks [*Burdine*, 1953; *Johnson et al.*, 2006; *Katz and Thompson*, 1986] and unsaturated soils [*Mualem*, 1976; *Van Genuchten*, 1980]. Pore systems in complex carbonate rocks remain less understood, though expanding our knowledge in this area has the potential to improve subsurface modeling and carbonate reservoir evaluation.

Previous studies have applied a variety of conventional techniques to porous media to qualitatively and quantitatively characterize the pore size of complex geological materials. The first category is direct imaging, including optical microscopy, electron microscopy [*Curtis et al.*, 2010; *Ruppert et al.*, 2013], and X-ray computed tomography (CT) [*Bultreys et al.*, 2016; *Milliken and Curtis*, 2016; *Van Geet et al.*, 2000]. Using these direct imaging methods, studies have examined pore systems and the surrounding matrix visually, though these methods are only qualitative, and some (such as CT) requires highly complicated processes [*Lin et al.*, 2016; *Loucks et al.*, 2012; *Menke et al.*, 2016; *Milner et al.*, 2013].

The second category to characterize pore size is indirect fluid intrusion, including mercury intrusion capillary pressure (MICP) to provide pore-throat size distribution [*Abell et al.*, 1999; *Diamond*, 2000; *Hinai et al.*, 2014], and low-temperature gas adsorption (N_2, Ar, CO_2), which provides pore-size distribution and surface area [*Chalmers et al.*, 2012; *Clarkson et al.*, 2013; *Gregg et al.*, 1967; *Gun'ko et al.*, 2007]. Fluid intrusion measures the bulk properties of pores, as the volume of intruded fluid is correlated to pore abundance. Using such techniques,

quantifications of pore size are derived from empirical or theoretical models that link the intrusive behavior to pore shape and the physicochemical properties of the pore-solid interface. However, for geologic materials with a broad range of pore sizes, such as carbonate rocks, fluid intrusion commonly fails to address and analyze the complex pore systems appropriately.

Carbonate rocks, an important type of reservoir rocks, account for 40% of the total oil and gas production in the world [*Akbar et al.*, 1995], and 25% of the world and 40% of the US groundwater resources [*Ford and Williams*, 2007]. Yet, problems persist regarding the evaluation of extraction of hydrocarbon and groundwater from carbonate reservoirs. Unlike siliciclastic rocks, which mostly include intergranular pores, carbonate rocks can have a variety of pore types, including interparticle, intraparticle, moldic, fracture, shelter and other touching and non-touching vuggy pores [*Lucia*, 1983; 1995]. The intrinsically heterogenous spatial distribution of pores and wide range of pore sizes in carbonate rocks make the behavior of these systems hard to predict and commonly cause issues in reservoir evaluation and management. Previous research shows that pore attributes in carbonates impact petrophysical properties [*Anselmetti and Eberli*, 1999; *Melim*, 2001], and play an essential role in permeability estimation [*Anselmetti and Eberli*, 1999]. However, it is well-known that the porosity-permeability correlations of carbonate are distinct from those in siliciclastic rocks [*Lucia*, 2007] due to variable diagenetic overprinting that unique in carbonate rocks [*Choquette and Pray*, 1970].

Geophysical methods commonly are used to infer subsurface properties at large spatiotemporal scales. Realization of the importance of nanometer and micron-scale properties has led to increasing interest in using geophysical methods to estimate pore attributes. Recently, low-field NMR and complex conductivity or spectral induced polarization (SIP) measurements have been applied to characterize subsurface and borehole hydrogeological characteristics, especially

fluid flow properties (e.g., for reviews, see *Behroozmand et al.* [2015] and *Falzone et al.* [2018]). NMR directly measures hydrogen abundance in pore fluids and characterizes the physiochemical environment of hydrogen in the sample. For fully saturated porous media, the NMR relaxation time is proportional to pore size. Therefore, the relaxation time distribution can be used to calculate a pore-size distribution. Porosity and pore-size distribution have also been used to predict permeability of geologic materials using calibrated NMR parameters. For a comprehensive review of the application of NMR in petrophysics, the reader is referred to *Coates et al.* [1999] and *K-J Dunn et al.* [2002].

Extending the widely applied DC-resistivity tool, SIP has been used to measure the frequency-dependent dielectric response of applied electric fields in porous media at low frequencies. SIP is sensitive to geometries of the pores and variations in the physiochemical properties of solid-fluid interfaces in porous media. SIP has also been reported to be a valid tool for estimating permeability and texture heterogeneity [*A. Revil and Florsch*, 2010] in both conventional and unconventional reservoirs. Joint use of NMR and SIP provides an advantage in characterizing porous media and has shown promise for predicting petrophysical properties such as surface area-to-pore volume ratio and permeability of sandstones [*Niu and Revil*, 2015; *Niu and Zhang*, 2018a; *Andreas Weller et al.*, 2010a; *Zhang et al.*, 2018]. However, the applicability of such geophysical methods to carbonates is far from understood, and many challenges related to the complex pore attributes of carbonates remain.

This study aims to introduce an integrated method combining both NMR and SIP to quantitatively characterize the pore structure of carbonates and gain insights into fluid flow and lithology of carbonate reservoir rocks at the core and log scales. At the core scale, this study examines three types of carbonate rocks - grainstone, packstone, and mudstone from carbonate

reservoirs in Kansas. This study assesses widely-used NMR and SIP petrophysical relationships, and proposes new relationships applicable to carbonate rocks. At the larger spatial scale, it tests the proposed petrophysical relationships to examine the potential of NMR well-logging data in a cherty dolomite reservoir of Arbuckle, southern Kansas, with the aim of exploring the feasibility and sensitivity of using T_1/T_2 ratio as a lithology indicator for characterizing electrofacies subclasses within these carbonates.

By combining different geophysical techniques, this study advances understanding of the complex structure and pore networks of carbonate rocks and how these pore attributes affect the geophysical response at the core and well-log scales. The results also reveal the full potential of NMR logging data in characterizing petrophysical properties of reservoir rocks, aspects that have traditionally been overlooked. These results are essential for accurate interpretations of borehole geophysical measurements into carbonate reservoirs properties.

Chapter 2. Geological Settings of Core Samples and Well Logs

The Lansing-Kansas City Group, Mississippian System, and the Arbuckle Group are three important carbonate reservoirs in Kansas and have produced oil since the early 20th century [*Evan K Franseen*, 2006; *Evan K Franseen et al.*, 2003]. Due to the long production history of these sites, core analysis extends back to the 1950s, yet these data are poorly preserved and insufficiently cover the production area. Modern geophysical tests on cores are an essential component in reservoir characterization and are vital for engineering projects like CO_2 injection at Wellington Field, where geophysical data are used to refine models to predict CO_2 sequestration and evaluate the effectiveness of CO_2 storage and incremental oil recovery.

Arbuckle Group

The Cambrian-Ordovician Arbuckle Group is part of the Sauk Sequence [*Sloss*, 1964] developed in the southern Great American Carbonate Bank. The Arbuckle and its equivalent spans areas in Texas, Oklahoma, Arkansas, and Kansas. Locally in Kansas, the Arbuckle Group overlies an unconformity on Precambrian or Cambrian rocks, and is overlain by another regional unconformity [*Evan K Franseen et al.*, 2003].

The Arbuckle Group rocks are described as deposits with cyclicity [*Barwick*, 1928; *Cole*, 1975; *Zeller*, 1968] and the cyclical deposition of Arbuckle Group is reflecting a repeated change of depositional environment from shallow subtidal to peritidal facies (Franseen, 1994). Over hundred of meter-scale peritidal cycles stacked to form up to 420 m thick successions of carbonate in Kansas. The depositional facies of Arbuckle Group are skeletal, oolitic, intraclastic packstone to grainstone and wackestone to mudstone [*E. K. Franseen*, 2000]. The primary porosities formed during deposition comprise intercrystalline porosity and interparticle porosity.

Dolomitization and recrystallization of dolomite happened simultaneously which either enhanced or occluded the porosity. Prolonged periods of subaerial exposure also created a vast system of dissolution features and breccia, aspects which complicate the pore attributes of the Arbuckle Group. Together, these comprehensive diagenetic overprints induce difficulties in reservoir characterization. For example, *Evan K Franseen et al.* [2004] and *Zhang et al.* [2017] showed that permeability could vary by at least two orders of magnitude for a given porosity, an observation interpreted as the result of lithologic variations, including change of pore size distribution, and interlaminated lithologies.

Well-log part of this study centers on Wellington field which has 135 wells with logs, and two pioneer wells for CO_2 sequestration. The Arbuckle Group is the targeted injection zone of the

CO_2-Enhancing Oil Recovery (EOR) project [*Holubnyak et al.*, 2017], and locally has high porosity and permeability. It is capped by the Simpson Group, which includes shale with low porosity and permeability.

Logging data used in this study is from the Wellington KGS 1-32, in Sumner County, Kansas. This well was drilled to a total depth of 5240 ft and included a suite of modern geophysical logs, including neutron, density, self-potential, resistivity, conductivity, photoelectric, caliper, gamma-ray, sonic slowness, microlog lateral and normal, and NMR imaging logs. Ten core samples from the same well (Wellington KGS 1-32) are tested for the core analysis part of this study.

Lansing-Kansas City Group

The Lansing-Kansas City Groups are part of the Missourian stage, Upper Pennsylvanian series, and occor throughout Kansas [*Watney et al.*, 2001]. Observations of the Lansing-Kansas City Group in Kansas reveal the units display cyclical depositional patterns [*R C Moore*, 1949; *Watney*, 1980; *Watney et al.*, 1989]. These cycles display depositional environments ranging from shallow-water, high-energy oolitic shoals (the focus of this study), low-energy marine environment, to offshore deepwater environment. These strata document rapid changes of sea level that caused transgression and regression, reflected in the interbedded limestone and shale of the Lansing-Kansas City Group. In a typical cyclothem of Lansing-Kansas City Group [*Heckel and F. Baesemann*, 1975], the shoal limestones locally are oolitic grainstones and skeletal grainstones.

Extensive freshwater diagenesis significantly modified the oolitic and skeletal grainstones during subsequent subaerial exposure [*Watney*, 1980]. Partial dissolution forms secondary moldic pores that preserve the original shape of ooids and skeletons, but provides ample pore space. Micro-fracturing also had a positive influence on porosity [*Watney*, 1980].

The oolitic grainstones, a major lithology of interest in this study, are a common reservoir rock among prolific pay zones in Kansas [*Watney and Paul*, 1983] due to the high porosity preserved in the moldic pore system. However, the relationship among porosity, permeability and petrophysical properties in oomoldic carbonate still is studied insufficiently, and varies case by case [*Jewett and Merriam*, 1959].

Core plug samples of the Lansing-Kansas City Group for this study are extracted from 20 wells at various locations in western Kansas (Figure 2.2). Wells are spudded in a broad range of time period from 1921 to 1985 but are all plugged from 1985 to 1989. These Lansing-Kansas City Group wells are all productive, but have distinctive porosity (3 – 36%) and permeability (0.01 – 1500 mD), due to the varied facies and diagenesis [*Watney*, 1980].

Chapter 3. Methodology

NMR Principles

Nuclear magnetic resonance (NMR) is a well-known, non-destructive method to determine physiochemical environments of pores in geologic media. In the past few decades, NMR has been successfully applied to well-logging and laboratory work to estimate petrophysical properties of reservoir rock such as porosity, pore size distribution, and permeability (for detailed reviews, see *Coates et al.* [1999] and *K-J Dunn et al.* [2002]).

The fundamental physical principles of NMR are based on an understanding of the perturbation of the alignment of magnetic nuclear spins in a static magnetic field ($\boldsymbol{B}_0$), resulting in a net nuclear magnetization (M). After the alignment to the static magnetic field, nuclei spins can be tipped by an external radiofrequency (RF) magnetic field ($\boldsymbol{B}_1$) out of alignment, which forces the nuclei to precess in phase with each other. Irradiation of resonant $\boldsymbol{B}_1$ results in a decrease in longitudinal magnetization (M_z) and generation of transverse magnetization (M_{xy}) [*Simpson and Carr*, 1958]. For core plug samples (as used here), the transverse (T_2) relaxation time usually is measured using a Carr-Purcell-Meiboom-Grill (CPMG) pulse sequence [*Carr and Purcell*, 1954; *Meiboom and Gill*, 1958]. The amplitude of the transverse magnetization $M_{xy,}$ is a function of transverse relaxation time (T_2) as shown here:

$$M_{xy}(t) = M_{0,xy}e^{-\frac{t}{T_2}}, \tag{1}$$

where t is the time for one pulse train, $M_{0,xy}$ is the magnitude of the transverse magnetization at t = 0 and is proportional to the total volume of hydrogen nuclei. Thus $M_{0,xy}$ can be scaled to provide the total fluid content and equivalent porosity.

The T_2 relaxation time distribution is obtained through an inversion process solving the exponential equation. The relaxation time T_2 is consist with three components linked to three different mechanisms [*Kleinberg et al.*, 1994; *Westphal et al.*, 2005]:

$$\frac{1}{T_2} = \frac{1}{T_{2B}} + \frac{1}{T_{2S}} + \frac{1}{T_{2D}} = \frac{1}{T_{2B}} + \rho_2 \frac{S}{V} + \frac{1}{12}(T_E \gamma G)^2 D_0, \quad (2)$$

where the subscripts *B*, *S*, *D* represent bulk fluid (free fluid) relaxation, surface relaxation, and molecular diffusion, respectively, ρ_2 is the surface relaxivity corresponding to the capability of relaxation enhancement on the surface, *S* and *V* refer to the surface area and volume of pore space, respectively, T_E is the interval echo time of the CPMG sequence, γ is the gyromagnetic ratio of the hydronic nuclei (which is constant and depends on fluid types), G is the effective magnetic field gradient, and D_0 is the molecular diffusion coefficient of the adsorbate.

Bulk fluid relaxation time is the transverse relaxation time of fluid in a bulk state. For water, the bulk relaxation time is a temperature-dependent and salinity-independent constant of 3.82 s at 30 ℃ [*Simpson and Carr*, 1958]. In geologic material, it generally is assumed that relaxation occurs in fast relaxation regime, in which the relaxation at the surface is slower than the transport of hydrogen nuclei to the surface, i.e., the bulk fluid relaxation $\frac{1}{T_{2B}}$ is $\ll \frac{1}{T_{2S}}$, and is negligible. Similarly, the inhomogeneities in the magnetic field can be ignored as well [*Latour et al.*, 1993], i.e., $\frac{1}{T_{2D}} = 0$. As a result, T_2 relaxation time can be expressed as a function of only surface relaxation:

$$\frac{1}{T_2} \approx \frac{1}{T_{2S}} = \rho_2 \frac{S}{V} = \rho_2 \frac{a}{\Lambda}, \quad (3)$$

where a is the dimensionless geometry related factor, which equals to 1 for tabular pores, 2 for cylindrical pores and 3 for spherical pores. Λ is the characteristic size of pore space, for example, in samples with just spherical pores, Λ is the radius of the pore body. Therefore, T_2 is proportional

to the surface area to volume ratio (S/V, presented as $S_{por,}$ below) and characteristic pore size. The S_{por} is an important quantity as it contains information of pore shapes and texture features [*Santamarina et al.*, 2002; *Wadell*, 1932] and can be related to electrical properties like surface conductance [*Slater et al.*, 2006] and tortuosity. Equation 3 is the basis of determining $S_{por,}$ pore size distribution, and permeability and relies on the accurate acquisition of surface relaxivity (ρ_2). The methods of obtaining ρ_2 include 1) calibrating T_2 relaxation time using mercury intrusion [*Kenyon et al.*, 1989; *Morriss et al.*, 1993] and 2) calculating ρ_2 using T_2 multiplied by S_{por} generated from gas adsorption experiments. The limitation of ρ_2 determination and the pre-assumptions used in deriving pore-size distributions will be discussed later.

SIP Principles and Petrophysical Relationships

Spectral induced polarization (SIP) or complex conductivity is a geophysical measurement probing the low-frequency electrical polarization mechanisms in porous media [*A. Revil and Florsch*, 2010]. Extending from bulk resistivity of porous media measured using DC-resistivity, SIP also is sensitive to capacitive properties of the mineral grain-fluid interface. The induced polarization phenomena is observed as the voltage between two potential electrodes do not promptly drop to zero. The measured complex conductivity $\sigma^*(\omega)$ is controlled by both the ionic conduction (σ') and polarization σ", and the latter is related to electrochemical and geometrical properties at the rock-fluid interface. The complex electric conductivity can be described as:

$$\sigma^*(\omega) = \frac{1}{\rho^*(\omega)} = \sigma'(\omega) + \sigma"i(\omega) \quad (4)$$

where, $\rho^*(\omega)$ is the frequency-dependent resistivity, ω is the angular frequency as $\omega = 2\pi f$, f is the frequency with a unit of Hz, and i is the imaginary number. The SI unit for conductivity is S/m.

The magnitude of conductivity $|\sigma|$ and the phase shift φ can be calculated from the real and imaginary part of conductivity by the equation:

$$|\sigma| = \sqrt{\sigma^{*2}} = \sqrt{\sigma'^2 + \sigma''^2} \tag{5}$$

and,

$$\tan\varphi = \frac{\sigma''}{\sigma'}. \tag{6}$$

The empirical Archie's law [*Archie*, 1942] has been widely used to relate the electrical conductivity of rock to porosity by

$$\sigma_0 = \frac{1}{F}\sigma_f, \tag{7}$$

where σ_f is the conductivity of saturating fluid and σ_0 is the bulk conductivity of the brine-saturated samples. F is the formation factor. $F = \varphi^{-m}$, where φ is porosity and m is Archie's porosity exponent ranging from 1.5 to 2 for most consolidated sandstones. However, m varies from 1.3 to larger than 4 in carbonates with complex pores, as m is sensitive to the geometry and roughness of grains and pores. The formation factor represents the geometry of the interconnected electrical field, which is comparabe to the pathway of hydraulic flow [*A. Revil et al.*, 2014b].

The classic form of Archie's Law ignores the electric conduction on the mineral surface, as it was developed using sandstone samples saturated at high salinities. This approximation might not be valid for clay-rich limestone or sandstone, where the effect of surface conductance dominates the conductivity at low salinities. If so, the F defined by Archie's procedure [*Archie*, 1942] underestimates the actual formation factor [*Andreas Weller et al.*, 2010a; *A. Weller et al.*, 2010b]. Waxman and Smits (1968) have developed an extended model for clay-rich sandstone that includes clay exchange cation-related conductivity σ_e:

$$\sigma_0 = \frac{1}{F}(\sigma_f + \sigma_e). \quad (8)$$

Subsequent studies have derived the equations with consideration of surface conductivity. The real [*Vinegar and Waxman*, 1984] and imaginary [*Börner et al.*, 1993] part of conductivities can be written as:

$$\sigma' = \frac{1}{F}\sigma_f + \sigma_s', \quad (9)$$

$$\sigma'' = \frac{1}{F}S_{por}\Sigma_{sn}''. \quad (10)$$

Here, σ_s' is the real part of surface conductivity and Σ_{sn}'' is the imaginary part of normalized surface conductance (sometimes called specific surface conductance [*Niu et al.*, 2016]). The normalized surface conductivity mainly depends on the charge density and capacity of an electrical double layer (EDL) formed at the mineral-fluid interfaces. The intrinsic *F* can be estimated only by fitting the slope of the Equation 9 with data points measured at multiple pore-fluid salinities.

Permeability

Well-designed experiments and petrophysical models involving pore attributes have been used to address the fundamental challenges of predicting permeability *k* from petrophysical properties such as porosity. A commonly used equation is the semi-empirical Kozeny-Carman (K-C) model, developed by *Kozeny* [1927] and modified by *Carman* [1937]. This model can be expressed as:

$$k_{K-C} = \frac{\varphi^3}{\tau {S_{por}}^2 (1-\varphi)^2}, \quad (11)$$

where φ is the total porosity, τ is the tortuosity, S_{por} is the surface area to volume ratio. This model has shown excellent agreement with measured permeability for many reservoir rocks [*Guo*,

2012; *Johnson et al.*, 2006; *C H Moore*, 2001; *P Xu and Yu*, 2008], even as its parameters remain complex.

Among all the parameters of the K-C equation, tortuosity τ has been recognized as an important metric that describes the geometric complexity and macroscopic permeability of porous systems [*Dullien*, 1975; *Johnson et al.*, 2006; *Nashawi and Malallah*, 2009]. The tortuosity τ is defined as the ratio between the distances that fluid actually travels, owing to the curvature and connectivity of pore spaces, and the length of the straight line between entry- and exit-points of a pore space. In general, tortuosity depends on numerous factors, including sorting, packing, grain shape and size, pore shape and size, as well as the spatial distribution of pores and grains [*Barrande et al.*, 2007; *Guo*, 2012]. By definition, τ can be categorized in many different ways. This work defines the hydraulic tortuosity in the Kozeny – Carman equation [*Carman*, 1937] as the square of the ratio of the effective length of the hydraulic pathway (L_a) to the distance through the straight line of two points (L) in the direction of flow, or:

$$\tau = \left(\frac{L_a}{L}\right)^2, \tag{12}$$

Therefore, under the assumption that rock resistance R_o is roughly equal to fluid resistance R_w, the formation factor F can be calculated from τ and porosity:

$$F = \frac{\rho_o}{\rho_w} = \frac{R_o \frac{A}{L}}{R_w \frac{A_{por}}{L_a}} \approx \frac{\sqrt{\tau}}{\varphi}, \tag{13}$$

where A and A_{por} are the total, and pore space cross-section area, ρ_o and ρ_w, are the reservoir and fluid resistivity. The equations 11 and 13 show that permeability estimation from resistivity measurement is feasible.

Permeability from SIP

Following the pioneering work of Kozeny and Carman, numerous studies experimentally or theoretically estimated the permeability of porous media from pore space attributes like porosity, geometry, and size of pores and particles. Permeability can also be estimated using geophysical measurements such as electrical resistivity and SIP with the principle of estimating the effective pore size or hydraulic tortuosity from geophysical parameters such as imaginary conductivity, formation factor.

This study applies the modified K-C equation (following *Katz and Thompson* [1986]) which links the electrical conductivity of bulk (σ') and fluid (σ_f) to permeability k via a characteristic pore size $d_c$as:

$$k = cd_c^2 \frac{\sigma'}{\sigma_f}, \tag{14}$$

where c is the Kozeny constant. *Katz and Thompson* [1986] define the d_c as a percolation threshold, where a pore system becomes interconnected. In other studies [*Barrande et al.*, 2007; *Johnson et al.*, 1986], the dynamic pore size Λ (also in units of meters or micrometers) was introduced to replace d_c to represent dynamically connected porosity. Assuming cylindrical pores, Equation 14 can be expressed by Λ as:

$$k = \frac{\Lambda^2}{cF}. \tag{15}$$

In practice, this Λ can be derived from pore-throat size distribution from an MICP test [*Johnson et al.*, 1986; *A. Revil et al.*, 2014b]. This study uses the characteristic pore size deterimined from NMR as Λ, and constant c = 8 [*A. Revil and Florsch*, 2010].

Electrofacies

Petrophysical properties such as porosity, saturation, and permeability can be derived from well log responses, and represent the critical inputs of rock typing and subsurface geologic models [*Busch et al.*, 1987; *Delfiner et al.*, 1987]. Numerous logs, each providing distinct information on the reservoir, can be grouped or clustered to define electrofacies. These logs include environment logs, lithology logs, porosity logs, resistivity logs. Environment logs are the basic logs available to provide information of borehole environment for production efficiency and safety and include temperature log, pressure log, caliper log, fluid condition monitoring log, noise log, etc. Beyond allocating production, temperature and caliper logs are also utilized for porosity and resistivity log quality control. Apart from the environment control, the identification and discrimination of lithology from logging is crucial to reservoir evaluation as the log responses reflect the mineralogical and physical properties of the subsurface. For the detailed principle and development of each logging tool, the reader is referred to *Ellis and Singer* [2007].

The most informative lithology log is spectral gamma ray (SGR), which is based on the gamma-ray response to identify clay minerals from radioactivity emitted by isotopes of potassium, thorium, and uranium (K, Th, and U, respectively) series. Since the uranium sometimes is high in minerals other than clays (for example, in dolomite), calibrated gamma-ray reading (CGR) which only includes potassium and thorium is used more commonly in determining clay content. Units with high CGR suggest shaly lithofacies and low permeability zones, whereas low CGR commonly indicates clean sandstone or carbonate. The GR log usually is analyzed together with additional logs like density log, neutron log, or sonic slowness.

Like the GR log, both density and neutron logs are nuclear tools responding to gamma-ray scattering and neutron scattering effects caused by the formation matrix and pore-filling fluids.

Porosity, bulk density and hydrogen content are the common outcomes of density and neutron logs. As a supplementary measurement of density log, photoelectric factor (PeF) provides a means to discriminate lithologies by analyzing the low-energy photoelectric (PE) absorption which is mostly independent of porosity. The sonic log is based on propagation of acoustic waves through the section. It not only is used for porosity estimation and cement volumetric evaluation, but is also combined with density to produce impedance logs and synthetic seismic profiles which can be used to correct depth and seismic travel times.

Resistivity is another petrophysical property that indirectly reflects the permeability and fluid saturation of reservoirs which is challenging to measure. To solve the challenge of accurate measurement, numerous resistivity and induction logs have been introduced in modern wireline logging probes, including microlog (ML), medium and deep resistivity (MRT/DRT), conductivity (90 inches conductivity (CT90) is used in this thesis) and spontaneous potential (SP). These logs measure the resistivity of mudcake, flushed zone, uninvaded zone and formation fluid respectively.

Additionally, recently developed electromagnetic logging tools provide additional information about pore structure and fluid type in the surrounding reservoir environment. Among those tools, magnetic resonance imaging logging (MRIL) has created excitement in the well logging community. Based on the same physical principles as its laboratory scale counterpart, MRIL is used in well logging to reveal total fluid-filled porosity, pore-size distribution, fluid types and fluid contents that can be used subsequently to determine permeability. Since the 1970s, important advances have been made in NMR wireline tools, the new acquisition schemes and processing methods significantly improved the data acquisition, data quality and resolution, as well as the data analysis and interpretation.

A lithofacies is a rock type distinct from adjacent rock types, as determined by its physical or chemical properties resulting from different facies, lithology, texture, and mineralogy. These lithofacies usually are interpreted in terms of environment of deposition and diagenesis. Although core data represent geological 'ground truth,' most wells are not cored and core data are sparse. However, most wells are logged with different tools. Early attempts in the early 1980s to predict lithofacies from log responses to augment core description used empirical geological facies-log response associations. Serra and Abbott (1982) developed the concept of electrofacies from well logs, as a measure to extend the petrophysical properties (e.g., porosity, permeability, saturation states) identified in the core to the well log. The electrofacies are defined as collective wireline logging responses that uniquely distinguish facies from one another. In many cases, such differentiations are robust as well log measurements are the direct reflection of facies characteristics and physiochemical properties of rocks. However, the correlation between rock physical properties and geology is non-unique. Electrofacies should match the lithofacies identified in the core if electrofacies are classified accurately and adequately [*J H Doveton*, 2014]. Numerous reservoir studies have illustrated the value and importance of electrofacies characterization for permeability estimation and improved reservoir characterization [*Ali et al.*, 2008; *Bucheb and Evans*, 1994; *Kim et al.*, 2005; *Lim et al.*, 2006; *Mathisen et al.*, 2001; *Perez et al.*, 2005; *Sharma et al.*, 2011].

Single variable methods generally are used for early stage and current electrofacies recognition. For example, *Flaum and Pirie* [1981] applied spectral gamma ray to quantitatively subdivide sandstone, clay, limestone in strata of the Cotton Valley Group (Jurassic) in eastern Texas, and *Lucia* [2007] successfully subdivided mud-supported carbonate and grain-supported carbonate in San Andres and Grayburg formations (Permian) in western Texas using computed

gamma-ray log (CGR). The major shortcoming of single variable analysis is that it is not applicable for clean reservoirs with no clay and complex lithofacies – like many sandstone and carbonate reservoirs.

In most strata, integrating more log responses is necessary for electrofacies recognition. Litho-porosity cross-plots like the M-N plot [*Burke et al.*, 1969], which combines neutron log, density log, and sonic log, are another frequently used electrofacies discriminator. Yet, in this approach, 'M' and 'N' are created parameters and produced without regard to any specific physical properties. To improve the litho-porosity method, [*Clavier and Rust*, 1976]) developed the matrix-identification (MID) plot, which is also called U_{maa} vs. ρ_{maa} plot. It uses two quasi-physical quantities: apparent matrix density (ρ_{maa}) in g/cc and apparent volumetric cross section of photoelectric absorption (U_{maa}) in barns/cc calculated by:

$$\rho_{maa} = (\rho_b - \rho_f \varphi_t)/(1 - \varphi_t) \tag{16}$$

$$U_{maa} = (PeF\rho_b - U_f \varphi_t)/(1 - \varphi_t) \tag{17}$$

where ρ_b is bulk density, ρ_f is fluid density, φ_t is true volumetric porosity, P_e is photoelectric absorption measurement, PeF is the photoelectric absorption factor, and U_f is the fluid volumetric photoelectric absorption. More recently, third-generation density logs (litho-density log) provide not only a bulk density (ρ_b) measurement but also the photoelectric measurement P_e, which reflects the average atomic number of the formation and is therefore a reliable indicator of the formation lithology [*Dewan*, 1983]. In carbonate reservoir logging analysis, and based on standard U_{maa} and ρ_{maa} values from various minerals, three end-member minerals (quartz, calcite, dolomite) can be plotted in a triangle on the U_{maa} and ρ_{maa} cross plot. End-member ρ_{maa} values for pure quartz, calcite, and dolomite are 2.65, 2.71 and 2.87 g/cc, respectively, whereas end-member U_{maa} for quartz, calcite, and dolomite are 4.78, 13.80 and 8.98 barns/cc, respectively [*Poupon et al.*,

1971]. The artificial or formalized parameters are defined to be independent of porosity [*J H Doveton*, 2014], however, if the pore characteristics dominate the log signals, the MID and U_{maa}-ρ_{maa} triangle approaches are less accurate.

To attain more representative electrofacies from well logs, an alternative method is proposed to use multivariate data analysis to correlate well-log responses with core descriptions. A multivariate data analysis is expected to improve petrophysical properties estimation by clustering the well-log responses with similar characteristics into groups (electrofacies). With the blooming of computational power, use of mathematical procedures and computer programs to automatically classify electrofacies from even more complex set of variables has become more common [*Bucheb and Evans*, 1994; *Busch et al.*, 1987; *Delfiner et al.*, 1987; *JH Doveton and Cable*, 1979; *Grimm*, 1987]. One of the complete multivariate statistical analysis includes analysis of variance, nonparametric regression, clustering, and classification. In this thesis, the analysis utilizes the following steps: 1. Principal component analysis (PCA); 2. Fuzzy c-mean clustering; and 3. Classification. First, PCA transforms well log data to scores, which are then subjected to model-based clustering, and to be used to categorize the scores into groups interpreted as electrofacies. The details of each step are discussed below.

Step 1: PCA

Principal component analysis (PCA) is a multivariate technique in which a number of related variables are transformed to set of uncorrelated variables [*Jolliffe*, 2011]. The greatest advantage of PCA is the simplification of data by reducing its dimensionality, and it facilitates extraction of the structure of variables. This procedure is important in modern well-log analysis as logging suites provide log responses that are closely correlated, which challenges the multivariate analysis.

For PCA, all logs first should be normalized with zero-score standardization, which subtracts the mean and standardizes data to unit deviation of each log to ensure the equal weight of each response. If n data points of m types of log responses form a $m \times n$ matrix X, the covariance matrix can be expressed as $S_x = \frac{1}{n-1} X^T X$. The variance of *i*th and covariance of the *i*th and *j*th principal components are:

$$var(y_i) = \beta_i^T \Sigma \beta_i = \lambda_i, \tag{18}$$

and

$$cov(y_i, y_j) = \beta_i^T \Sigma \beta_j, \tag{19}$$

where β is the coefficient and column eigenvector and λ is the eigenvalue. Therefore, the covariance matrix can be alternatively expressed as

$$S_x = \mathrm{B}^T \Lambda \mathrm{B}, \tag{20}$$

And the *i*th principle component can be described as

$$p_i = \sum_1^j \beta_{ij} x_i. \tag{21}$$

To achieve the reduction of dimensions, the reduced principal components should have the largest possible variance $var(y_i)$ and lowest covariance $cov(y_i, y_j)$, essentially equal to 0. In this data reduction, the number of principal components is less than the number of original variables. Based on different criteria of maximum variation of principle components, eigenvalues for two or more principle components could be projected to a two or more-dimension coordinate system, which is called score plot. In this study, the first two principle components (PC1, PC2) are selected to address score plot. Since most of the variability in the dataset is contained in the first two PCs, noise that collected in the observations can be extracted and eliminated from original data suite. However, even if well logs can be projected into uncorrelated variables, it is unrealistic to build

connections for principal components against actual physiochemical properties as opposed to what core descriptions and well-log responses can do.

Step 2: Clustering

By definition, clustering is any technique that involves the grouping of data. Cluster analysis is used as a primary stage for unsupervised learning to group the dataset into subsets in such a manner that similar instances are grouped, whereas different instances belong to different groups [*Rokach and Maimon*, 2005]. The purpose of the cluster analysis as used here is to separate the data from a suite of logs into meaningful groupings that can be interpreted in terms of electrofacies. Common clustering algorithms mostly use a hard boundary, which allows a component belongs to only one cluster, that can be divided to several subgroups, including centroid-based algorithms (K-mean clustering, mean-shift clustering), density-based algorithms (Density-Based Spatial Clustering of Applications with Noise (DBSCAN)), hierarchical development (hierarchical agglomerative clustering, depth-constrained hierarchical clustering), and neural network algorithms (see *Jain* [2010] for a review of details of current pattern recognition and clustering methods). Centroid-based algorithms are the most popular and well-known clustering methods due to their high efficiency and linear complexity. However, the cost of fast processing speed is that the number of centroids must be pre-assigned by the user, a situation which is not ideal. Centroid-based algorithms also start with unsupervised, random centroids, points which can drastically affect the final clustering result, and therefore lead to inconsistency, even among multiple analyses of the same data. Recently, approaches like DBSCAN and spectral clustering are designed to intentionally overcome the problems of imaging pattern recognition where the number of clusters represents previous information. Those algorithms fix the inherent disadvantages implemented by centroid-based algorithms as applied to large data set with irregular distribution and high standard deviations. However, since the underlying algorithms are intended

to be efficient for pattern recognition which is not associated with the physical model, these methods do not perform well if the clusters are not well separated, as is commonly the situation for lithofacies. Similarly, lithofacies with very similar petrophysical properties - like packstones and mudstones - are difficult to differentiate from the log responses, and usually overlap in the score maps. Therefore, hard boundaries are not preferred for electrofacies classification, instead, fuzzy-membership based algorithms have become popular in such circumstances.

Fuzzy c-means (FCM) is a method of centroid-based clustering which employs fuzzy membership and allows one data point to belong to many (or even all) clusters with degrees of membership from 0 to 1 (e.g., the total membership = 1) (*J C Dunn* [1973]. This method bloomed after being optimized by *Bezdek et al.* [1984], and is now a common algorithm in many pattern recognition analyses. A fuzzy c-mean process tries to minimize the primary objective function:

$$J_m = \sum_{i=1}^{N}\sum_{j=1}^{C} \mu_{ij}^{m} \left\| x_i - c_j \right\|^2, \tag{22}$$

where m is a real number $\in [1, \infty]$ called fuzziness index or factor, μ_{ij} is the degree of membership of x_i in the cluster j, x_i is the ith of measured data in Euclidean space, c_j is the center of the cluster in Euclidean space, and ||*|| is the Euclidean distance between data x_i and the cluster center c_j. Fuzzy partitioning is calculated by updating of fuzzy membership μ_{ij}

$$\mu_{ij} = \frac{1}{\sum_{j=1}^{C} \left(\frac{|x_i - c_i|}{|x_i - c_j|} \right)^{\frac{2}{m-1}}} \tag{23}$$

moreover, the cluster centers c_i by :

$$c_{ij} = \frac{\sum_{i=1}^{C} x_j \mu_{ij}^m}{\sum_{i=1}^{C} \mu_{ij}^m}. \tag{24}$$

Repeating above steps through an iterative operation until the minimum objective function J_m has been achieved or the termination criterion has been reached.

This study considers two-dimensional FCM analysis of PC1 and PC2, as derived from the log data. If only two possible electrofacies (A and B) have been assigned, a membership partitioning matrix for both k-means and FCM algorithm as M_{KM} and M_{FCM} includes:

$$M_{KM} = \begin{bmatrix} 0 & 1 \\ 0 & 1 \\ 1 & 0 \\ \vdots & \vdots \\ 0 & 1 \end{bmatrix}, \qquad M_{FCM} = \begin{bmatrix} 0.3 & 0.7 \\ 0.4 & 0.6 \\ 0.8 & 0.2 \\ \vdots & \vdots \\ 0.1 & 0.9 \end{bmatrix}. \tag{25}$$

Numbers indicate the degree of membership that belongs to each electrofacies. For sample 1 in the first row, a data point belongs exclusively to electorfacies B with a degree of membership equal to 1 in the k-means algorithm, whereas in the FCM algorithm it belongs to electrofacies A with a membership coefficient of 0.3 and belongs to electrofacies B with a membership coefficient of 0.7. As an outcome, every data point will have a membership partitioning for each cluster and that membership represents the possibility of belonging to a cluster. Instead of unitary distribution of such association, FCM allows a changeable clustering result by adjusting the membership threshold to each cluster and gives the best result for the overlapped dataset, commonly better than the k-means algorithm in recognizing members that belong to multiple groups [*Bezdek*, 2013]. For instance, mudstone, packstone, and grainstone can have very similar PC1 and PC2 values thus very close cluster centers. FCM, therefore, would be less possible to include a mudstone that surrounded by the packstone and grainstone in the score plot which is critical to the recognition of subclasses.

Step 3: Classification

The next step would be assigning lithofacies to clusters to make them meaningful electrofacies. This procedure is usually performed by either applying the lithofacies of centroid to the whole cluster universally [*J H Doveton*, 2014] or assigning lithofacies based on their corresponding logs and log interpretations [*Roslin and Esterle*, 2016]. However, those two methods are relying on 1) fairly large number of clusters, and 2) distinct log values among clusters and extensive understanding of these log values. These two conditions are not satisfied in this study since we are dealing with carbonate samples with fixed number of clusters and relatively small changes in log responses. To avoid human bias while assigning the lithofacies to clusters and make this interpretive procedure an unsupervised way, a more statistical way is then performed by minimizing the overall objective function, S:

$$S = \phi_m + \beta\phi_n \tag{26}$$

where, ϕ_m is the term of data misfit and $\phi_m = \sum_{i=1}^{n}\left(\frac{d_i^{elec} - d_i^{litho}}{\sigma}\right)^2$, d_i^{elec} and d_i^{litho} are the electrofacies and lithofacies for ith data point respectively, σ is the standard deviation of the dataset, and n is the total number of data points. ϕ_n is representing the model norm or regularizer and

$$\phi_n = \alpha\sum_{i=1}^{n-1}\left(d_{i+1}^{elec} - d_i^{elec}\right)^2 + (1-\alpha)\|misprediction\|_2^2 \tag{27}$$

Eletrofacies that are not matching lithofacies would be considered as '*mispredicted'* and therefore misprediction rate is simply equals to a number of mispredicted data points over the total number of data points. Therefore, ϕ_n contains the information of smoothness of rock type transactions and the success rate of prediction. Weighting parameter α and β are used to adjust

the weight among terms and can be optimized, α is the weight between the smoothness of rock type transactions and the success rate of prediction and β is the weight between data misfit and model norm.

Chapter 4. Core plug analysis

Material and Methods

Sample description and preparation

A total of fifty-one samples including Lansing-Kansas City Group oomoldic limestone plugs and Cambro-Ordovician Arbuckle Group carbonate plugs, were taken from wells in central and southern Kansas. *Evan K Franseen et al.* [2003]; *Watney* [1980] interpreted depositional environments of the Lansing-Kansas City Group and Arbuckle Group to range from subtidal to peritidal and to include grainstones, packstones, and mudstones. The pore types include interparticle, intraparticle, moldic, isolated vuggy and touching vuggy [*Lucia*, 1983; 1995], as related to depositional facies, early diagenesis, and dolomitization [*Evan K Franseen et al.*, 2004; *Watney et al.*, 1989].

The forty-one grainstone samples were oomoldic limestones with diameter ~ 1 inch, whereas five packstone and five mudstone samples were plugs of mostly dolomite and chert with diameter ~ 1.5 inches. Samples were extracted from drilling core samples continuously at 4-5 inch scales to have higher analyzing resolution than well-log data. The Arbuckle samples came with well-log data, which serve as reference data. All samples have lithofacies descriptions, effective helium porosities, and air permeability with Klinkenberg correction (K_{air}) from specific core analysis done at CoreLab and Weatherford. Additional experiments, including low-pressure gas adsorption porosimetry and X-ray microtomography (μ-CT) scanning, are performed for four samples (two grainsotnes, one packstone, one mudstone), and is described below.

Gas adsorption measurements were performed by the ASAP2020 Accelerated Surface Area and Porosimetry System (Micromeritics). The specific surface area (in units of area per unit of mass (m^2/g)) were determined by the low-pressure gas adsorption of nitrogen onto the surface

of powdered samples (0.3 mm) at cryogenic temperatures of nitrogen. Nitrogen was chosen due to its small molecular size, low boil temperature, and reasonable saturated pressure. Brunauer, Emmett, and Teller (BET) surface area analysis was completed in the linear region of the 10-points BET plot, which was evaluated systematically using the Rouquerol transform. Two grainstones, one packstone, and one mudstone, are selected to perform low-pressure gas adsorption. All samples are ground into 250-300 μm, and 0.8-0.9 g ground powder for each sample is used in the test.

To perform the μ-CT scanning, rock sticks were extracted from the four core plugs with dimensions of roughly 2 mm (length) by 2 mm (width) by 2 cm (height), chosen to achieve a high-resolution pixel size of 1.69 μm. Original μ-CT images were collected using a ZEISS Xradia 400 Versa μ-CT and post-processed using Avizo Fire to stack and reconstruct the grayscale 3-D digital data. For pore network separation and two-phase segmentation, a combined algorithm of manually picked threshold and watershed-based methods were applied on at 100*100*100 pixels. This Area of Interest (AOI) was applied to qualitatively differentiate pore space (deep color regions) from the matrix (light color regions). A minimum pore size of 3.38 μm (or minimum pore radius 1.69 μm) is the effective resolution limit of μ-CT. Therefore, the total pore volume determined by μ-CT and post-processes ignores pore space with radii smaller than 1.69 μm. Detailed information about our samples can be seen in Tables 4.1 and 4.2.

Geophysical measurements (NMR, SIP)

All samples were first oven dried at 70 ˚C for 72 hours and placed under a vacuum with specific saturation fluids to saturate the effective pore space. All samples were wrapped with Teflon tape to hold water and reduce background noise while performing the NMR tests. Samples analyzed by SIP were sealed with semi films and silicone gel to prevent dehydration, which could dramatically increase impedance.

Sodium-chloride brine concentrations for saturation were set as 0.01 mol/L, 0.03 mol/L, 0.11 mol/L, and 0.12 mol/L for different fluid salinities, in order to extract formation factor *F*. After saturation, all samples were kept in the same holder with saturation fluids to stabilize and normalize the conductivity (see Table 4.1). The sample holder for the SIP test was built as a modified Wenner array with Ag/AgCl electrodes according to *Binley et al.* [2005], the distance between two potential electrodes changes and is 0.0179 m plus the sample height. SIP data were collected using a Portable SIP meter (Ontash & Ermac, Inc.) over a frequency range from 0.01 Hz to 10k Hz to ensure the datasets could capture the SIP responses from a broad range of pore-size distribution, especially macropores. The lower detection limit of phase shift was approximately 0.2 mrad. The reference resistor at 10k Ohm was close to the same order of magnitude of the samples' impedance and provided an optimal signal to noise ratio. The value of the σ' spectra and σ"spectra in 1Hz frequency was used as the characteristic σ' and σ" value for the sample.

NMR measurements were performed by a 2MHz Rock Core Analyzer (Magritek Ltd) using CPMG pulse sequence with echo times of 300 μs and an inter-experiment time of 1600 μs to ensure collection of the signal of macropores. The inversion algorithm of FID curve provided by Magritek Ltd is based on the inversed Laplace transform with non-negative least squared (NNLS) inversion algorithm. Regularization parameters (also called smoothing parameters) were derived from L-curve the regularization parameter selection method. The logarithmic mean of T_2 (T_{2ML}), equivalent porosity, and T_2 distribution are provided.

Results and Discussion

μCT image and BET surface area

Figure 4.1 shows CT images of two grainstones, one packstone and one mudstone. The intensity of each pixel in grayscale (0-255, darkest to lightest) represent the hardness of material where harder materials cause less attenuation of X-ray. On these data, darker regions indicate softer

material and pore, lighter regions indicate harder material. Grainstone 1 (Figure 4.1 a) is an oolitic grainstone containing abundant oomoldic pores and is well cemented by calcite. Some moldic pores contain calcite spar. Grainstone 2 (Figure 4.1 b) is an oolitic grainstone in which ooids are mostly neomorphosed with very limited dissolution. The packstone (Figure 4.1 c) is a dolo-packstone that has medium grained dolomite crystals, and consists of higher portion of interparticle pores than grainstones. Mudstone (Figure 4.1 d) is a dolo-mudstone that is argillaceous and has no or very low interparticle porosity. Evident from the μCT images, the heterogeneity and complexity of our samples became more apparent in low porosity samples where complex intra- or interparticle pores dominate the porosity [*Evan K Franseen et al.*, 2003].

Low-pressure nitrogen adsorption measurements were applied to the same four samples as the μCT scans, representing different lithofacies (two grainstones, one packstone, one mudstone). The data revealed S_{por} of 12.69 μm^{-1} for packstone, 8.55 μm^{-1} for grainstone 1, 73.47 μm^{-1} for grainstone 2 (mean of grainstones is 41.01 μm^{-1}) and 114.10 μm^{-1} for mudstone.

Characteristics of NMR porosity and T_2 distribution

In general, the NMR porosity and conventional helium porosity correlate well (RMSE=0.24, Figure 4.2). In detail, with few exceptions, NMR porosity is up to 6.3 % p.u. lower than Helium porosity. Porosity for different lithologies varies drastically. Grainstone porosity extends from 2.8 % to 33.5 % with a median value of 16.9 % and standard deviation of 7.4% (n = 45); packstone porosity ranges from 2.6 to 7.2 % with a median value of 5.1 % and standard deviation of 1.5% (n = 5); and mudstone porosity varies from 1.4 to 10.4 % with a median value of 3 % and standard deviation of 3.9% (n = 5).

Several factors may explain the discrepancy between NMR porosity and helium porosity. First, NMR porosity is a function of saturation and calculated by the equivalent water volume over total sample volume. Loss of water then leads to underestimated porosity. Typically, the pore space

saturated by fluids is less than that which gas can intrude, especially in situations with poorly connected pore throats, because surface tension and low contact angle limit the saturation of fluid [*Brooks and Corey*, 1964]. Apart from the poorly connected pores, samples with vuggy open pores where grains are dissolved to be moldic space are unable to hold water in place during the experiment, resulting in lost signal strength and low porosity. Similarly, abundant micropores with relaxation time under the detection limit can cause porosity underestimation in NMR experiments [*Kenyon*, 1992; *Kleinberg et al.*, 1994]. With the dead time of our experiments, relaxation below 0.02 ms did not count into the total signal.

The T_2 relaxation times from representative grainstones, packstones, and mudstones (Figure 4.3) include unimodal and bimodal distributions for each class. Grainstone samples have a higher amplitude peak (up to 0.85), whereas packstone and mudstone samples have a lower amplitude peak (up to 0.26 and 0.19, respectively). These data reveal higher porosity in grainstones than in packstones and mudstones. Similar to the distinctive amplitude, the mode of T_2 distributions varies between grainstones, packstones, and mudstones. Grainstones have a larger peak T_2 value (above 500 ms), whereas the peak T_2 value of packstones is lower (around 200 ms), and the peak value of mudstones is lowest (generally less than 100 ms). Together, these data reveal smaller pores and less total porosity in packstone and mudstone samples than in grainstone samples.

T_{2ML} commonly is considered a length scale that represents characteristic pore size [*Slater et al.*, 2014; *Andreas Weller et al.*, 2010a]. T_{2ML} is calculated by the logarithmic mean theorem: $T_{2ML} = \mathrm{e}^{\frac{\sum \ln T_2}{N}}$, where N is the total sample size. Grainstones in general have high T_{2ML} (range from 10.94 ms to 844.29 ms). In contrast, packstones (range from 99.23 ms to 171.96 ms) and

mudstones (range from 24.60 ms to 225.98 ms) have lower T_{2ML}. A positive linear correlation (R^2 = 0.77) between porosity and T_{2ML} is evident (Figure 4.4).

According to the International Union of Pure and Applied Chemistry (IUPAC)'s definition for porous media [*Thommes et al.*, 2015], three pore types can be divided based on size: micropores (diameter d < 2 nm), mesopores (2 nm < d < 50 nm), and macropores (d > 50 nm). For most geo-materials, all three types of pores are formed simultaneously and may have been modified by syngenetic and diagenetic events. In many cases, bimodal or trimodal populations suggest two or three kinds of pore types and unimodal means the sample has relatively uniform pore size. For example, *Gan et al.* [1972] suggested T_2 distributions of gas shale samples were bimodal due to the organic mesopores and inorganic micropores that dominate such dense reservoirs [*Chalmers et al.*, 2012; *Mehana and El-monier*, 2016; *Tinni et al.*, 2017]. Likewise, *Yao and Liu* [2012]; *Yao et al.* [2010] confirm trimodal T_2 distribution in coal samples represent microfractures, primary macropores, and secondary mesopores.

It would be easy to use the T_2 distribution to differentiate pore types and conclude that unimodal samples have one pore type. However, a considerable amount of our samples show broad unimodal T_2 distribution that includes up to four orders of magnitude of relaxation time. *D Chang et al.* [1994] and *Marschall et al.* [1995] also tested the observed unimodal T_2 distribution in carbonate samples using MICP and thin section observations. The results, however, showed that those unimodal samples do have multiple pore sizes or pore throat sizes. This phenomenon, which causes T_2 modes to merge, is called pore coupling [*Ramakrishnan et al.*, 2001]. Due to the diffusion of protons from macropores (intraparticle and interparticle) to micropores, peaks of T_2 can shift and merge in some samples, to values that are not representative of the true pore size distribution. In previous research, pore coupling has been interpreted as a result of better

connectivity through pore systems [*Fordham et al.*, 1999] and has also been shown to relate to a higher surface relaxivity ρ_2. The unimodal T_2 distribution resulting from pore coupling in carbonate samples could be considered an implication of grain support [*John Doveton and Watney*, 2014], whereas bimodal distributions suggest mud support. However, to calibrate and verify the actual pore size distribution and pore types from NMR data, complementary analyses like digital image analysis, gas adsorption, and MICP are necessary.

Characteristics of complex conductivity spectra

Under the condition of pore-fluid conductivity σ_w = 0.12 S/m, and room temperature T_r = 24 °C, the impedance and phase shift of the saturated samples are measured from 0.1 Hz to 10 kHz. Frequency-dependent phase shifts of three representative grainstone, packstone and mudstone samples (Figure 4.5) show only data points in the frequency range of 0.1 Hz to 1000 Hz, to avoid the high-frequency coupling effect [*Niu et al.*, 2016]. The phase shift of mudstone (6-7 -mrad) and packstone (0.6-1.2 -mrad) are more pronounced than the phase shift of grainstone (0.8-4.6 -mrad) and show a flat plateau from 0.1 Hz to 1000 Hz, distinct from the general positive trend of the grainstone spectrum. The impedance spectrums of samples can be decomposed into real part of conductivity σ' and imaginary part of conductivity σ'' spectra (Figure 4.5). Doing so illustrates several interesting trends. First, the real part of conductivities σ' show a similar range and narrow variability among all samples, between 0.001 and 0.006 S/m (Figure 4.5a). For σ'' spectrums (Figure 4.5b), vary considerably, the peak values for a given frequency can be up to one order of magnitude different, with grainstones and packstones lower than mudstones. Second, the σ'' spectrums demonstrate similar shape as phase shift spectrum. All samples have σ'' values that increase as frequency increases, and have no peak frequency.

The low phase shift values are consistent with previous investigations of carbonate samples [*Müller-Huber et al.*, 2018; *Müller-Huber et al.*, 2016]. The phase shift of grainstone includes

exactly 1-5 –mrad, a value consistent with *Müller-Huber et al.* [2018] for oomodic Schaumkalk samples, although the packstone and mudstone have lower phase shift then they documented (5-12 -mrad). Peak frequency in phase shift spectrum and σ'' spectrum usually is interpreted as a characteristic that related to the dominant pore size and pore space features [*Luo and Zhang*, 1998; *A. Revil et al.*, 2014a; *A. Revil et al.*, 2012]. However, absence of peak frequency is observed commonly in carbonate samples [*Müller-Huber et al.*, 2018; *Niu et al.*, 2016] and is interpreted to correlate with broad pore-size distribution [*A Revil*, 2013]. For instance, the flat spectrum is interpreted to result not only from large 'broadness' of the pore-size distribution, but also high 'evenness' of the pore-size distribution where the 'broadness' and 'evenness' refer to the range of pore-size distribution and the fraction of each pore size in the spectrum. This argument is consistent with the T_2 distributions (Figure 4.3). The grainstone has roughly the same T_2 range (3-4 orders of magnitude) as T_2 distributions of mudstone and packstone. Therefore 'broadness' seems not sufficient to be a controlling parameter for the shape of phase shift spectrums and σ'' spectrums. The difference of 'evenness' of pore size distribution, in contrast, is more significanFt among lithofaices. Mudstone and packstone have more evenly distributed amplitude than grainstone. Evenly distributed amplitude implies an even contribution to the complex conductivity from induced polarization in different pore sizes which are consistent with the phase shift spectrums and σ'' spectrums. In such scenarios, instead of picking a peak frequency, Revil et al. (2010) suggest using the data points at 1 Hz to represent the characteristic pore size and pore space features.

The fact that σ' is not lithology dependent, but σ'' is lithology dependent, indicates that they are sensitive to different petrophysical features or processes. Based on the physical meaning of real part of conductivity σ', it may be the pore cross-sectional area and the effective path length,

or the effective flow path, that controls σ' [*Vinegar and Waxman*, 1984]. In contrast, the imaginary part of conductivity σ'' has an additional dependency on the parameters that describe the complexity of the pore system, like pore-size distribution [*Vinegar and Waxman*, 1984], chargeability [*A. Revil et al.*, 2014a; *Scott and Barker*, 2003] and surface area [*A. Weller et al.*, 2010b]. Therefore, it is reasonable that mudstones with higher surface area and inter-surface chargeability can have a higher σ'' than packstones and graistones, as discussed in detail in the following section.

Petrophysical properties derived from NMR and SIP

a. Pore-size distribution and characteristic pore size

As shown in Equation 3, $\frac{1}{T_2}$ is equal to $\frac{1}{T_{2S}}$ under the assumption that relaxation phenomena represent a fast diffusion regime. Both pore-size distribution and surface area-to-volume ratio S_{por} are derived from T_2 distribution.

The BET-derived S_{por} are used to calculate ρ_2 in this data set, revealing average ρ_2 values of 2.8 μm/s for grainstone, 0.6 μm/s for packstone and 0.1 μm/s for mudstone (for individual ρ_2 for each sample, see Table 4.3). These data match ρ_2 values reported by previous studies on carbonate rocks, which range from 0.1 to 3.5 μm/s [*Bhagat et al.*, 2012; *Marschall et al.*, 1995]. Assuming nearly spherical pore shapes (geometry factor a=3), the pore-size distribution of same six samples used in Figure 4.2 can be calculated by Equation 3 (Figure 4.4). Since the Equation 3 expresses a linear transformation, the shape of pore-size distribution is the same as the shape of T_2 distribution. Since the T_2 for free water is about 2s, the corresponding pore size is 16.8 μm if we assume ρ_2=2.8 μm/s. The pore-size distribution generated from NMR relaxation time covers a wide range of pore size from 0.1 nm to 100 μm. Water in pores beyond 100 μm then is considered 'bulk water' and will have the same relaxation time as free water. Though signals from bulk water

are collected, they can't be differentiated from the signals from water in 100 μm pores. This upper limit of NMR porosimetry may induce underestimation of characteristic pore size and average pore size of samples with pores > 100 μm, e.g. oomoldic grainstones.

Most commonly, comparing pore-size distribution with other petrophysical properties uses a representative value of the distribution. Corresponding to the characteristic value for T_2 distribution - T_{2ML}, the characteristic pore size Λ can be calculated using Equation 3 as well (Table 4.3). Grainstones in general have larger characteristic pore sizes (up to 4 μm) than packstones (50 to 100 nm) and mudstones (less than 20 nm, except 33-25 which is 126.84 nm). To be noticed that, some grainstones have significant amount of vuggy pores and ooids that are larger than 100 μm according to the hand sample observation and μCT images. Apart from the underestimation of T_{2ML} due to the limitation of NMR porosimetry, there are two more reasons that may cause characteristic pore sizes of grainstones to be underestimated. One is that ρ_2 of grainstones is averaged down by grainstone samples that have less ooilitic pores. Another reason is that vuggy and oolitic pores don't hold water very well in position, most of connected vuggy and oolitic pores can be under-saturated during measurement.

In porous media with one dominant pore size which is been defined as the size of pores that dominant the fluid flow behavior, T_{2ML} is proportional to the dominant pore size and therefore, characteristic pore size Λ can be used to represent the dominant pore size [*Banavar and Johnson*, 1987].

However, T_{2ML} most likely does not represent the dominant pore size in bimodal or trimodal samples since T_{2ML} gives the information of most abundant pore sizes while it's usually the pore-throat size dominant the fluid flow behavior. Many researchers have realized the limitation of using a single Λ value to represent the complex pore size distribution of samples and therefore,

related the Λ value with an imperial length - $1/S_{por}$ [*Katz and Thompson*, 1986; *A. Revil et al.*, 2014b; *Robinson et al.*, 2018]. *Osterman et al.* [2016] and *Robinson et al.* [2018] compared permeability predicted using Λ, $1/S_{por}$ and T_{2ML} and showed that it provided very similar results; from this observation, they suggested $1/S_{por}$ and T_{2ML} both contain necessary pore space information for permeability prediction.

b. S_{por}

The lithofacies-specific ρ_2 values were used to estimate S_{por} from the T_2 distributions. The NMR-derived S_{por} plotted with porosities (Figure 4.8) demonstrates a power-law correlation (R^2=0.82). One observation from this plot is the wide range of S_{por} from 0.2 μm^{-1} to over 200 μm^{-1} in some low porosity (4 - 8 %) samples.

This elevated S_{por} range is attributed to the roughness of pore surface and grain surface, as revealed by μCT images. Samples with higher S_{por} have rougher surfaces, less particle contact, and smaller grain size than samples with lower S_{por}. This interpretation is consistent with previous work by *Bang et al.* [2012] in pure calcium carbonate precipitation and *Walter and Morse* [1984] in dissolution test of skeletal carbonate, which supports the conclusion that grains with rougher surfaces and smaller sizes have greater specific surface area. Although both are grainstone samples, sample LKC89 (S_{por} = 169.92/μm) has moldic pores filled by micrite which are small crystals that contribute a lot to the surface area, whereas sample LKC135 (S_{por} = 39.54/μm) has moldic pores that are well preserved and smooth where the inner surface of cortices are covered by recrystallized dolomite spars. This observation suggests that parameters like T_{2ML} and S_{por} are sensitive to surface roughness.

The imaginary conductivity σ'' has been related to pore attributes [*A. Revil and Florsch*, 2010; *A. Weller et al.*, 2010b]. The S_{por} can be estimated from σ'' (Equation 10), with the assumption that the change of bulk property formation factor F is insignificant. Studies like *A. Revil and Florsch* [2010]; *A. Weller et al.* [2010b] documented either well-defined linear correlation or power-law correlation between S_{por} and σ'' in consolidated sandstone and unconsolidated sand-clay mixed samples. Instead of a clear linear relationship, the carbonate samples from all three lithofacies in this study only define a general positive trend between σ'' and S_{por} (Figure 4.8) with a weak power-law correlation between σ'' and S_{por} (R^2 = 0.17; with an exponent of 0.21), markedly less significant than the correlation in sandstone and sand samples [*Kruschwitz et al.*, 2010; *A. Weller et al.*, 2010b]. It is possible that S_{por} itself is not the parameter that controls the imaginary part of conductivity in carbonates. Additional parameters need to be considered and counted to correlate σ'' and S_{por} in carbonate rocks.

Niu et al. [2016] concluded that the single linear relationship between σ'' and S_{por} claimed by *A. Revil and Florsch* [2010] and *A. Weller et al.* [2010b] is not appropriate for low-porosity clayey samples. *Niu et al.* [2016] also emphasized on the importance of formation factor F in relating σ'' with S_{por}, and argued that F should not be ignored (Equation 10) if it varies considerably. Equation 10 indicates that, theoretically, the S_{por}/F is the textural parameter that controls σ'' in porous media. To validate the relationship between σ'' and S_{por} and F as proposed by *Niu et al.* [2016] in carbonates, F values were estimated by measuring all fifty-one samples saturated with four fluids with different salinities. The results reveal that as porosity increases, F tends to decrease from over 700 down to 11 (see Table 4.3. for more details). Almost all packstones and mudstones have F greater than 50, with corresponding low porosity, high S_{por}, and low ρ_2. In contrast, grainstones have F values lower than 50. The power-law correlation between $\sigma'' \cdot F$ and

S_{por} (R^2 = 0.62 for the power-law relationship; Figure 4.10) is evident and is stronger than it between σ" and S_{por}. Likewise, the power-law relation for $\sigma" \cdot F - S_{por}$ correlation includes an exponent of 0.44, which is not quite similar to the exponents of the power-law relationship on $\sigma" - S_{por}$ established for other samples (0.96 for sand + clay in Slater et al. 2006; 0.996 for sandstones and unconsolidated samples in Weller et al. 2010b). This result suggests that S_{por}/F has more important control than S_{por}on the imaginary conductivity in carbonate rocks. This observation is consistent with the empirical equation 10, and could directly help geophysicists calculate S_{por} and determine other hydraulic properties like hydraulic conductivity and tortuosity of porous media from SIP measurements.

c. Porosity exponent *m* from Archie's law

Generally, F has an approximate exponential correlation with porosity, as expected from Archie's Law where $F = \varphi^{-m}$. The range of calculated porosity exponent *m* is 1.19 to 3.63, with an average of 2.10. This range of *m* is comparable with the data demonstrated by *Borai* [1987] and *Focke and Munn* [1987]. Figure 4.11 shows that F is generally following the Archie's Law with porosity exponent *m* ranged from 1 to 3 while Figure 4.12 shows that the *m* is positively correlated with porosity.

This observation is opposite to the negative correlations between *m* and porosity in sandstones [*Borai*, 1987], shales [*Cho et al.*, 2016], and even some oolitic and sucrosic limestones [*Casteleyn et al.*, 2011; *Focke and Munn*, 1987], where *m* generally becomes larger as cementation occurs. However, similar positive correlations have been described by *Borai* [1987], *Focke and Munn* [1987], *J H Doveton* [2014], and *Rankey et al.* [2018] in moldic limestones, moldic dolostones and oomoldic dolostones.

The variety of $m-\varphi$ correlations has inspired studies that focus on interpreting the physical meaning of *m*. *Focke and Munn* [1987] proposed that the m is controlled by pore types where samples with dominantly intergranular or intercrytalline pores act like siliciclastics and m decreases or remains constant as porosity increases. On the other hand, in rocks with dominantly moldic pores, m increases with increasing porosity. A more detailed investigation on the effect of moldic pores on *m* is performed by *Ragland* [2002], who finds that a higher percentage of isolated moldic pores relates to lower connectivity and consequently higher m. *Ragland* [2002] also finds that adding 10-15% percent of open fractures to moldic samples can decrease *m* from 3.2 to 2.1. To quantify the influence of pore-size distribution on m, *Niu and Zhang* [2018b] numerically studied the change of electric field density and m in samples with a variety of grain size, grain shape, and pore size in granular material. They concluded that *m* is related to pore-scale variations in the electrical field, and increasing *m* is linked to the increasing volume fraction of pore throats (pore throat volume/total pore volume) regardless of the grain shape, grain size distribution, and porosity. Therefore, the *m* increases with increasing porosity is possibly because higher porosity samples typically have higher volume fraction of pore throats.

The grainstone samples consist of well-developed oomolds and well-preserved micritized cortices. Some of the moldic pores are partially or fully filled by cements. The CT images of a high porosity (33.5 %), high *m* (3.27) grainstone 1 (Figure 4.1 a) and low porosity, low *m* grainstone 2 (Figure 4.1 b) show that grainstone 1 is dominated by oomoldic pores which are either isolated or connected by micro-factures caused by a collapsed cortex. In contrast, grainstone 2 includes more intraparticle pores and no long-narrow pores. As stated by *Herrick and Kennedy* [1994], it is the narrowest part of The moldic pores contribute to total porosity but do not contribute to the electrical current transportation unless localized micro-fractures, cortex crushing, or

dissolution connect the dissolved ooids with other ooids or with interparticle pores. Yet interconnecting moldic pores are connected by long-narrow pores (Figure 4.1 a)) and less conductive interparticle pores. In other words, those long-narrow pores or micro-fractures are considered pore throats regarding electrical properties. Therefore, the samples with poorly connected oomolds and an increasing percentage of pore throat are related to higher m. The more regular shape and point contact of the crystals (as shown in CT-images of mudstone and packstone) produce better connected intercrystalline pores, a low percentage of pore throats, and more effective electric conduction, resulting in higher formation factor F and thus lower cementation factor m.

d. Permeability

In searching for the appropriate permeability models for the carbonate samples, relationships between permeability and complex conductivity parameters (σ', σ") were plotted (Figures 4.13 and 4.14). Figure 4.13 reveals two trends. First, an exponential relationship (linear in log-space) between real conductivity σ' and k_{air} is evident for grainstone samples ($R^2 = 0.67$), however, no such correlation exists in packstone and mudstone. Second, mudstones and packstones have relatively invariant σ' comparing with grainstones that have similar , especially in samples with low k. Compared with the $\sigma' - k$ plot (Figure 4.13), the $\sigma" - k$ data (Figure 4.14) are more scattered (R^2 = 0.09 versus 0.67). Grainstone samples appear to define a general exponential trend between σ" and k, whereas packstones and mudstones are not having any evident trend.

Several studies have built empirical or semi-empirical relationships that link σ" to k, especially for sandstones and unconsolidated samples [*A. Revil et al.*, 2015; *A. Revil and Florsch*, 2010; *Andreas Weller et al.*, 2010a], mostly following the approach of linking σ" to S_{por}, and then

calculating k from S_{por} using the Kozeny-Carman equation (Equation 11). Although linear [*A. Weller et al.*, 2010b] or power-law [*Slater*, 2007] relationships between σ" and k are evident in sandstone, unconsolidated sands, and sand clay mixtures, no such relationship is observed for these carbonate samples. As mentioned above, since σ" is sensitive to the total pore surface that conducts charges, and k is more sensitive to effective transport paths for hydraulic flow, the disconnection between these two parameters may be more common in carbonate samples that went through complex digenesis. A comparison of carbonate and sandstone samples [*Ehrenberg and Nadeau*, 2005] revealed distinctive statistical trends between arithmetically averaged permeability and average porosity for sandstones and carbonate, and such results were interpreted to reflect diverse paragenetic and diagenetic histories.

The real part of conductivity σ' has been used to calculate formation factor *F,* and then permeability k based on the K-C model (Equations 13-15, *Katz and Thompson* [1986]). The observed versus expected data (Figure 4.15) illustrate a statistically significant correlation (R^2 = 0.67, P<0.001).

The relationship among porosity, permeability, and T_{2ML} (Figure 4.16) suggests samples with higher T_{2ML} generally have higher porosity and higher permeability. On the contrary, samples with lower T_{2ML} have lower porosity but a wide range of permeability. Mudstone and packstone samples are completely overlapping with each other and all have relatively low T_{2ML} values (<150ms) except one with 253.7ms, whereas the grainstone samples covers a wide range of T_{2ML}. Therefore, despite the reality of limited sample set, especially with few mudstone and packstone samples, T_{2ML} does not show well correlation with permeability in our data set. Thus, careful calibration and lab work is needed alongside further work that derives k from σ" on carbonate.

Permeability estimation from SIP and NMR is possible through empirical relationships, however, it also needs careful calibration and better petrophysical models.

Regarding the results above, the mixed pore types and broad pore size distribution in carbonate have impacts on both NMR and SIP responses. Results of this study suggest that NMR and SIP responses can be complementary to each other while interpreting the petrophysical properties of carbonate samples. NMR results can distinguish a variety of pore size distributions and SIP results could differentiate pore types. Clearly, the existing permeability models need to be improved to understand the different pore attribute controls on permeability better. Moreover, the permeability estimation from multiple geophysical measurements might be feasible and provide a reliable estimation of the pore size distribution [*Niu and Zhang*, 2018a; *Osterman et al.*, 2016].

The complexity of the pore system in carbonate

The purpose of comparing petrophysical parameters with each other is finding potential correlations that can be used to infer one parameter from others. Moreover, it is expected that by comparing NMR and SIP responses which are based on different physical principles, understanding of relations between geometric properties (i.e., pore size, pore shape, texture) and petrophysical properties can be improved. Based on their sensitivity to the pore space, the petrophysical parameters discussed in this study can be grouped into parameters sensitive to total pore space (T_{2ML}, σ", m, F, and S_{por}) and parameters sensitve to effective pore space (σ', and permeability), where effective pore space refers to the effective hydraulic or electrical pathway. The relatively prononced correlation between porosity - T_{2ML} (Figure 4.4, with R^2=0.77, P<0.001), porosity - S_{por} (Figure 4.8, with R^2=0.82, P<0.01), S_{por} - $\sigma"F$ (Figure 4.10, with R^2=0.62, P<0.01), porosity - m (Figure 4.12, with R^2=0.65, P<0.001), permeability - σ' (Figure 4.13, with R^2=0.67, P<0.001) and the relatively ambiguous correlation between permeability - σ" (Figure

4.13, with with R^2=0.09, P<0.05), porosity - permeability - T_{2ML} (Figure 4.16) therefore have shown better relevance among paramters that are sensitive to total pore space than with parameters that only sensitive to effeccticve pore space. The weak correlation between parameters sensitive to total pore sapce and parameters sensitive to effeictive pore space indicates that in some carbonate rock we tested, abundant pore space (i.e., semi-isolated and dead-end pores) only contribute to the total pore surface area and total porosity, but not to effective hydraulic and electrical pathways.

One of the most evident observations in this study is that geophysical responses do not always exhibit distinct behavior among different lithologies. One explanation for this lack of correspondence could be that the study simply lacked enough packstone and mudstone samples to be statistically valid. That is, a total of five packstones and five mudstones are not sufficient to draw any definitive conclusions. Moreover, all packstone and mudstone samples are low porosity (<10%), which may not be representative of the range of variability.

Beyond these limitations, however, petrophysical properties derived from NMR and SIP are more likely to sensitive to the pore geometry and fluid behavior in carbonate rocks rather than to depositional texture. That is saying depostional textures are not always distinguishable by NMR and SIP since different depositional textures could have very similar characterisitics and consequently similar NMR and SIP reponses. *Janson and Lucia* [2018] analyzed on carbonate with different depositional textures and claim that the combination of pore types and pore space heterogeneity due to diagenesis could lead to very similar geophysical responses (e.g., acoustic velocity and NMR responses) for different lithologies which validated those observations presented in this study where mudstones, packstones, grainstones can have very similar relations among petrophysical properties.

Another noteworthy observation is that none of these petrophysical parameters correlations conducted in this study yields as high coefficient of determination R^2 as those correlations of sandstones or granular materials (R^2 = 0.840 for S_{por} - σ" relation of sandstones in *A. Weller et al.* [2010b], or R^2 = 0.93 for S_{por} - $\sigma"F$ relation of porous borosilicate samples in *Niu et al.* [2016]). Similarly, the porosity - acoustic P-velocity and S_{por} - acoustic P-velocity relations are not as pronounced as in sandstones [*Casteleyn et al.*, 2011; *Janson and Lucia*, 2018] even though acoustic P-velocity is a geophysical response with more dependency on mechanical properties of the carbonate matrix than the NMR and SIP responses examined here. The weaker correlations between petrophysical parameters in carbonate, in comparison with the correlations developed in sandstones, could possible related to the characteristic of carbonate pore system. Unlike sandstones, which typically are composited by just relatively homogeneous interparticle pores , all carbonates contain multiple pore types, which consequently induce pronounced petrophysical heterogeneity even within subfacies [*Choquette and Pray*, 1970; *Mazzullo*, 2004]. The creation of such complicated pore system is related to the development of both primary and secondary porosity [*Choquette and Pray*, 1970; *Lucia*, 1983]. All carbonate sediments have elevated primary porosities (up to 70%), and include interparticle, intraparticle, framework pores and seltered pores before they have entirely solidified. Porosity can drop dramatically from 70% to 1% [*Lucia*, 2007] during diagenesis, due to factors such as compaction, cementation, recrystallization and other diagenetic processes [*C H Moore*, 2001]. Later on, other diagenesis processes (e.g., dissolution and dolomitization) can modify the pore attributes of rock and create secondary porosity, including intercrystalline, moldic, vuggy, and even cavernous pores. Of pore types, interparticle and intercrystalline pores are well connected and contribute more to the effective hydraulic and electrical paths, whereas moldic and solution-enlarged pores (vuggy, cavernous) can produce

semi-connected or isolated pores that have limited contribution to the effective hydraulic and electrical paths, but contribute to responses of total pore space-sensitive parameters. For instance, oomoldic grainstones in this study (Figure 4.1a) can have oomoldic pores that are connected by microfractures, which result in rocks with high porosity and intermediate to high S_{por}. Those dead-end oomoldic pores increase porosity and S_{por}, but will not help transport the fluid or transmit electrical current. On the contrary, crushing oomoldic pores can decrease the porosity, but improve the permeability, as illustrated by *Hussain* [2006]. This mechanism may be why samples with similar porosity or S_{por} but have wide range of permeability (Figure 4.16). In a more micro scope, the diagenesis that makes the pore interfaces rougher which increases the S_{por} but have little impact on the effective porosity and permeability.

Overall, as stated by *Lucia* [2007], the complexity of petrophysical responses of carbonates is controlled primarily by two geometric information of pore system: pore types and pore size distribution. *Müller-Huber et al.* [2018] claim that derivation of geometric information of carbonates requires validating petrophysical data with other methods to overcome the scale limitations and blind spots. For instance, the two geophysical methods applied in this study, NMR and SIP, are sensitive to pore attributes (e.g., porosity, pore size, S_{por}), but on different physical bases. By assessing the correlations among petrophysical parameters generated by two methods, this study helps building a integral methods of evaluating complex carbonate pore attributes and corresponding reservoir properties using NMR and SIP.

Chapter 5. Logging data analysis

The primary task of reservoir evaluation is to provide a full picture of the nature, behavior and distribution of reservoir rocks and fluids. To fulfill the objective, multidisciplinary log analysis [*Dewan*, 1983] has served as the petrophysical basis for geological and geophysical data interpretation. Initiated by the oil and gas industry, conventional well-logging tools and interpretation methods are well developed, yet modern logs like NMR logs are not fully exploited in many workflows. To fill this gap, the aim of this part of the study is to harness the full potential of NMR logging data in carbonate reservoir characterization. Specifically, this study focuses on assessing the potential of T_1/T_2 ratio being a lithology indicator by using it as an input variable to recognize subclasses of electrofacies within a carbonate succession.

Lithofacies from core description

Franseen (1994, 2000) and Steinhauff et al. (1998) identified facies characteristic of Arbuckle strata in Kansas. Their results reveal that although Arbuckle rocks have been extensively dolomitized, much of the dolomitization is non-fabric destructive, thereby original depositional facies and textures are preserved. Of ten principal facies, the target interval (from 4900 to 5000 ft, 1633-1667 m) contains only five lithofacies: mudstone, packstone, grainstone, incipient breccia and breccia. Grainstone consist of intraclasts, ooids and peloids, skeletal fragments, and was interpreted to represent high-energy deposition in a subtidal to peritidal environment. Abundant cement nearly totally occludes porosity, and leads to low permeability. Packstone and mudstone typically are massive to horizontally laminated. Porosities range from 3% to around 20%. Breccias commonly are associated with subaerial exposure. The evaporation of sea water lead to evaporite depostion, and the dissolution of evaporite, in turn, induced

collapse horizons in Arbuckle strata. Due to the heterogeneous texture, porosities and permeabilities of breccias in this interval vary considerably.

Data from NMR log

As introduced in the methodology, the application of NMR logs in the petroleum industry facilitates reservoir evaluation by providing hydrogen content and relaxation time directly from the measurements [*Kenyon*, 1997]. Empirical relationships allow these information to be used to calculate apparent porosity, pore size distribution and permeability [*Kleinberg et al.*, 1994]. The NMR logs we have access to provides both longitudinal relaxation and transverse relaxation measurements, describes as T_1 and T_2 distributions, respectively. Figure 5.1 shows lithofacies and corresponding T_2 and T_1 distributions within the depth interval of 4900 - 5000 ft. Overall, the transverse relaxation rate $1/T_2$ is larger than the longitudinal relaxation rate $1/T_1$. It is noteworthy that most of the porosities in T_1 distributions are in the bin T_1 = 2048 ms which is due to the detecting cap of the equipment is set to 2048 ms.

T_1/T_2 ratio – a petrophysical property indicator

From the NMR theory, both T_1 and T_2 spectra are represented by multi-exponential curves and should have very similar shapes. The T_1/T_2 ratio is a scaler of longitudinal relaxation time distribution versus transverse relaxation time distribution. The intensity function $a_{1,2}$ of both longitudinal and transverse relaxation time [*Khetrapal et al.*, 1975; *Kleinberg et al.*, 1994] can be derived from following equations:

$$M_1(t) = \sum_{i=0} a_1(T_{1i}) \left(1 - 2e^{-\frac{t}{T_{1i}}}\right), \tag{28}$$

$$M_2(t) = \sum_{i=0} a_2(T_{2i})\, e^{-\frac{t}{T_{2i}}}. \tag{29}$$

To calculate T_1/T_2 ratio, both a_1 and a_2 are required [*Kleinberg et al.*, 1993a]. For instance, a_1 and a_2 are intensity functions for discrete relaxation times T_i (i = 4, 8 … 2048 ms). The zero-normalized cross-correlation coefficient, P, can be calculated from the equation:

$$\mathrm{P}_{a_1 a_2}(\omega) = \sum_{i=0} \frac{1}{\sigma_{a_1}\sigma_{a_2}} [a_1(T_{1i}) - a_1(\overline{T_1})] * [a_2(\omega T_{2i}) - a_2(\omega \overline{T_2})], \qquad (30)$$

where ω is the multiplier which is T_1/T_2 ratio, σ_{a_1} and σ_{a_2} are the standard deviation of amplitudes of T_1 and T_2 spectrums, $\overline{T_1}$ and $\overline{T_2}$ are the mean value of T_1 and T_2. This simplified correlation function is constrained by the shape and range of T_1 and T_2 distributions. Although ω can be obtained by maximizing $\mathrm{P}_{a_1 a_2}(\omega)$, the effective range of i should be carefully selected with fully considering the saturation states, saturation fluids, and fractures [*Kleinberg et al.*, 1993b; *Song et al.*, 2002].

The T_1/T_2 values calculated from the focus interval range from 0.89 to 7.62. As introduced in Chapter 3, a ternary plot of quartz, calcite and dolomite abundance can be used to represent the mineral constituents of a carbonate reservoir. To test for potential correlation between T_1/T_2 and mineralogy, a plot of $U_{maa} - \rho_{maa}$ includes superimposed with T_1/T_2 in color within the target interval (from 4900 to 5000 ft, or 1633-1667 m) (Figure 5.2). This $U_{maa} - \rho_{maa}$ cross plot indicates that mineral components of the target interval are mostly quartz and dolomite with limited calcite. High ρ_{maa} and high U_{maa} indicate more dolomite content, while lower ρ_{maa} and U_{maa} reflect increasing silica (quartz) content. In the cross plot (Figure 5.2), relatively high T_1/T_2values (>5) and relatively low T_1/T_2 values (<2) appear to correspond with highly dolomitic samples, whereas intermediate T_1/T_2 (2-5) samples are broadly distributed. The correlation between dolomite percentage and T_1/T_2 value suggests that T_1/T_2

may be an indicator of lithology for the subclasses of carbonate like Arbuckle Group with high purity of dolomite.

The T_1/T_2 value has been interpreted as an indicator of the molecular environment of hydrogen proton [*Callaghan*, 1991]. In bulk and unrestricted space, without the participation of multiphase fluid or the impact from diffusion, the T_1/T_2 value is equal to one [*Kleinberg et al.*, 1993b]. *Callaghan* [1991] concluded that, within a confined environment, such as a pore, decreasing T_2 corresponds to the restricted motion of water molecules, whereas increasing T_1 indicates more ordered lattice structure and higher crystallinity. These results suggest that T_1/T_2 value would be higher in more ordered materials, and in materials with smaller pores. Therefore, changing of T_1/T_2 calculated from the NMR log is expected to be related to variations in mineralogy and texture, e.g., lithofacies.

To assess the potential of T_1/T_2 as a lithology indicator, other well-defined lithology indicators, such as total gamma ray (GRTO) and conductivity (CT90), are used for comparison. Both comparisons between gamma ray and T_1/T_2 (Figure 5.3a) and conductivity and T_1/T_2 (Figure 5.3b) show no obvious relationship. Based on these comparisons, T_1/T_2 ratio may be as useful as other conventional lithology indicators (gamma ray and conductivity) in lithofacies recognition, yet T_1/T_2 defines distinct petrophysical properties. Therefore, next section explores a more qualitative means to identify the utility of T_1/T_2, by using T_1/T_2 as a input to recognize electrofacies.

Electrofacies Classification

PCA

Eight logs, including T_1/T_2 ratio (*NMRR*), apparent matrix density (ρ_{maa}), matrix volumetric photoelectric absorption (U_{maa}), total porosity (*PHIT*), lateral log 90 inch

conductivity (*CT90*), total Gamma-ray reading (*GRTO*), Thorium (*THOR*), and Potassium (*POTA*) were extracted from the NMR, spectral gamma-ray, photoelectric, density and neutron, porosity curves as input variable suite for electrofacies recognition. Data used in PCA are from the whole Arbuckle Group in Well Wellington #1-32 (4162-5160 ft, or 1387-1720 m) and average values of each log for five lithofacies are listed in Table 5.1. The Pareto distribution of 8 eigenvalues for each eigenvector (Figure 5.4) illustrates that the first 2 principal components account for 59% of the total variability. Figure 5.5 shows the biplot of PC1 and PC2 where loading vectors show contribution of original variables (well logs) to PC1 and PC2 and the correlations among original variables. In detail, if two vectors are close and form a small angle, the two input well logs are well correlated [*J H Doveton*, 2014; *Martinez and Kak*, 2001]. The length of vectors represents the variance of each principle component gained from original well-logs. By reading the biplot (Figure 5.5), Thorium (*THOR*), Potassium (*POTA*) and Total Gamma-ray (*GRTO*) have similar weight on each principle component. ρ_{maa} and U_{maa} vectors point to high negative PC2 and low positive PC1 values, which are negatively correlated with total porosity (*PHIT*) and conductivity (*CT90*) that are almost 180 degrees away from ρ_{maa} and U_{maa} vectors. T_1/T_2 (*NMRR*) is isolated from the other vectors, with relatively small PC1 (4.21) and PC2 (-1.67).

The *PHIT* and *CT90* vectors have very similar scores showing a strong correlation between porosity and conductivity. Conventionally, conductivity is considered positively correlated with porosity [*Bernabe et al.*, 2011; *Johnson et al.*, 1986]. However, breccias have lower porosity but higher conductivity compared with non-breccia carbonate in these Arbuckle data (Table 5.1). Those breccia samples were formed due to the collapse of paleokarst features, and they are locally cemented with micrite [*E. K. Franseen*, 2000; *Evan K Franseen et al.*,

2003]. Brecciation and fracturing make vuggy porosity, whereas the autoclasts (typically from mudstones and wackestones) are better cemented than the matrix of breccia samples. Therefore, even the total porosity is low, the well connected vuggy pores and intercrystalline pores make breccia samples more conductive. *THOR, POTA* and *GRTO* are extracted from the spectral gamma-ray, and are indicators of clay content. Therefore, their scores are similar to each other (Figure 5.5). Another pair of lithology indicators are ρ_{maa} and U_{maa} (Table 5.2). The difference between breccia samples and other samples becomes distinctive, as breccia samples are low in both ρ_{maa} and U_{maa} values which is consistent with the observation (*Evan K Franseen et al.* [2004] that most Arbuckle breccias are autobrecciated and have very limited terrigenous constituents. NMRR does not carry as much variance as other vectors in PC1 and PC2 which means there are more information distributed in other principle components.

Cluster Analysis

In defining clusters, an important bit of *a priori* information is the number of expected clusters. In this study, since the clustering algorithm – FCM is an unsupervised method, an accurate number of clusters is required during the self-training process [*Bezdek et al.*, 1984; *Zadeh*, 1996]. For instance, the number of clusters is fixed as five, corresponding to five primary lithofacies including mudstone, packstone, grainstone, incipient breccia, and breccia. Initially, five cluster centers are inserted randomly on the Euclidean space of the PC1-PC2 cross plot and self-training starts with an initial guess of cluster membership values μ_{ij}. Objective function of all five clusters then are calculated and updated until the stopping criteria is reached. This analysis uses PCA and cluster analysis results of all eight input variables (well logs) as an example. The objective function meets the minimum threshold at iteration 11. Updated centers (crosses in color) are superimposed with clusters of principal component scores (Figure 5.6).

Five clusters are defined as five distinctive electrofacies from EF1 to EF5 for further interpretation. The PC1 reasonably maps EFs. EF1 and EF2 plot in negative PC1 regime whereas EF3-5 has positive PC1 values. EF1 tends to be more distinctive with lower PC1 values and can be easily differentiated from other EFs. Meanwhile, EF3, EF4, and EF5 heavily overlap with one another, indicating similarity among EF3-5.

Classification

To achieve the unsupervised classification of clusters generated in the last step, this procedure is simply decomposed as the following workflow. First, five clusters are assigned with five lithofacies with no repetition, and then S in Equation 26 is calculated. Next, the first step is repeated with different permutations of lithofacies k times, here k is 120 for 5 clusters. Finally, the analysis picks the combination that minimizes S as the 'electrofacies'. The classifications show that clusters with positive PC1 scores tend to have more carbonate (mudstone, packstone, grainstone) and clusters with negative PC1 scores, suggesting breccia carbonate (incipient breccia and breccia) that contain more clay content and are a less pure carbonate. Within carbonate clusters, grainstone have higher matrix volumetric photoelectric absorption than packstone and mudstone, indicating higher dolomite content and lower abundance of clay minerals in grainstones. Three carbonate clusters are overlap, and have very close cluster centroids, suggesting the importance of a fuzzy clustering algorithm instead of hard-boundary algorithms.

The outcome of overlapping clusters can be explained from a geological perspective. Specifically, petrophysical responses of different textures of carbonate (mudstone, packstone, grainstone) can be very similar, and similar petrophysical responses would have similar principle components scores. In contrast, incipient breccia and breccia can be distinguished very well

because of more distinctive PC1 and PC2 scores as a result of the dissimilarity of petrophysical responses. Specifically, compared with incipient breccia, breccia has lower dolomite content, higher porosity (because of dissolution), and higher clay content.

Predicted Electrofacies

To quantitatively validate if the T_1/T_2 can improve the accuracy of prediction of lithofacies, a series of electrofacies discrimination employed different variable sets. Most well-log based carbonate reservoir characterizations utlilize density, neutron, conductivity and gamma-ray logs as inputs, especially when no modern logs are available [*Asgari and Sobhi*, 2006; *Dorfman et al.*, 1990; *Lee et al.*, 2002; *Perez et al.*, 2005]. As a control group, this study also uses total porosity, total gamma ray and lateral log 90 inches conductivity as the primary input variable set (Set 1 for short) for electrofacies classification.

To test whether NMRR improves classification, NMRR was added to the primary input dataset asto form the second input variable set (Set 2). Furthermore, a full log suite except NMRR was tested as a third input variable set (Set 3). Finally, the full log suite including NMRR serves as forth input variable set (Set 4). Each variable set was used as input for a PCA, a clustering analysis and a classification, thus generating four predictions of electrofacies. A graphic predicted electrofacies log of each of these variable sets provides a means to visually compare predictions with a full core description and special core analysis (Figure 5.7). For reference, a total gamma ray curve of this interval (Figure 5.7 a) is also provided for comparison. The core-plug profile (Figure 5.7 b) shows the lithofacies identified from both static rock typing (core-plug observation) and dynamic rock typing (special core analysis).

Calculating the objective function *S* provides a means to compare the recognition accuracy of each variable set. Results of Set 1, 2, 3, and 4 have *S* = 1.81, 1.68, 1.55, and 1.54,

respectively, and a lower value means better accuracy on recognizing lithofacies. The outcome of Set 1 serves as a baseline of the recognition, and it has the lowest accuracy (Figure 5.7 c), especially in differentiating breccias from other lithofacies. Adding NMRR to Set 1 decreases the value of the objective function of Set 2 (Figure 5.7 d), from 1.81 to 1.68. Moreover, Set 2 lowers the misprediction rate of lithofacies from 0.79 to 0.66, and also decreases the number of incorrect predictions between non-breccia dolomites and incipient breccia and breccia. Therefore, the introduction of NMRR increased the recognition accuracy relative to the control group (Set 1). The results from Set 3 and Set 4, which includes more mineralogy related parameters (*THOR, POTA,* ρ_{maa}*,* U_{maa}), outperform sets 1 and 2 with minimized objective function values. For example, both Set 3 and Set 4 successfully discern a breccia layer (4910 ft) that is missed in Set 1 and 2. However, comparing the *S* values of Set 4 and Set 3, the inclusion of NMRR in Set 4 does not improve the assessment of Set 3 markedly. This result indicates that NMRR provides information partly redundant with other mineralogy related well logs.

Discussion

The T_1/T_2 values calculated from Wellington well 1-32 in this study are consistent with the measured values from *Cheng et al.* [2017]; *Kenyon et al.* [1988] study shows a wide range of T_1/T_2 from 1 to 6 in carbonate samples. The assumption of apparent T_1/T_2 ratio is the reflection of lithology is based on the general correlation between NMRR and other lithology indicators such as porosity, conductivity, gamma-ray, and the ρ_{maa} versus U_{maa} plot. However, the parameters affecting T_1/T_2 need to be discussed further.

Impact of lithology on T_1/T_2

Numerous studies conducted on T_1/T_2 indicate a correlation between T_1/T_2 and lithology [*D Chang et al.*, 1994; *Kenyon*, 1992; *A Timur*, 1969]. There are two major mechanisms that can

be used to explain this correlation. One mechanism is diffusion-induced shorting of T_2 in samples that have well-connected small pores. As suggested by Equation 2, a total of three relaxation mechanisms (bulk, surface and diffusive relaxation) are involved in the transverse relaxation. whereas only bulk relaxation and surface relaxation are involved in longitudinal relaxation. In other words, T_1 is not shortened by diffusion, although T_2 is. If the fast diffusion regime is assumed, both bulk and diffusive relaxation can be neglected, therefore the T_1/T_2 is simply the ratio of surface relaxivities, ρ_1/ρ_2 , which should be a constant in one sample. However, the diffusion term is not always ignorable, especially when the connectivity between pores is good [*Anand and Hirasaki*, 2007; *Hürlimann et al.*, 2003] or the localized magnetic field heterogeneity is significant [*Kleinberg et al.*, 1994; *Strange et al.*, 1993]. *Song et al.* [2002] demonstrates that in a water saturated oolitic limestone, T_1/T_2 = 1.5 for long relaxation times and T_1/T_2 = 4 for short relaxation times. Due to the existence of two distinct environments, the authors concluded that higher T_1/T_2 value is the result of more important diffusion among small pores. Therefore, high T_1/T_2 values can be used to recognize samples with high amount of small pores.

The second underlying mechanism of linking T_1/T_2 to lithology is the change in surface relaxivity. Such change in relaxivity can be induced by changes in mineral surface environment, including variations in physicochemical properties like surface potential, ion concentration, and contact angle with pore fluid, affinity of pore surface and pore fluid [*Daigle et al.*, 2014; *Foley et al.*, 1996; *Kleinberg et al.*, 1993a]. *Aytekin Timur* [1972] and *D Chang et al.* [1994] measured and compared transverse surface relaxivity ρ_2 of carbonate and sandstone samples, and observed that dolomite and calcite have lower ρ_2 than sandstones and pure quartz. *Kleinberg et al.* [1994] suggested an average ρ_1/ρ_2 =1.6 for 6 sandstone samples, but also claim that the increasing of

anisotropic electron motion can decrease ρ_1/ρ_2. One reason that causes low anisotropic electron motion is an increase in abundance of clay minerals which carry paramagnetic particles (Fe, Cu, Cr, and etc.) that eliminate the anisotropy of electron motion, and therefore slows longitudinal relaxation down. Therefore, the higher clay content and metal content will increase the T_1/T_2 ratio due to the higher content of the paramagnetic particle.

Previous laboratory observations established the connection between T_1/T_2 and lithology, or at least pore-size distribution and mineralogy. However, by comparing the accuracy of four different variable sets, no significant improvement in electrofacies recognition is observed by adding NMRR data into the variable set (Set 4 versus Set 3). This result suggests thar NMRR is not a valid rock type indicator, at least in these Arbuckle data.

Impact of fluid on T_1/T_2

One consideration is that the changes in T_1 and T_2 depend on not just lithology but also the reservoir fluid types. Since the NMR signal is directly sensitive to the hydrogen content (water and hydrocarbon) and the corresponding environment, T_1 and T_2 are actually capturing the fluid properties and fluid-rock interactions instead of the solid properties. Viscosity, one of the most important fluid properties, turns to play a vital role in controlling the hydrogen motion and change of T_1/T_2. The T_1/T_2 ratio initially was considered a constant in brine-saturated rock samples under low-frequency magnetic field (2 MHz) [*Freedman and Morriss*, 1996; *Kleinberg et al.*, 1993b], whereas later studies conducted on oil shale and gas shale [*Coates et al.*, 1999; *Straley*, 1997] elucidate T_1/T_2 fluid typing in the presence of mixed fluids in the same sample. Comparing with T_1/T_2 value of water (1-2), solid-like and highly viscous hydrocarbons generally have higher T_1/T_2 value (up to 100), whereas light oils and gas with low viscosity have lower T_1/T_2 (4-20) [*Coates et al.*, 1999; *Freedman et al.*, 2001]. The results in *Washburn and Birdwell* [2013] and

Fleury and Romero-Sarmiento [2016] show that bitumen, heavy oil and methane have high T_1/T_2 and increase the overall T_1/T_2.

The test well, Wellington KGS 1-32, is not a producing well, and the Arbuckle Group in this area is extensively water-flooded with bare residual oil. However, gas may still be a confounding factor driving T_1/T_2 values. The dependency of fluid in deriving T_1/T_2 is also prominent in the PCA results. According to the loadings of each component referenced to input variables (Table 5.2), NMRR vector has relatively low loadings on both PC1 and PC2 compared with other logs and the maximum correlation between NMRR and principal component appears in principal component 4 with a very high loading 0.936. This indicates that the change in NMRR values heavily depends on the parameter(s) that are not strongly associated with other input variables. For instance, NMRR is the only input variable that both sensitive to the fluid types and lithologies which makes the similar results of Set 3 and 4 reasonable due to the low weight of fluid type in rock typing.

However, the fact that T_1/T_2 is sensitive to fluid type does not exclude it from being a potential indicator for rock typing since the behavior of fluids is also closely related to other petrophysical properties that are rock type indicators, like pore shape and pore size. Gas has a higher residual saturation with broader pore size distribution in the water-wet system [*Zhou and Blunt*, 1997] and holds a more stable water film in large pores [*Blunt*, 2001]. Higher complexity of pore shape is also corresponding to the higher capillary pressure [*Or and Tuller*, 1999; *W Xu et al.*, 2014], which prevents water from displacing gas in the pore [*Valvatne et al.*, 2005].

Therefore, the appropriate use of NMRR in rock typing is interpreted to require calibration with fluids effects. With a more insightful understanding of multi-phase flow in carbonate under a low magnetic field, we expect to derive a modified T_1/T_2 value that is exclusively representative

of the lithology. Recently, the application of 2-D T_1 - T_2 map gives a more effective way to recognize multi phases simultaneously and it has become a popular means for fluid typing [*Fleury and Romero-Sarmiento*, 2016; *Mailhiot et al.*, 2017]. By using 2-D T_1 - T_2 maps, signals from hydrocarbons can be recognized and eliminated to minimize the impact on the T_1/T_2 value from non-water phases. Nonethless, although it needs further investigation, the impact of multi-phase flow on NMR data is beyond the scope of this study.

Other controls that may fail electrofacies recognition

Lithofacies (geological facies) sometimes cannot be tied to electrofacies (petrophysical facies) due to 1) statistical analysis applied is not sensitive to the subtle changes of logs between facies [*Brandsegg et al.*, 2010; *J H Doveton*, 2014], and 2) different resolution and scale of well and laboratory measurements [*Hurlimann et al.*, 2005].

In this case study, the targeting zone is restricted in one 100 feet interval where the change of lithology is limited, which also leads to an insignificant change of log data for electrofacies recognition. The gamma-ray log shows a very typical response for clean sedimentary rocks. Except for 4955-4961 ft, where gamma-ray values reach 45 API units, the the section has the uniformly low readings (Figure 5.7 a), indicating clean carbonate with low clay content. Similarly, the trace of deep resistivity (RDEP) changes only slightly, within one order of magnitude. The consistent formation resistivity cannot provide detail information for rock-typing, and it suggests relatively homogenous pore attributes and mineral composition at the scale of the resolution of the log. This interpretation is consistent with the concentrated readings in $U_{maa} - \rho_{maa}$ MID plot (Figure 5.2). Therefore, although 8 different log data are applied to the electrofacies recognition, they may not provide enough variation that the statistical methods needed to differentiate sub-facies (mudstone, packstone, grainstone) inside of the carbonates. *El*

Sharawy and Nabawy [2016] document similar results, statistical methods that failed to discern the difference between dolomitic limestone and limestone, although they did successfully recognize sandstone, shale, and limestone. The difficulty of recognizing carbonate sub-electrofacies in this study indicates those sub-electrofacies are too similar and not discernable by the proposed statistical method. As *Brandsegg et al.* [2010] and *J H Doveton* [2014] suggest, since PCA is a linear dimentionality reduction method, the distance between and within lithofacies are considered with the same scale. As a result, variability of sub-facies in a fairly uniform lithofacies will be masked by the varibility between major lithofacies. To solve that problem, either a structured PCA which analyzes sub-facies independently [*Brandsegg et al.*, 2010] or a non-linear dimensionality reduction method (e.g., T-distributed Stochastic Neighbor Embedding (t-SNE) method [*Van Der Maaten*, 2009]) should be considered to express the variablity within and without one lithofacies in different scale.

Another possible reason that affects the accuracy of electrofacies recognition is the different resolution among logs and the different scale between log data and core observations. Take NMR as an example, NMR log is one of the most time-consuming logging tools, but also essentially penetrates a large area of detection [*Coates et al.*, 1999]. This aspect induces so-called 'bed boundary effect,' in which the NMR log may collect several geological bed volumes, each with distinct properties, in a single NMR measurement [*Kleinberg et al.*, 1993b]. The bed boundary effect leads to merging of geophysical responses from thin layers and discrepancy on the resolution between NMR and other logs. This discrepancy of resolution even can be observed within between T_1 and T_2 measurement since T_1 measurement requires an even longer time than T_2 measurement. This basically means T_1/T_2 ratio is also affected by such bed boundary effect. Meanwhile, comparing with lithologies determined from core plug samples with a diameter of

3.8 cm, log data are more of a moving average of a much larger inverstigation area. Considering both vertical and lateral facies variance of the research area (introduced in Chapter 2), the mismatching between log data and core observations should not be surprising.

Although the application of conventional multivariate statistical methods (e.g., PCA, cluster analysis, and discriminant analysis using well logs) have succeeded in predicting electrofacies and corresponding permeability in many carbonate reservoirs [*Burke et al.*, 1969; *H-C Chang et al.*, 1997; *J H Doveton*, 2014; *Qi and Carr*, 2006], this study is consistent with the results of *Dorfman et al.* [1990], *Lee et al.* [2002] and *Criollo et al.* [2016]. Those studies documented that, without core calibration, the accuracy of recognizing sub-facies of carbonate is low, compared to the accuracy of distinguishing between sandstone and shale. Meanwhile, the adding of T_1/T_2 ratio does not improve the accuracy of rock typing much, due to the reasons and impacts that been discussed before. To improve the accuracy of recognizing electrofacies, alternate statistical methods like structured PCA, should be considered, and need to be constrained by more *a priori* information like depth. Furthermore, the infucluence from fluid should be eliminated by using $T_1 - T_2$ map and also permeability should be calculated to compare with core-permeability which provides a more practical evaluation of the reservoir quality.

Chapter 6. Conclusion

Core Analysis

To explore possible correlations between geophysical responses and pore attributes in carbonate rocks, a workflow combines NMR and SIP measurements on core samples was applied to the investigation. Results reveal that (1) NMR and SIP responses of grainstone are distinct from

responses of mud-rich carbonate (packstone and mudstone whereas packstone and mudstone are quite similar, perhaps due to the small sample size); (2) Oppositely, the relations among petrophysical properties calculated from NMR and SIP display no distinct trend for different lithologies. This result indicates those petrophysical properties are more sensitive to pore attributes (e.g., pore size distribution, pore shape, etc.) than to depositional textures. (3) NMR and SIP tools are complimentary to one another for deriving petrophysical properties like pore size distribution, pore types, surface area, and permeability. This result suggests that a combined method (using both NMR and SIP) has advantages to individual tools in identifying different carbonate textures and pore attributes; (4) The well-defined relations between $\sigma'' \cdot F - S_{por}$ implies it may be useful to estimate electrical properties and S_{por}, independent of lithology. The presence of a power-law relation (akin to that present in siliciclastic rocks) suggests that some of the models well developed and applied to sandstones can be modified and applied to carbonates as well; (5) K-C equations are applied successfully to grainstones to estimate permeability, whereas the extreme sensitivity of σ'' to total pore surface area obscures relations between permeability and σ'' in packstone and mudstone samples (muddy carbonates). Thus, a next step of estimating carbonate permeability should be developing a model that sensitive to pore types. (6) Based on their correlations with each other, the petrophysical parameters discussed in this study can be grouped into parameters sensitive to total pore space (porosity, T_{2ML}, σ'', m, F, and S_{por}) and parameters sensitive to effective pore space (σ', and permeability) where effective pore space refers to the effective hydraulic or electrical pathway.

Well Log Analysis

To examine the potential application of the NMR log in reservoir characterization, this study explores the suitability of combining T_1/T_2 (NMRR, derived from NMR log) with other

logs to recognize sub-electrofacies within a dolostone reservoir interval in the Arbuckle Group, of southern Kansas. Logs of a total interval of 100 ft of the Arbuckle dolostone in the Wellington KGS 1-32 well were classified in this study into five lithofacies (mudstone, packstone, grainstone, incipient breccia, and breccia). Correlations between T_1/T_2 values and other lithology related indicators like ρ_{maa}, U_{maa}, total gamma-ray (GRTO) and lateral log 90 inches conductivity (CT90) are tested. To validate the inference of NMRR as a lithology indicator, PCA, Fuzzy C-mean clustering, and an unsupervised classification with four distinct sets of input logs recognized five electrofacies corresponding to five lithofacies. The PCA and clustering results show that among five electrofacies, incipient breccia and breccia are more distinct while mudstone, packstone and grainstone heavily overlap. The comparison of classification results between Set 1 (PHIT, GRTO, and CT90), and Set 2 (Set 1 with NMRR) indicates that adding of NMRR reduced the recognition error from 1.81 to 1.68 (unitless) whereas the errors of Set 3 (Set 1 with THOR, POTA, ρ_{maa}, U_{maa}) and Set 4 (Set 3 with NMRR) are close (1.55 and 1.54). These outcomes suggest that adding T_1/T_2 can improve the classification accuracy if THOR, POTA, ρ_{maa}, U_{maa} data are not available; the ratio failed to improve the classification accuracy if all logs are available. There are three specific conclusions can be drawn from these results: 1) T_1/T_2 contains lithology information redundant to other logs; 2) T_1/T_2 is not solely controlled by lithology, but also controlled by fluid types and fluid behaviors; 3) T_1/T_2 is not sensitive enough to differentiate small changes among sub-classes in relatively pure dolostone. To make T_1/T_2 more representative to lithology, a 2-D $T_1 - T_2$ based analysis is needed to filter out signals from hydrocarbon in the future.

This study exploits the potential of borehole NMR data which focuses on investigating the inferences from NMR longitudinal and transverse relaxation time ratio (T_1/T_2) on

electrofacies characterization. The analysis suggests that NMR logging data have considerable potential in characterizing petrophysical properties of reservoirs, beyond what traditionally has been analyzed and interpreted. Nonetheless, challenges remain in the interpretation of data, such as how to connect the physical meanings of relaxivity change to mineralogy change, and how to eliminate the impact of hydrocarbon to get a more representative NMRR for lithology.

To conclude, this thesis proposes the possible electrical and NMR models for complex carbonate samples. It demonstrates the benefits of integrating NMR and SIP in characterizing petrophysical and geometrical properties of carbonate samples by assessing petrophysical relationships among NMR and SIP responses. Meanwhile, this thesis work illustrates of the utilization of the NMR imaging log in determining electrofacies. Also, by analyzes the factors controlling the variation within NMR logging data, this study will help to better interpret NMR logging data and improve the carbonate reservoir characterization. This thesis demonstrates the potential of combining electrical and NMR methods to advance understandings of fluid distribution and fluid flow in carbonate.

References

Abell, A. B., K. L. Willis, and D. A. Lange (1999), Mercury Intrusion Porosimetry and Image Analysis of Cement-Based Materials, *Journal of Colloid and Interface Science*, *211*(1), 39-44.

Akbar, M., et al. (1995), Classic Interpretation Problems - Evaluating Carbonates, *Oilfield Review*, *7*(1), 38-57.

Ali, L., S. Bordoloi, and S. Wardinsky (2008), Modeling Permeability in Tight Gas Sands Using Intelligent and Innovative Data Mining Techniques, in *SPE Annual Technical Conference and Exhibition*, edited, Society of Petroleum Engineers, Denver, Colorado, USA.

Anand, V., and G. J. Hirasaki (2007), Diffusional Coupling Between Micro And Macroporosity For NMR Relaxation In Sandstones And Grainstones1, *Petrophysics*, *48*(04).

Anselmetti, F. S., and G. P. Eberli (1999), The velocity-deviation log: A tool to predict pore type and permeability trends in carbonate drill holes from sonic and porosity or density logs, *AAPG bulletin*, *83*(3), 450-466.

Archie, G. E. (1942), The electrical resistivity log as an aid in determining some reservoir characteristics, *Transactions of the American Institute of Mining and Metallurgical Engineers*, *146*(01), 54-61.

Asgari, A. A., and G. A. Sobhi (2006), A fully integrated approach for the development of rock type characterization, in a middle east giant carbonate reservoir, *Journal of Geophysics and Engineering*, *3*(3), 260-270.

Banavar, J. R., and D. L. Johnson (1987), Characteristic pore sizes and transport in porous media, *Physical review B*, *35*(13), 7283-7286.

Bang, J. H., Y. N. Jang, W. Kim, K. S. Song, C. W. Jeon, S. C. Chae, S. W. Lee, S. J. Park, and M. G. Lee (2012), Specific surface area and particle size of calcium carbonate precipitated by carbon dioxide microbubbles, *Chemical Engineering Journal*, *198*, 254-260.

Barrande, M., R. Bouchet, and R. Denoyel (2007), Tortuosity of porous particles, *Analytical Chemistry*, *79*(23), 9115-9121.

Barwick, J. S. (1928), The Salina Basin of North-Central Kansas, *AAPG bulletin*, *12*(2), 177-199.

Behroozmand, A. A., K. Keating, and E. Auken (2015), A Review of the Principles and Applications of the NMR Technique for Near-Surface Characterization, *Surveys in Geophysics*, *36*(1), 27-85.

Bernabe, Y., M. Zamora, M. Li, A. Maineult, and Y. B. Tang (2011), Pore connectivity, permeability, and electrical formation factor: A new model and comparison to experimental data, *Journal of Geophysical Research-Solid Earth*, *116*(B11), 204.

Bezdek, J. C. (2013), *Pattern recognition with fuzzy objective function algorithms*, 13-44, Springer Science & Business Media.

Bezdek, J. C., R. Ehrlich, and W. Full (1984), FCM: The fuzzy c-means clustering algorithm, *Computers & Geosciences*, *10*(2-3), 191-203.

Bhagat, A., C. H. Sondergeld, and C. S. Rai (2012), The Petrophysical Study on UAE Carbonates, paper presented at 2012 SEG Annual Meeting, Society of Exploration Geophysicists.

Binley, A., L. D. Slater, M. Fukes, and G. Cassiani (2005), Relationship between spectral induced polarization and hydraulic properties of saturated and unsaturated sandstone, *Water Resources Research*, *41*(12), 417.

Blunt, M. J. (2001), Flow in porous media—pore-network models and multiphase flow, *Current opinion in colloid & interface science*, *6*(3), 197-207.

Borai, A. (1987), A new correlation for the cementation factor in low-porosity carbonates, *SPE formation evaluation*, *2*(04), 495-499.

Börner, F., M. Gruhne, and J. Schön (1993), Contamination indications derived from electrical properties in the low frequency RANGE1, *Geophysical Prospecting*, *41*(1), 83-98.

Brandsegg, K. B., E. Hammer, and R. Sinding-Larsen (2010), A comparison of unstructured and structured Principal Component Analyses and their interpretation, *Natural resources research*, *19*(1), 45-62.

Brooks, R. H., and A. T. Corey (1964), Hydraulic properties of porous media and their relation to drainage design, *Transactions of the ASAE*, *7*(1), 26-0028.

Bucheb, J. A., and H. B. Evans (1994), Some applications of methods used in electrofacies identification, *The Log Analyst*, *35*(01).

Bultreys, T., M. A. Boone, M. N. Boone, T. De Schryver, B. Masschaele, L. Van Hoorebeke, and V. Cnudde (2016), Fast laboratory-based micro-computed tomography for pore-scale research: Illustrative experiments and perspectives on the future, *Advances in water resources*, *95*, 341-351.

Burdine, N. (1953), Relative permeability calculations from pore size distribution data, *Journal of Petroleum Technology*, *5*(03), 71-78.

Burke, J. A., R. L. Campbell, Jr., and A. W. Schmidt (1969), The Litho-Porosity Cross Plot A Method Of Determining Rock Characteristics For Computation Of Log Data, in *SPE Illinois Basin Regional Meeting*, edited, Society of Petroleum Engineers, Evansville, Indiana.

Busch, J., W. Fortney, and L. Berry (1987), Determination of lithology from well logs by statistical analysis, *SPE formation evaluation*, *2*(04), 412-418.

Callaghan, P. T. (1991), *Principles of nuclear magnetic resonance microscopy*, Clarendon Press.

Carman, P. C. (1937), Fluid flow through granular beds, *Transactions-Institution of Chemical Engineeres*, *15*, 150-166.

Carr, H. Y., and E. M. Purcell (1954), Effects of diffusion on free precession in nuclear magnetic resonance experiments, *Physical Review*, *94*(3), 630.

Casteleyn, L., P. Robion, C. David, P.-Y. Collin, B. Menéndez, N. Fernandes, G. Desaubliaux, and C. Rigollet (2011), An integrated study of the petrophysical properties of carbonate rocks from the “Oolithe Blanche” formation in the Paris Basin, *Tectonophysics*, *503*(1-2), 18-33.

Cerepi, A. (2004), Geological control of electrical behaviour and prediction key of transport properties in sedimentary porous systems, *Colloids and Surfaces A: Physicochemical and Engineering Aspects*, *241*(1), 281-298.

Chalmers, G. R., R. M. Bustin, and I. M. Power (2012), Characterization of gas shale pore systems by porosimetry, pycnometry, surface area, and field emission scanning electron microscopy/transmission electron microscopy image analyses: Examples from the Barnett, Woodford, Haynesville, Marcellus, and Doig units, *AAPG bulletin*, *96*(6), 1099-1119.

Chang, D., H. J. Vinegar, C. Morriss, and C. Straley (1994), Effective Porosity, Producible Fluid And Permeability In Carbonates From Nmr Logging, in *SPWLA 35th Annual Logging Symposium*, edited, p. 21, Society of Petrophysicists and Well-Log Analysts, Tulsa, Oklahoma.

Chang, H.-C., H.-C. Chen, and J.-H. Fang (1997), Lithology determination from well logs with fuzzy associative memory neural network, *IEEE transactions on geoscience and remote sensing*, *35*(3), 773-780.

Cheng, Y., S. Chen, M. Eid, G. Hursan, and S. Ma (2017), Determination of Permeability From NMR T1/T2 Ratio in Carbonates, edited, Society of Petrophysicists and Well-Log Analysts.

Cho, Y., E. Eker, I. Uzun, X. Yin, and H. Kazemi (2016), Rock Characterization in Unconventional Reservoirs: A Comparative Study of Bakken, Eagle Ford, and Niobrara Formations, in *SPE Low Perm Symposium*, edited, p. 15, Society of Petroleum Engineers, Denver, Colorado, USA.

Choquette, P. W., and L. C. Pray (1970), Geologic nomenclature and classification of porosity in sedimentary carbonates, *AAPG bulletin*, *54*(2), 207-250.

Clarkson, C. R., N. Solano, R. M. Bustin, A. Bustin, G. Chalmers, L. He, Y. B. Melnichenko, A. Radliński, and T. P. Blach (2013), Pore structure characterization of North American shale gas reservoirs using USANS/SANS, gas adsorption, and mercury intrusion, *Fuel*, *103*, 606-616.

Clavier, C., and D. H. Rust (1976), Mid Plot:a New Lithology Technique, *The Log Analyst*, *17*(06), 1-9.

Coates, G. R., L. Xiao, and M. G. Prammer (1999), *NMR logging: principles and applications*, 6-89 pp., Haliburton Energy Services Houston.

Cole, V. B. (1975), Subsurface Ordovician-Cambrian Rocks in Kansas, *Reprinted 1981ed.) Lawrence, Kansas: Kansas Geological Survey*, *2*.

Criollo, D., Z. Marin, and D. Vasquez (2016), Advanced Electrofacies Modelling and Permeability Prediction: A Case Study Incorporating Multi-Resolution Core, NMR and Image Log Textural Information Into a Carbonate Facies Study, paper presented at 22nd Formation Evaluation Symposium of Japan, Society of Petrophysicists and Well-Log Analysts.

Curtis, M. E., R. J. Ambrose, and C. H. Sondergeld (2010), Structural characterization of gas shales on the micro-and nano-scales, paper presented at Canadian unconventional resources and international petroleum conference, Society of Petroleum Engineers.

Daigle, H., A. Johnson, J. P. Gips, and M. Sharma (2014), Porosity Evaluation of Shales Using NMR Secular Relaxation, in *Unconventional Resources Technology Conference, Denver, Colorado, 25-27 August 2014*, edited, pp. 1205-1216.

Delfiner, P., O. Peyret, and O. Serra (1987), Automatic determination of lithology from well logs, *SPE formation evaluation*, *2*(03), 303-310.

Dewan, J. T. (1983), *Essentials of modern open-hole log interpretation*, 97-114, PennWell Books.

Diamond, S. (2000), Mercury porosimetry: an inappropriate method for the measurement of pore size distributions in cement-based materials, *Cement and concrete research*, *30*(10), 1517-1525.

Dorfman, M., J.-J. Newey, and G. Coates (1990), New techniques in lithofacies determination and permeability prediction in carbonates using well logs, *Geological Society, London, Special Publications*, *48*(1), 113-120.

Doveton, J., and H. Cable (1979), Fast matrix methods for the lithological interpretation of geophysical logs, in *Geomathematical and petrophysical studies in sedimentology*, edited, pp. 101-116, Elsevier.

Doveton, J., and L. Watney (2014), Textural and pore size analysis of carbonates from integrated core and nuclear magnetic resonance logging: An Arbuckle study, *Interpretation*, *3*(1), SA77-SA89.

Doveton, J. H. (2014), *Principles of mathematical petrophysics*, 122-170, Oxford University Press (UK).

Dullien, F. A. L. (1975), New network permeability model of porous media, *AIChE Journal*, *21*(2), 299-307.

Dunn, J. C. (1973), A Fuzzy Relative of the ISODATA Process and Its Use in Detecting Compact Well-Separated Clusters, *Journal of Cybernetics*, *3*(3), 32-57.

Dunn, K.-J., D. J. Bergman, and G. A. LaTorraca (2002), *Nuclear magnetic resonance: Petrophysical and logging applications*, 114-119, Elsevier.

Ehrenberg, S., and P. Nadeau (2005), Sandstone vs. carbonate petroleum reservoirs: A global perspective on porosity-depth and porosity-permeability relationships, *AAPG bulletin*, *89*(4), 435-445.

El Sharawy, M. S., and B. S. Nabawy (2016), Determination of electrofacies using wireline logs based on multivariate statistical analysis for the Kareem Formation, Gulf of Suez, Egypt, *Environmental Earth Sciences*, *75*(21), 1394.

Ellis, D. V., and J. M. Singer (2007), *Well logging for earth scientists*, 57-64, Springer.

Falzone, S., J. Robinson, and L. Slater (2018), Characterization and Monitoring of Porous Media with Electrical Imaging: A Review, *Transport in Porous Media*, 1-26.

Flaum, C., and G. Pirie (1981), Determination Of Lithology From Induced Gamma-Ray Spectroscopy, in *SPWLA 22nd Annual Logging Symposium*, edited, Society of Petrophysicists and Well-Log Analysts, Mexico City, Mexico.

Fleury, M., and M. Romero-Sarmiento (2016), Characterization of shales using T1–T2 NMR maps, *Journal of Petroleum Science and Engineering*, *137*, 55-62.

Focke, J., and D. Munn (1987), Cementation exponents in Middle Eastern carbonate reservoirs, *SPE formation evaluation*, *2*(02), 155-167.

Foley, I., S. Farooqui, and R. Kleinberg (1996), Effect of paramagnetic ions on NMR relaxation of fluids at solid surfaces, *Journal of Magnetic Resonance, Series A*, *123*(1), 95-104.

Ford, D. C., and P. W. Williams (2007), *Karst hydrogeology and geomorphology*, 6-12, Wiley Online Library.

Fordham, E., W. Kenyon, T. Ramakrishnan, L. Schwartz, and D. Wilkinson (1999), Forward models for nuclear magnetic resonance in carbonate rocks, *The Log Analyst*, *40*(04).

Franseen, E. K. (2000), A review of Arbuckle Group strata in Kansas from a sedimentologic perspective: Insights for future research from past and recent studies, *The Compass: Earth Science Journal of Sigma Gamma Epsilon*, *75*(2-3), 68-89.

Franseen, E. K. (2006), *Mississippian (Osagean) shallow-water, mid-latitude siliceous sponge spicule and heterozoan carbonate facies: An example from Kansas with implications for regional controls and distribution of potential reservoir facies*, 23 pp., Kansas Geological Survey.

Franseen, E. K., A. P. Byrnes, J. R. Cansler, and T. Carr (2004), The geology of Kansas: Arbuckle Group, *Current Research in Earth Sciences: Kansas Geological Survey, Bulletin*, *250*, 1-43.

Franseen, E. K., A. P. Byrnes, J. R. Cansler, D. M. Steinhauff, T. R. Carr, and M. K. Dubois (2003), Geological Controls on Variable Character of Arbuckle Reservoirs in Kansas: An Emerging Picture, *The University of Kansas, Lawrence*.

Freedman, R., S. Lo, M. Flaum, G. J. Hirasaki, A. Matteson, and A. Sezginer (2001), A New NMR Method of Fluid Characterization in Reservoir Rocks: Experimental Confirmation and Simulation Results, *Spe Journal*, *6*(04), 452-464.

Freedman, R., and C. E. Morriss (1996), Apparatus including multi-wait time pulsed NMR logging method for determining accurate T2-distributions and accurate T1/T2 ratios and generating a more accurate output record using the updated T2-distributions and T1/T2 ratios, edited, Google Patents.

Gan, H., S. P. Nandi, and P. L. Walker (1972), Nature of the porosity in American coals, *Fuel*, *51*(4), 272-277.

Gregg, S. J., K. S. W. Sing, and H. Salzberg (1967), Adsorption surface area and porosity, *Journal of The Electrochemical Society*, *114*(11), 279C-279C.

Grimm, E. C. (1987), CONISS: a FORTRAN 77 program for stratigraphically constrained cluster analysis by the method of incremental sum of squares, *Computers & Geosciences*, *13*(1), 13-35.

Gun'ko, V., V. Turov, R. Leboda, V. Zarko, J. Skubiszewska-Zieba, and B. Charmas (2007), Adsorption, NMR, and thermally stimulated depolarization current methods for comparative analysis of heterogeneous solid and soft materials, *Langmuir*, *23*(6), 3184-3192.

Guo, P. (2012), Dependency of Tortuosity and Permeability of Porous Media on Directional Distribution of Pore Voids, *Transport in Porous Media*, *95*(2), 285-303.

Heckel, P., and J. F. Baesemann (1975), *Environmental interpretation of conodont distribution in Upper Pennsylvanian (Missourian) megacyclothems in Eastern Kansas*, 486-509 pp.

Herrick, D. C., and W. D. Kennedy (1994), Electrical efficiency—A pore geometric theory for interpreting the electrical properties of reservoir rocks, *Geophysics*, *59*(6), 918-927.

Hinai, A. A., R. Rezaee, L. Esteban, and M. Labani (2014), Comparisons of pore size distribution: A case from the Western Australian gas shale formations, *Journal of Unconventional Oil and Gas Resources*, *8*, 1-13.

Holubnyak, Y., W. Watney, J. Rush, M. Fazelalavi, and D. Wreath (2017), Pilot Scale CO2 EOR in Mississippian Carbonate Reservoir at Wellington Field in South-central Kansas, *Energy Procedia*, *114*, 6989-6996.

Hurlimann, M. D., C. Flaum, M. Flaum, L. Venkataramanan, and R. L. Kleinberg (2005), Nuclear magnetic resonance method and logging apparatus for fluid analysis, edited, Google Patents.

Hürlimann, M. D., M. Flaum, L. Venkataramanan, C. Flaum, R. Freedman, and G. J. Hirasaki (2003), Diffusion-relaxation distribution functions of sedimentary rocks in different saturation states, *Magnetic resonance imaging*, *21*(3-4), 305-310.

Hussain, M. (2006), Recognizing attributes and oomoldic porosity development in eolianite in an arid setting: An example from the quaternary eolianite from the Arabian Gulf coastline, Saudi Arabia, *Carbonates and Evaporites*, *21*(2), 124.

Jain, A. K. (2010), Data clustering: 50 years beyond K-means, *Pattern recognition letters*, *31*(8), 651-666.

Janson, X., and F. J. Lucia (2018), Matrix microcrystalline structure and acoustic properties of oomoldic dolograinstone, *Geophysics*, *83*(4), Mr199-Mr210.

Jewett, J. M., and D. F. Merriam (1959), Geologic framework of Kansas; a review for geophysicists, paper presented at Symposium on geophysics in Kansas: Kansas Geological Survey Bulletin.

Johnson, D. L., J. Koplik, and R. Dashen (2006), Theory of dynamic permeability and tortuosity in fluid-saturated porous media, *Journal of Fluid Mechanics*, *176*(-1), 379-402.

Johnson, D. L., J. Koplik, and L. M. Schwartz (1986), New pore-size parameter characterizing transport in porous media, *Phys Rev Lett*, *57*(20), 2564-2567.

Jolliffe, I. (2011), *Principal component analysis*, Springer.

Katz, A. J., and A. H. Thompson (1986), Quantitative prediction of permeability in porous rock, *Phys Rev B Condens Matter*, *34*(11), 8179-8181.

Kenyon, W. E. (1992), Nuclear-Magnetic-Resonance as a Petrophysical Measurement, *Nuclear Geophysics*, *6*(2), 153-171.

Kenyon, W. E. (1997), Petrophysical principles of applications of NMR logging, *The Log Analyst*, *38*(02).

Kenyon, W. E., P. I. Day, C. Straley, and J. F. Willemsen (1988), A three-part study of NMR longitudinal relaxation properties of water-saturated sandstones, *SPE formation evaluation*, *3*(03), 622-636.

Kenyon, W. E., J. J. Howard, A. Sezginer, C. Straley, A. Matteson, K. Horkowitz, and R. Ehrlich (1989), Pore-size distribution and NMR in microporous cherty sandstones, paper presented at SPWLA 30th Annual Logging Symposium, Society of Petrophysicists and Well-Log Analysts.

Khetrapal, C. L., A. Kunwar, A. Tracey, and P. Diehl (1975), NMR basic principles and progress, *Springer*, *9*, 89-115.

Kim, H.-M., B. K. Mallick, and C. C. Holmes (2005), Analyzing Nonstationary Spatial Data Using Piecewise Gaussian Processes, *Journal of the American statistical Association*, *100*(470), 653-668.

Kleinberg, R. L., S. A. Farooqui, and M. A. Horsfield (1993a), T1/T2 ratio and frequency dependence of NMR relaxation in porous sedimentary rocks, *Journal of Colloid and Interface Science*, *158*(1), 195-198.

Kleinberg, R. L., W. E. Kenyon, and P. P. Mitra (1994), Mechanism of NMR Relaxation of Fluids in Rock, *Journal of Magnetic Resonance, Series A*, *108*(2), 206-214.

Kleinberg, R. L., C. Straley, W. E. Kenyon, R. Akkurt, and S. A. Farooqui (1993b), Nuclear magnetic resonance of rocks: T1 vs. T2, paper presented at SPE annual technical conference and exhibition, Society of Petroleum Engineers.

Kozeny, J. (1927), *Über kapillare Leitung des Wassers im Boden:(Aufstieg, Versickerung und Anwendung auf die Bewässerung)*, Hölder-Pichler-Tempsky.

Kruschwitz, S., A. Binley, D. Lesmes, and A. Elshenawy (2010), Textural controls on low-frequency electrical spectra of porous media, *Geophysics*, *75*(4), Wa113-Wa123.

Latour, L. L., P. P. Mitra, R. L. Kleinberg, and C. H. Sotak (1993), Time-Dependent Diffusion-Coefficient of Fluids in Porous-Media as a Probe of Surface-to-Volume Ratio, *Journal of Magnetic Resonance Series A*, *101*(3), 342-346.

Lee, S. H., A. Kharghoria, and A. Datta-Gupta (2002), Electrofacies characterization and permeability predictions in complex reservoirs, *SPE Reservoir Evaluation & Engineering*, *5*(03), 237-248.

Lim, J.-S., H.-J. Park, and J. Kim (2006), A new neural network approach to reservoir permeability estimation from well logs, paper presented at SPE Asia Pacific Oil & Gas Conference and Exhibition, Society of Petroleum Engineers.

Lin, Q., Y. Al-Khulaifi, M. J. Blunt, and B. Bijeljic (2016), Quantification of sub-resolution porosity in carbonate rocks by applying high-salinity contrast brine using X-ray microtomography differential imaging, *Advances in water resources*, *96*, 306-322.

Loucks, R. G., R. M. Reed, S. C. Ruppel, and U. Hammes (2012), Spectrum of pore types and networks in mudrocks and a descriptive classification for matrix-related mudrock pores, *AAPG bulletin*, *96*(6), 1071-1098.

Lucia, F. J. (1983), Petrophysical Parameters Estimated from Visual Descriptions of Carbonate Rocks - a Field Classification of Carbonate Pore-Space, *Journal of Petroleum Technology*, *35*(3), 629-637.

Lucia, F. J. (1995), Rock-Fabric Petrophysical Classification of Carbonate Pore-Space for Reservoir Characterization, *AAPG bulletin*, *79*(9), 1275-1300.

Lucia, F. J. (2007), *Carbonate reservoir characterization: an integrated approach*, 28-62, Springer Science & Business Media.

Luo, Y., and G. Zhang (1998), *Theory and application of spectral induced polarization*, 22-89 pp., Society of Exploration Geophysicists Tulsa.

Mailhiot, S. E., N. H. Williamson, J. R. Brown, J. D. Seymour, S. L. Codd, and R. K. June (2017), T 1–T 2 correlation and biopolymer diffusion within human osteoarthritic cartilage measured with nuclear magnetic resonance, *Applied Magnetic Resonance*, *48*(4), 407-422.

Marschall, D., J. Gardner, D. Mardon, and G. Coates (1995), Method for correlating NMR relaxometry and mercury injection data, paper presented at 1995 SCA Conference, paper.

Martinez, A. M., and A. C. Kak (2001), PCA versus LDA, *IEEE Transactions on Pattern Analysis and Machine Intelligence*, *23*(2), 228-233.

Mathisen, T., S. H. Lee, and A. Datta-Gupta (2001), Improved permeability estimates in carbonate reservoirs using electrofacies characterization: A case study of the North Robertson unit, west Texas, paper presented at SPE Permian Basin Oil and Gas Recovery Conference, Society of Petroleum Engineers.

Mazzullo, S. (2004), Overview of porosity evolution in carbonate reservoirs, *Kansas Geological Society Bulletin*, *79*(1/2), 20-28.

Mehana, M., and I. El-monier (2016), Shale characteristics impact on Nuclear Magnetic Resonance (NMR) fluid typing methods and correlations, *Petroleum*, *2*(2), 138-147.

Meiboom, S., and D. Gill (1958), Modified spin-echo method for measuring nuclear relaxation times, *Review of scientific instruments*, *29*(8), 688-691.

Melim, L. A. (2001), *The importance of pore type on permeability of Neogene carbonates, Great Bahama Bank*, 217-238 pp., SEPM Special Publication.

Menke, H. P., M. G. Andrew, M. J. Blunt, and B. Bijeljic (2016), Reservoir condition imaging of reactive transport in heterogeneous carbonates using fast synchrotron tomography — Effect of initial pore structure and flow conditions, *Chemical Geology*, *428*, 15-26.

Milliken, K. L., and M. E. Curtis (2016), Imaging pores in sedimentary rocks: Foundation of porosity prediction, *Marine and Petroleum Geology*, *73*, 590-608.

Milner, M., R. McLin, and J. Petriello (2013), Imaging Texture and Porosity in Mudstones and Shales: Comparison of Secondary and Ion-Milled Backscatter SEM Methods, in *Canadian Unconventional Resources and International Petroleum Conference*, edited, Society of Petroleum Engineers, Calgary, Alberta, Canada.

Moore, C. H. (2001), *Carbonate Reservoirs: Porosity, Evolution & Diagenesis in a Sequence Stratigraphic Framework*, 69-74, Elsevier.

Moore, R. C. (1949), *Divisions of the Pennsylvanian system in Kansas*, University of Kansas publications.

Morriss, C., J. Maclnnis, R. Freedman, J. Smaardyk, C. Straley, W. Kenyon, H. Vinegar, and P. Tutunjian (1993), Field test of an experimental pulsed nuclear magnetism tool, paper presented at SPWLA 34th Annual Logging Symposium, Society of Petrophysicists and Well-Log Analysts.

Mualem, Y. (1976), A new model for predicting the hydraulic conductivity of unsaturated porous media, *Water Resources Research*, *12*(3), 513-522.

Müller-Huber, E., F. Börner, J. H. Börner, and D. Kulke (2018), Combined interpretation of NMR, MICP, and SIP measurements on mud-dominated and grain-dominated carbonate rocks, *Journal of Applied Geophysics*, *159*, 228-240.

Müller-Huber, E., J. Schön, and F. Börner (2016), Pore space characterization in carbonate rocks—Approach to combine nuclear magnetic resonance and elastic wave velocity measurements, *Journal of Applied Geophysics*, *127*, 68-81.

Nashawi, I. S., and A. Malallah (2009), Improved Electrofacies Characterization and Permeability Predictions in Sandstone Reservoirs Using a Data Mining and Expert System Approach, *Petrophysics*, *50*(3), 250-268.

Niu, Q. F., M. Prasad, A. Revil, and M. Saidian (2016), Textural control on the quadrature conductivity of porous media, *Geophysics*, *81*(5), E297-E309.

Niu, Q. F., and A. Revil (2015), Connecting complex conductivity spectra to mercury porosimetry of sedimentary rocks, *Geophysics*, *81*(1), E17-E32.

Niu, Q. F., and C. Zhang (2018a), Joint inversion of NMR and SIP data to estimate pore size distribution of geomaterials, *Geophysical Journal International*, *212*(3), 1791-1805.

Niu, Q. F., and C. Zhang (2018b), Physical Explanation of Archie's Porosity Exponent in Granular Materials: A Process-Based, Pore-Scale Numerical Study, *Geophysical Research Letters*, *45*(4), 1870-1877.

Or, D., and M. Tuller (1999), Liquid retention and interfacial area in variably saturated porous media: Upscaling from single-pore to sample-scale model, *Water Resources Research*, *35*(12), 3591-3605.

Osterman, G., K. Keating, A. Binley, and L. Slater (2016), A laboratory study to estimate pore geometric parameters of sandstones using complex conductivity and nuclear magnetic resonance for permeability prediction, *Water Resources Research*, *52*(6), 4321-4337.

Perez, H. H., A. Datta-Gupta, and S. Mishra (2005), The role of electrofacies, lithofacies, and hydraulic flow units in permeability predictions from well logs: a comparative analysis using classification trees, *SPE Reservoir Evaluation & Engineering*, *8*(02), 143-155.

Poupon, A., W. R. Hoyle, and A. W. Schmidt (1971), Log Analysis in Formations with Complex Lithologies, *Journal of Petroleum Technology*, *23*(Aug), 995-&.

Qi, L., and T. R. Carr (2006), Neural network prediction of carbonate lithofacies from well logs, Big Bow and Sand Arroyo Creek fields, Southwest Kansas, *Computers & Geosciences*, *32*(7), 947-964.

Ragland, D. A. (2002), Trends In Cementation Exponents (m) For Carbonate Pore Systems, *Petrophysics*, *43*(05), 17.

Ramakrishnan, T., R. Ramamoorthy, E. Fordham, L. Schwartz, M. Herron, N. Saito, and A. Rabaute (2001), A model-based interpretation methodology for evaluating carbonate reservoirs, paper presented at SPE Annual Technical Conference and Exhibition, Society of Petroleum Engineers.

Rankey, E. C., H. Goodner, and J. Doveton (2018), Depositional Architecture and Petrophysical Variability of an Oolitic Tidal Sand Shoal: Pennsylvanian (Missourian), Kansas, USA, *Journal of Sedimentary Research*, *88*(9), 1114-1131.

Revil, A. (2013), Effective conductivity and permittivity of unsaturated porous materials in the frequency range 1 mHz–1GHz, *Water Resources Research*, *49*(1), 306-327.

Revil, A., A. Binley, L. Mejus, and P. Kessouri (2015), Predicting permeability from the characteristic relaxation time and intrinsic formation factor of complex conductivity spectra, *Water Resources Research*, *51*(8), 6672-6700.

Revil, A., and N. Florsch (2010), Determination of permeability from spectral induced polarization in granular media, *Geophysical Journal International*, *181*(3), 1480-1498.

Revil, A., N. Florsch, and C. Camerlynck (2014a), Spectral induced polarization porosimetry, *Geophysical Journal International*, *198*(2), 1016-1033.

Revil, A., P. Kessouri, and C. Torres-Verdín (2014b), Electrical conductivity, induced polarization, and permeability of the Fontainebleau sandstone, *Geophysics*, *79*(5), D301-D318.

Revil, A., K. Koch, and K. Holliger (2012), Is it the grain size or the characteristic pore size that controls the induced polarization relaxation time of clean sands and sandstones?, *Water Resources Research*, *48*(5).

Robinson, J., L. Slater, A. Weller, K. Keating, T. Robinson, C. Rose, and B. Parker (2018), On Permeability Prediction From Complex Conductivity Measurements Using Polarization Magnitude and Relaxation Time, *Water Resources Research*, *54*(5), 3436-3452.

Rokach, L., and O. Maimon (2005), Clustering methods, in *Data mining and knowledge discovery handbook*, edited, pp. 321-352, Springer.

Roslin, A., and J. S. Esterle (2016), Electrofacies analysis for coal lithotype profiling based on high-resolution wireline log data, *Computers & Geosciences*, *91*, 1-10.

Ruppert, L. F., R. Sakurovs, T. P. Blach, L. He, Y. B. Melnichenko, D. F. R. Mildner, and L. Alcantar-Lopez (2013), A USANS/SANS Study of the Accessibility of Pores in the Barnett Shale to Methane and Water, *Energy & Fuels*, *27*(2), 772-779.

Santamarina, J. C., K. A. Klein, Y. H. Wang, and E. Prencke (2002), Specific surface: determination and relevance, *Canadian Geotechnical Journal*, *39*(1), 233-241.

Scott, J. B., and R. D. Barker (2003), Determining pore-throat size in Permo-Triassic sandstones from low-frequency electrical spectroscopy, *Geophysical Research Letters*, *30*(9).

Sharma, P., G. Mamgain, V. Bahuguna, and C. Lal (2011), Improved Permeability Estimates in Carbonate Reservoirs Using Electrofacies Characterization: A Case Study of Mumbai High South, paper presented at The 2nd South Asain Geoscience Conference and Exhibition, New Delhi, India.

Simpson, J., and H. Carr (1958), Diffusion and nuclear spin relaxation in water, *Physical Review*, *111*(5), 1201.

Slater, L. (2007), Near surface electrical characterization of hydraulic conductivity: From petrophysical properties to aquifer geometries—A review, *Surveys in Geophysics*, *28*(2-3), 169-197.

Slater, L., W. Barrash, J. Montrey, and A. Binley (2014), Electrical-hydraulic relationships observed for unconsolidated sediments in the presence of a cobble framework, *Water Resources Research*, *50*(7), 5721-5742.

Slater, L., D. Ntarlagiannis, and D. Wishart (2006), On the relationship between induced polarization and surface area in metal-sand and clay-sand mixtures, *Geophysics*, *71*(2), A1-A5.

Sloss, L. (1964), Tectonic cycles of the North American craton, paper presented at Symposium on cyclic sedimentation, University of Kansas Geological Survey Bulletin, Lawrence, Kansas.

Song, Y.-Q., L. Venkataramanan, M. Hürlimann, M. Flaum, P. Frulla, and C. Straley (2002), T1–T2 correlation spectra obtained using a fast two-dimensional Laplace inversion, *Journal of magnetic resonance*, *154*(2), 261-268.

Straley, C. (1997), An Experimental Investigation Of Methane In Rock Materials, in *SPWLA 38th Annual Logging Symposium*, edited, p. 14, Society of Petrophysicists and Well-Log Analysts, Houston, Texas.

Strange, J. H., M. Rahman, and E. G. Smith (1993), Characterization of porous solids by NMR, *Phys Rev Lett*, *71*(21), 3589-3591.

Thommes, M., K. Kaneko, A. V. Neimark, J. P. Olivier, F. Rodriguez-Reinoso, J. Rouquerol, and K. S. Sing (2015), Physisorption of gases, with special reference to the evaluation of surface area and pore size distribution (IUPAC Technical Report), *Pure and Applied Chemistry*, *87*(9-10), 1051-1069.

Timur, A. (1969), Pulsed nuclear magnetic resonance studies of porosity, movable fluid, and permeability of sandstones, *Journal of Petroleum Technology*, *21*(06), 775-786.

Timur, A. (1972), Nuclear magnetic resonance study of carbonate rocks, paper presented at SPWLA 13th Annual Logging Symposium, Society of Petrophysicists and Well-Log Analysts.

Tinni, A., C. Sondergeld, and C. Rai (2017), Investigation of 2 MHz NMR Measurements Sensitivity to Moveable, Bound and Structural Water in Shales, edited, Society of Petrophysicists and Well-Log Analysts.

Valvatne, P. H., M. Piri, X. Lopez, and M. J. Blunt (2005), Predictive pore-scale modeling of single and multiphase flow, in *Upscaling Multiphase Flow in Porous Media*, edited, pp. 23-41, Springer.

Van Der Maaten, L. (2009), Learning a parametric embedding by preserving local structure, paper presented at Artificial Intelligence and Statistics.

Van Geet, M., R. Swennen, and M. Wevers (2000), Quantitative analysis of reservoir rocks by microfocus X-ray computerised tomography, *Sedimentary Geology*, *132*(1), 25-36.

Van Genuchten, M. T. (1980), A closed-form equation for predicting the hydraulic conductivity of unsaturated soils 1, *Soil science society of America journal*, *44*(5), 892-898.

Vinegar, H. J., and M. H. Waxman (1984), Induced Polarization of Shaly Sands, *Geophysics*, *49*(8), 1267-1287.

Wadell, H. (1932), Volume, shape, and roundness of rock particles, *Journal of Geology*, *40*(5), 443-451.

Walter, L. M., and J. W. Morse (1984), Reactive Surface-Area of Skeletal Carbonates during Dissolution - Effect of Grain-Size, *Journal of Sedimentary Petrology*, *54*(4), 1081-1090.

Washburn, K. E., and J. E. Birdwell (2013), Updated methodology for nuclear magnetic resonance characterization of shales, *Journal of magnetic resonance*, *233*, 17-28.

Watney, W. L. (1980), *Cyclic Sedimentation of the Lansing-Kansas City Groups in Northwestern Kansas and Southwestern Nebraska: A Guide for Petroleum Exploration*, Kansas Geological Survey, University of Kansas.

Watney, W. L., J. A. French, and E. K. Franseen (1989), Sequence Stratigraphic Interpretations and Modeling of Cyclothems in the Upper Pennsylvanian (Missourian), Lansing and Kansas City Groups in Eastern Kansas: Guidebook, 41st Annual Field Conference.

Watney, W. L., W. J. Guy, and A. P. Byrnes (2001), Characterization of the Mississippian chat in south-central Kansas, *AAPG bulletin*, *85*(1), 85-113.

Watney, W. L., and S. E. Paul (1983), Oil exploration and production in Kansas: present activity, future potential, paper presented at Kansas Univ. Tertiary Oil Recovery Conference;(United States).

Weller, A., S. Nordsiek, and W. Debschütz (2010a), Estimating permeability of sandstone samples by nuclear magnetic resonance and spectral-induced polarization, *Geophysics*, *75*(6), E215-E226.

Weller, A., L. Slater, S. Nordsiek, and D. Ntarlagiannis (2010b), On the estimation of specific surface per unit pore volume from induced polarization: A robust empirical relation fits multiple data sets, *Geophysics*, *75*(4), Wa105-Wa112.

Westphal, H., I. Surholt, C. Kiesl, H. F. Thern, and T. Kruspe (2005), NMR Measurements in Carbonate Rocks: Problems and an Approach to a Solution, *pure and applied geophysics PAGEOPH*, *162*(3), 549-570.

Xu, P., and B. Yu (2008), Developing a new form of permeability and Kozeny–Carman constant for homogeneous porous media by means of fractal geometry, *Advances in water resources*, *31*(1), 74-81.

Xu, W., J. T. Ok, F. Xiao, K. B. Neeves, and X. Yin (2014), Effect of pore geometry and interfacial tension on water-oil displacement efficiency in oil-wet microfluidic porous media analogs, *Physics of Fluids*, *26*(9), 093102.

Yao, Y., and D. Liu (2012), Comparison of low-field NMR and mercury intrusion porosimetry in characterizing pore size distributions of coals, *Fuel*, *95*, 152-158.

Yao, Y., D. Liu, Y. Che, D. Tang, S. Tang, and W. Huang (2010), Petrophysical characterization of coals by low-field nuclear magnetic resonance (NMR), *Fuel*, *89*(7), 1371-1380.

Zadeh, L. A. (1996), Fuzzy sets, in *Fuzzy Sets, Fuzzy Logic, And Fuzzy Systems: Selected Papers by Lotfi A Zadeh*, edited, pp. 394-432, World Scientific.

Zeller, D. E. (1968), Stratigraphic succession in Kansas, *Kansas Geological Survey Bulletin*, *189*, 81.

Zhang, F., Q. Niu, and C. Zhang (2018), Estimating pore-size distribution in carbonate reservoir rocks using joint inversion of NMR and complex conductivity data, in *SEG Technical Program Expanded Abstracts 2018*, edited, pp. 4909-4913.

Zhang, F., C. Zhang, and L. Watney (2017), Pore-structure characterization by combined laboratory nuclear magnetic resonance and spectral induced polarization: A case study of Kansas carbonates, in *SEG Technical Program Expanded Abstracts 2017*, edited, pp. 5432-5437.

Zhou, D. G., and M. Blunt (1997), Effect of spreading coefficient on the distribution of light non-aqueous phase liquid in the subsurface, *Journal of Contaminant Hydrology*, *25*(1-2), 1-19.

Figures

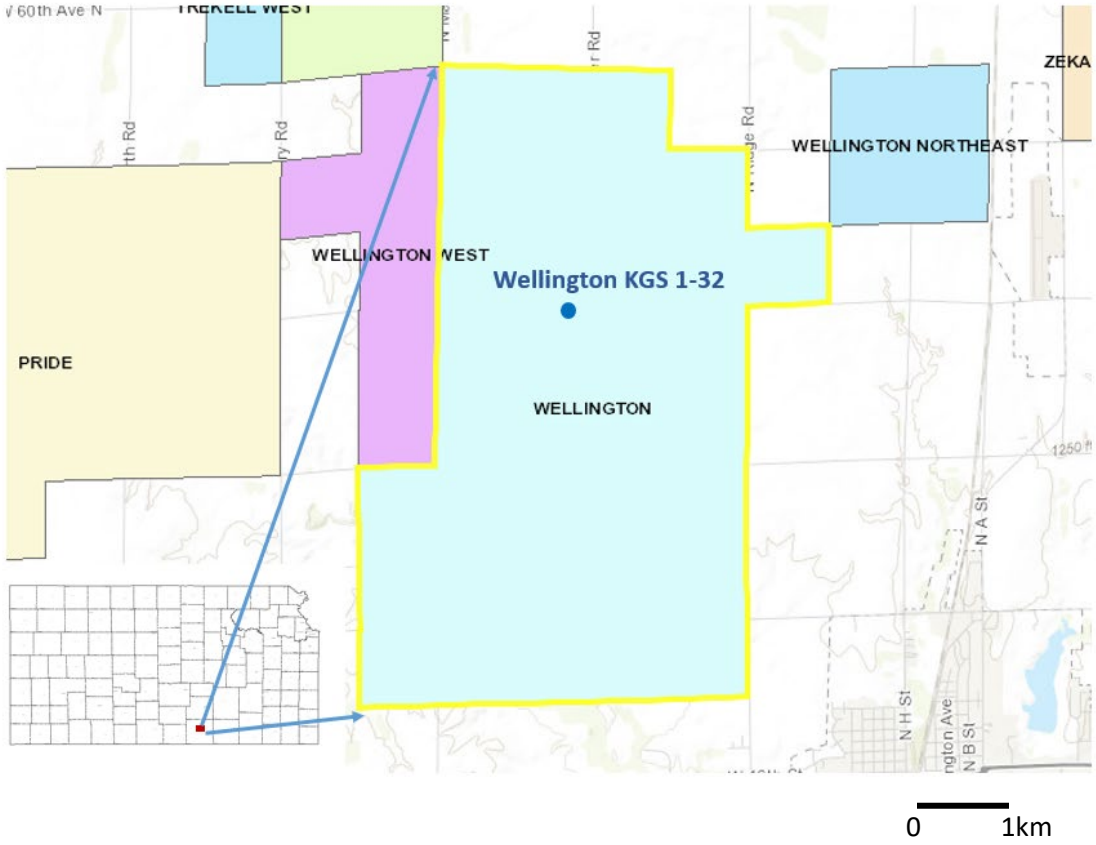

Figure 2.1. The location of well Wellington KGS 1-32 presented on a Kansas map. The light blue area with yellow outlines is the Wellington oil and gas field. The blue dot marks the location of Wellington KGS 1-32.

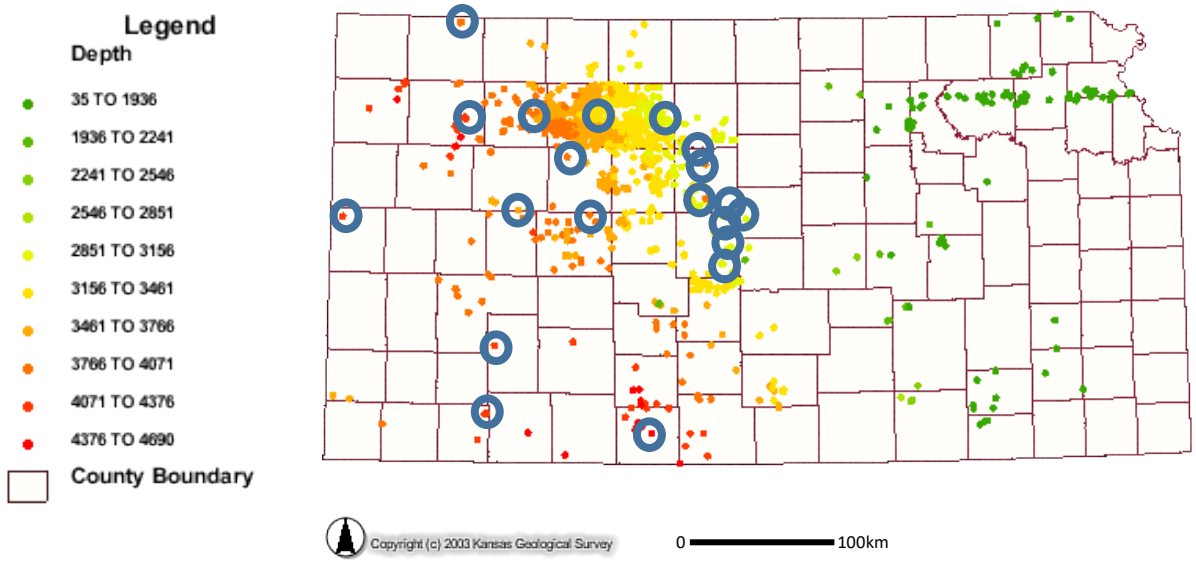

Figure 2.2. Well top map for Lansing-Kansas City Group (1524 Wells) in Kansas, generated by Kansas Well Top Stratigraphy Viewer (currently retired). The blue circles here mark out 20 wells from which LKC samples analyzed in this work.

Grainstone 1

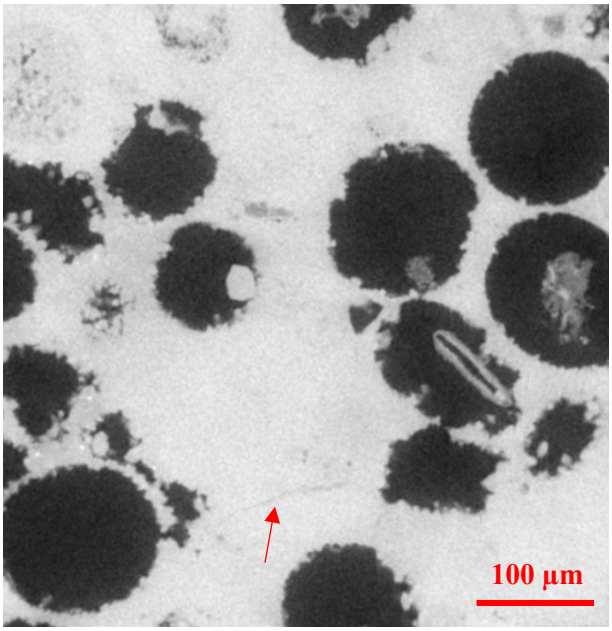

Grainstone 2

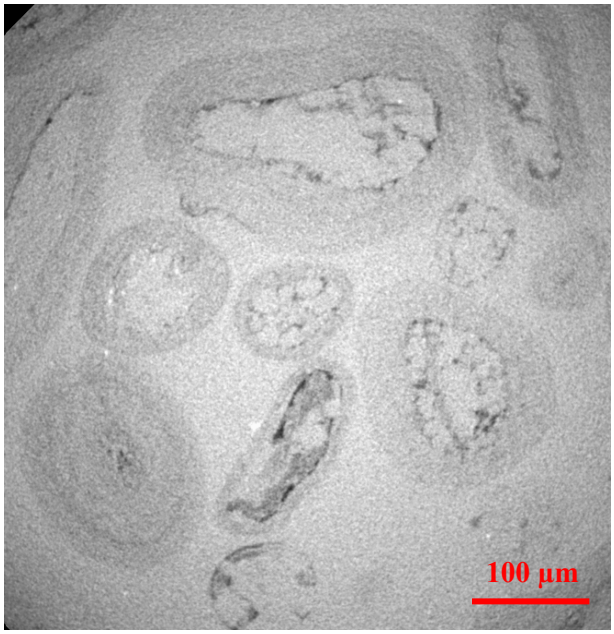

Packstone

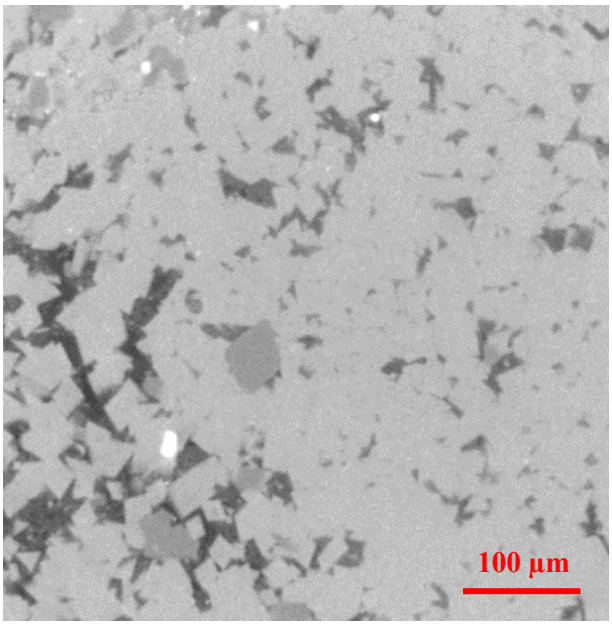

Mudstone

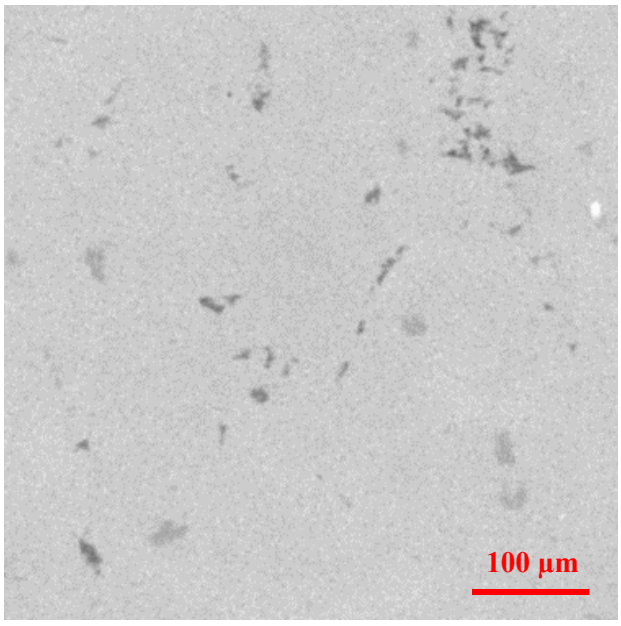

Figure 4.1. µ-CT images of two grainstone samples (a,b), one packstone sample (c) and one mudstone sample (d). All images have pixel size of 1.69 µm, and the intensity of each pixel in grayscale (0-255, darkest to lightest) represents the hardness. Darker shades represents softer

material, whereas lighter shades represent harder material. In these images, dark regions indicate pore space and light regions indicate solid. The X-ray strengths applied to each sample are different, so thresholds for recognizing different materials are different in each image. For example, pore regions in c) are more dark gray than black, in comparison to the pore regions in a). See text for detailed description of these images. Note the different size and abundances of pores among different textures observed here.

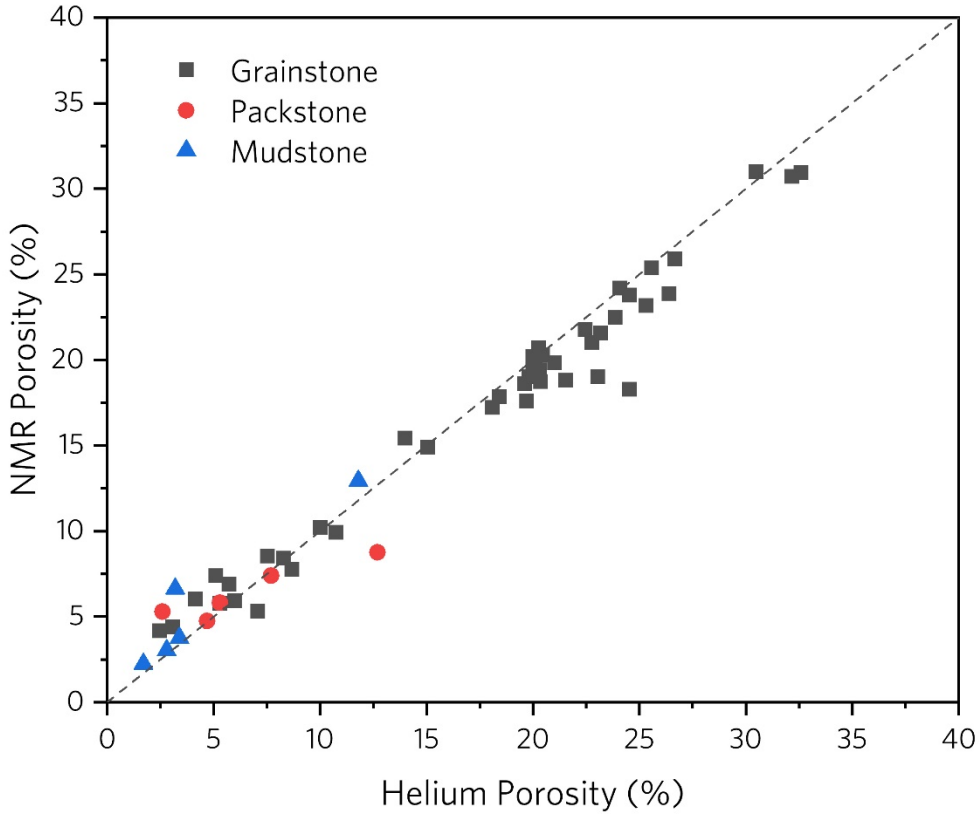

Figure 4.2. The relation between routine helium porosity (%) from specific core analysis (SCA) and NMR porosity (%) estimated from equivalent fluid content. The dashed line which is 1:1 line also shows in the figure with R^2=0.90, P<0.0001. Note that NMR porosity seems to measure porosity slightly higher than helium porosity at low porosity (<10%) and under predict porosity at high porosity (>20%), a difference related to the selected echo time (see discussion in text).

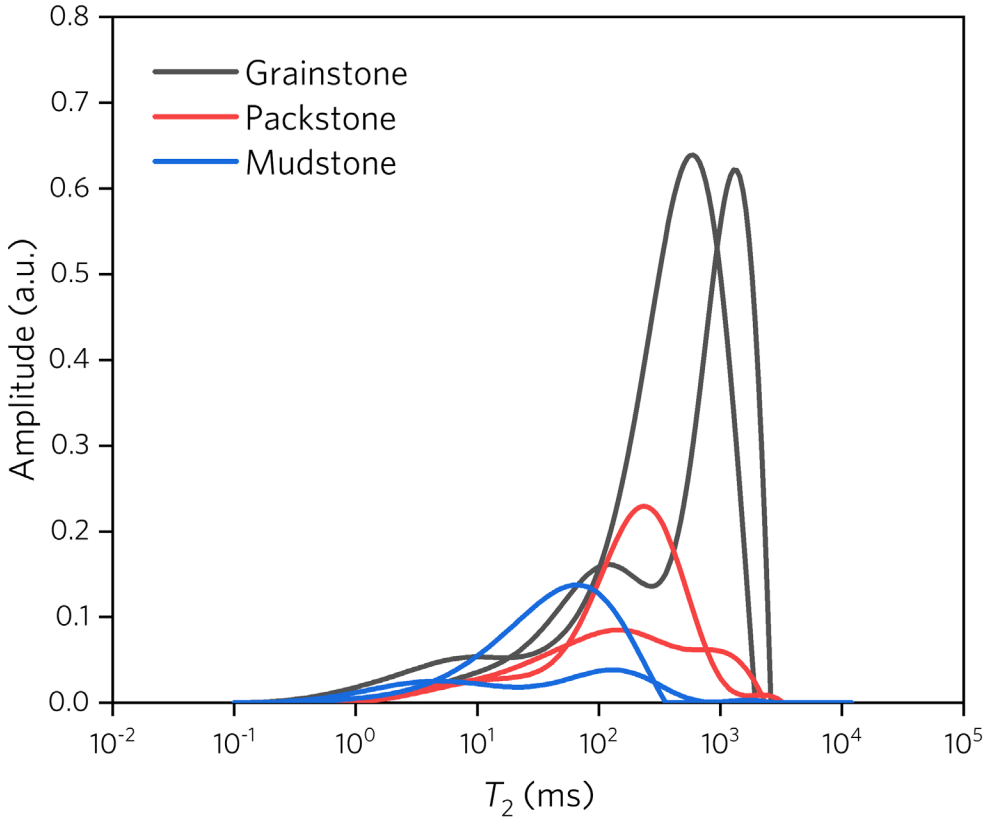

Figure 4.3. The T_2 distribution of representative core samples of grainstone, packstone and mudstone. For each lithofacies, there are two samples: one with unimodal distribution and another with bimodal distribution. The amplitude represents signal strength for each T_2 time, and is normalized by total signal strength of grainstone sample. Note that grainstones have higher peak amplitude values and longer T_2 than packstones, than mudstones.

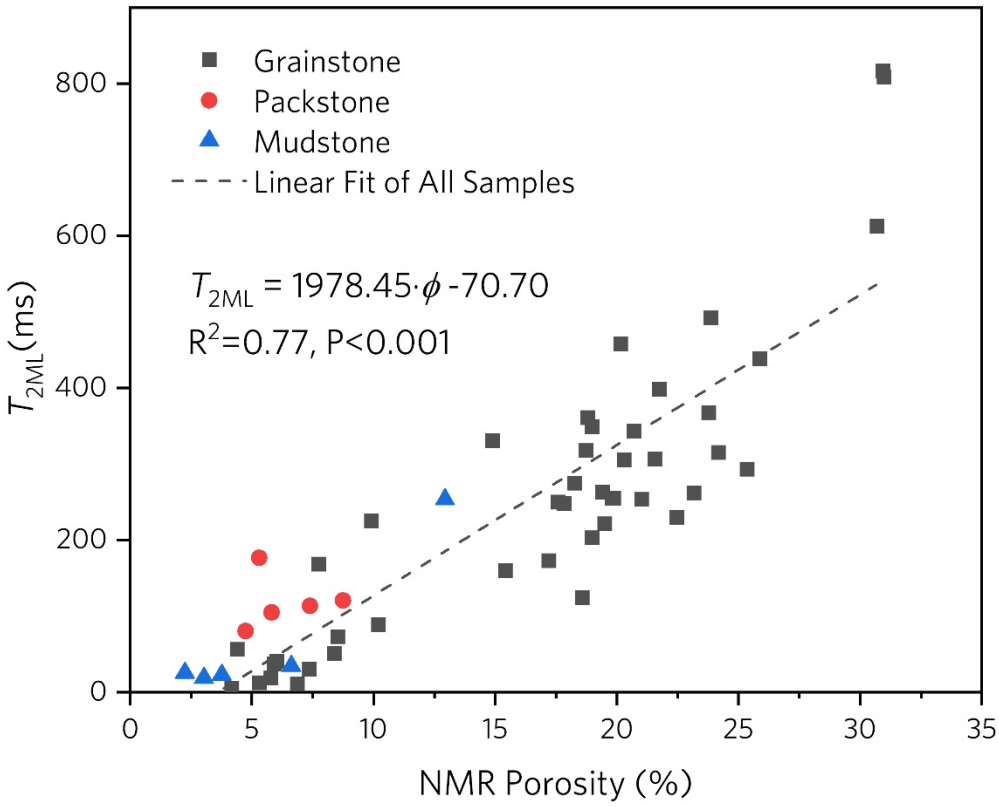

Figure 4.4. The relation between porosity estimated from NMR and T_{2ML} for samples of this study, noted by lithology (grainstone, packstone, and mudstone). The T_{2ML} is correlated positively with NMR porosity (R^2=0.77, P <0.001).

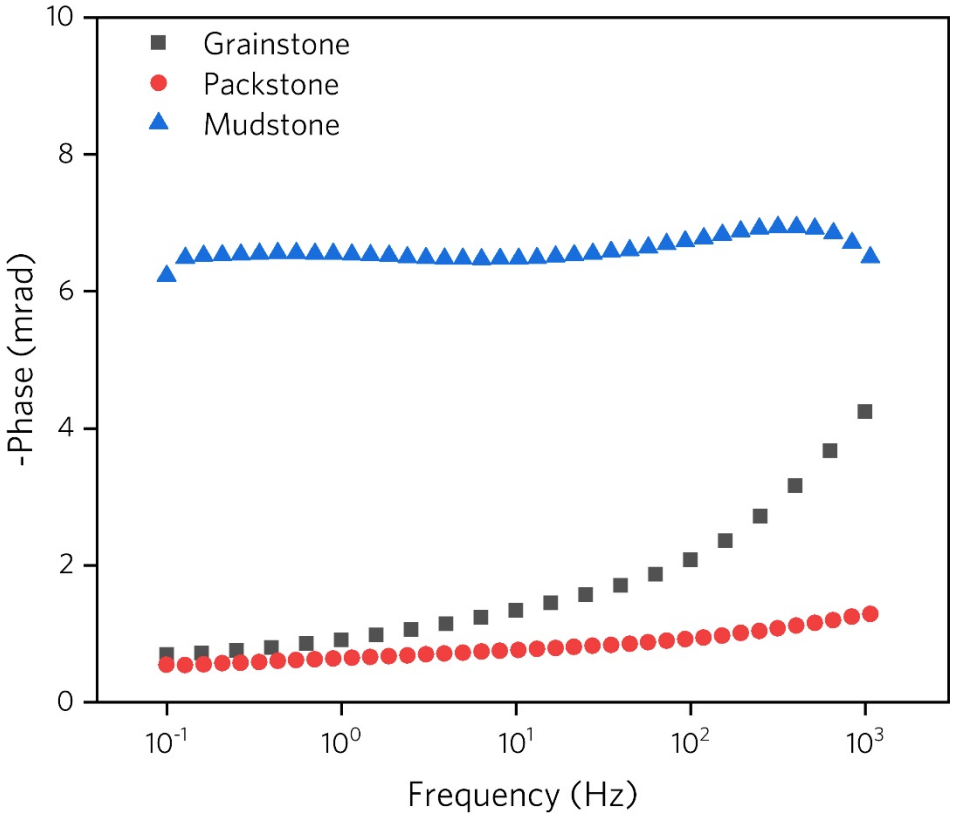

Figure 4.5. The frequency-dependent phase shift spectrum for three representative samples. The pore-fluid conductivity σ_w is 0.12 S/m (NaCl, 24 °C). Note that there are no visible peak values for phase shift spectrums. Phase shift of mudstone is higher than packstone and grainstone. The flat spectrum of mudstone are interpreted to indicate broad pore-size distribution [*A Revil*, 2013] and low chargeability of carbonate samples at low pore-fluid salinity [*Cerepi*, 2004]. The increasing phase shift of packstone and grainstone following by the frequency increasing indicate potential peak values at higher frequency (>1000 Hz), which is interpreted to be related to small-size pores (with radius < 1nm) [*Müller-Huber et al.*, 2018].

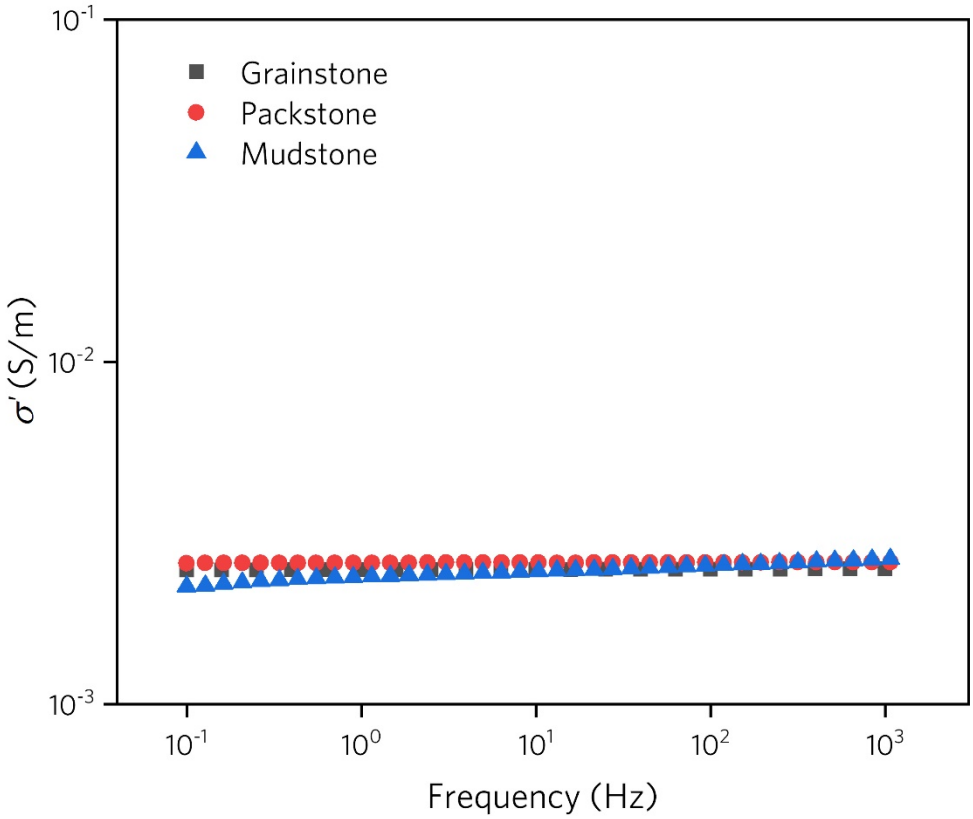
Grainstone
Packstone
Mudstone
σ' (S/m)
10-1
10-2
10-3
10-1
100
101
102
103
Frequency (Hz)

Figure 4.6 a)

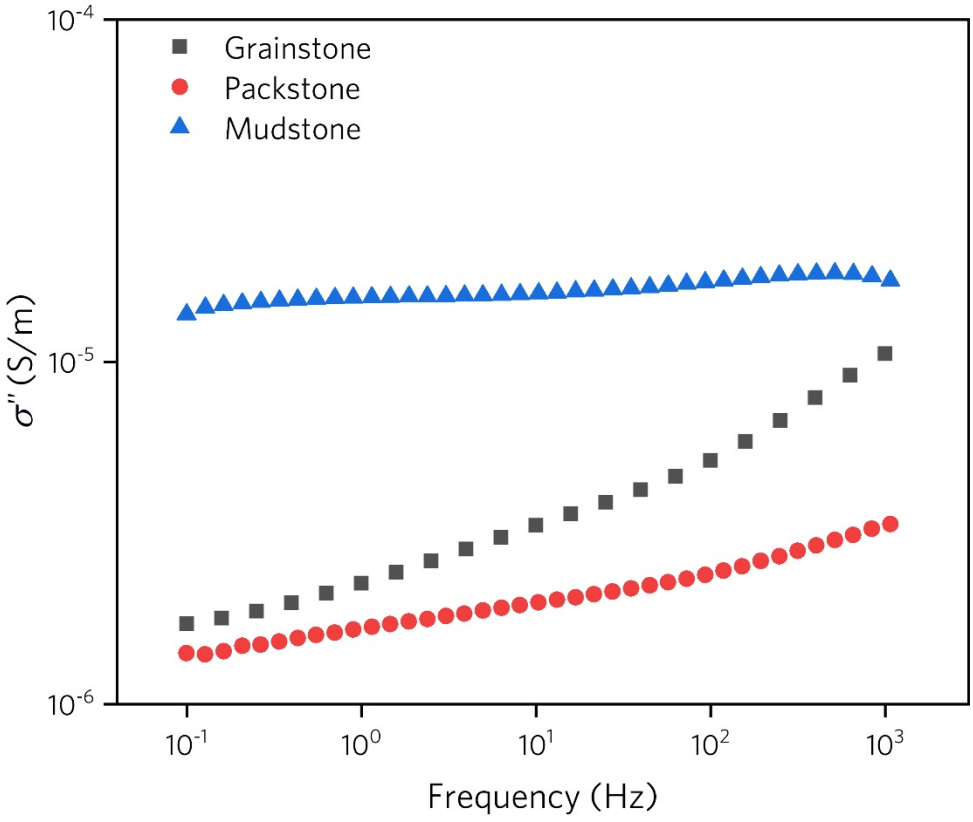

Figure 4.6 b)

Figure 4.6. The frequency-dependent complex conductivity spectrums for the same three representative samples illustrated in Figure 4.5. a) The frequency-dependent real part of conductivity σ' of grainstone, packstone mudstone; b) The frequency-dependent imaginary part of conductivity σ'' of grainstone, packstone, mudstone. The pore-fluid conductivity σ_w is 0.12 S/m (NaCl, 24 °C). Note that relative small difference are observed in σ' comparing to the difference of σ'' among three lithofacies. Mudstone has the highest σ'' value and is one order of magnitude larger than packstone and grainstone in low frequency end (0.1 Hz). Also note that shape of σ'' spectrums are similar to phase shift spectrums in where mudstone exhibit a plat plateau while packstone and grainstone have σ'' rise with frequency increasing.

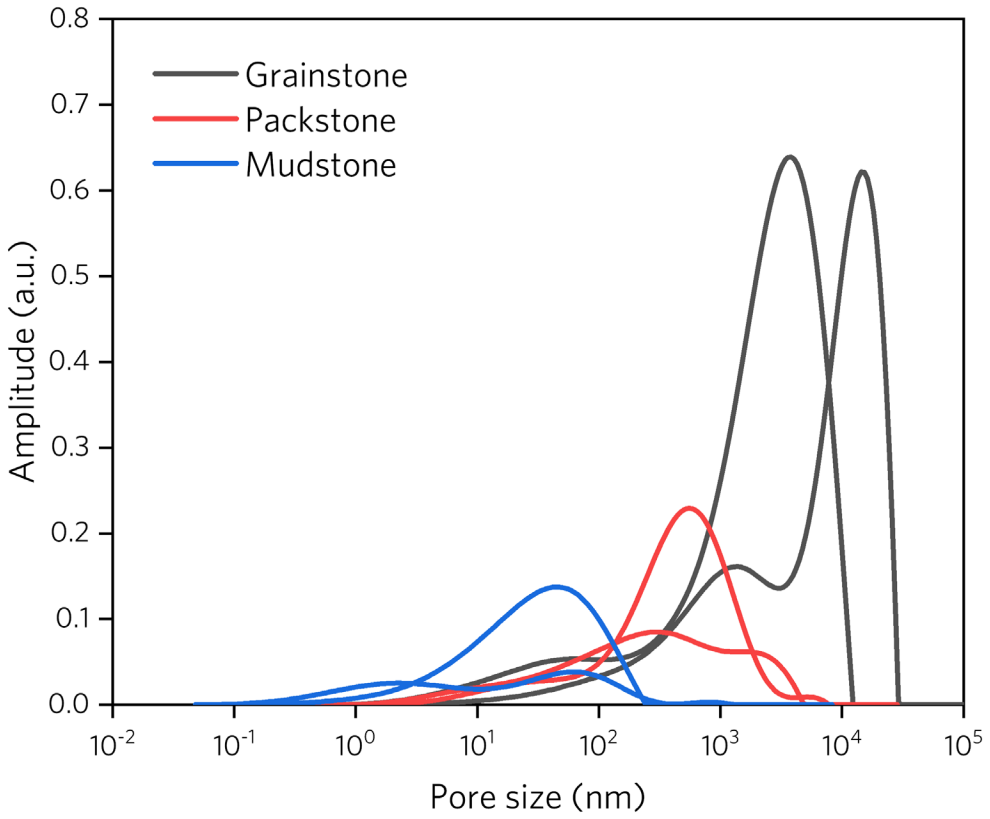

Figure 4.7. The pore size distribution of same representative core samples of grainstone, packstone and mudstone that be used in Figure 4.2. The amplitude represents signal strength for each pore size, and is normalized by total signal strength of grainstone sample. Note that the shape of pore size distribution is the same as T_2 distribution.

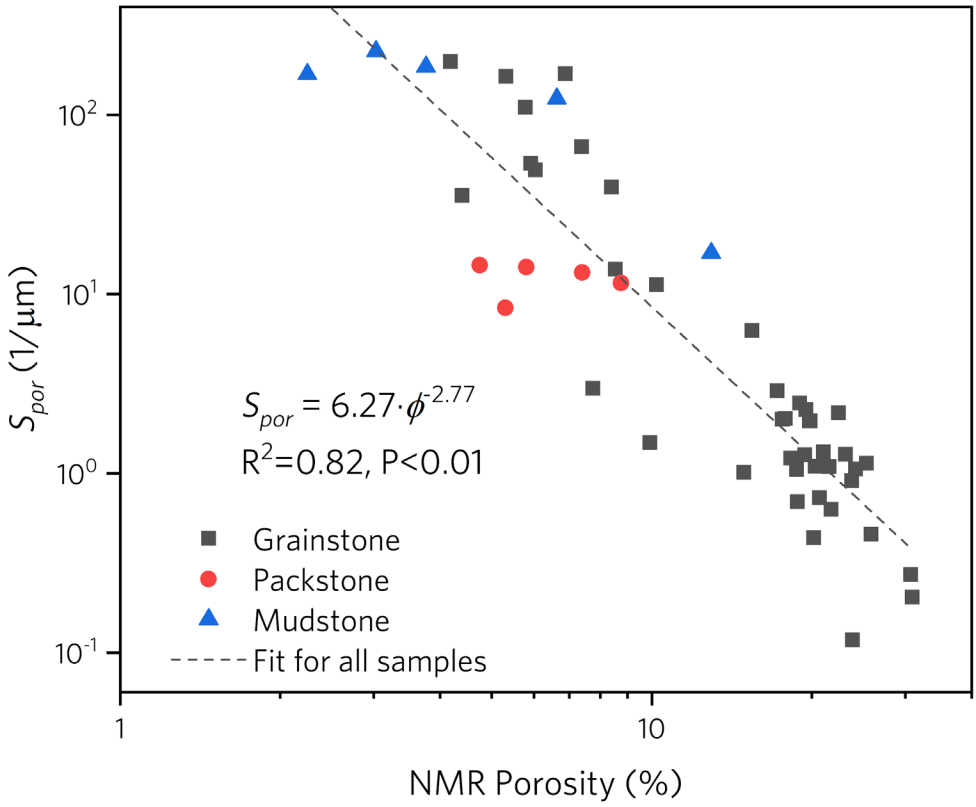

Figure 4.8. The relation between NMR porosity and S_{por}, both plotted on a log scale. Note the power-law correlation of S_{por} and porosity, for all three classes (R^2=0.82, P <0.01). The best-fit line of the dataset is presented as a dashed line.

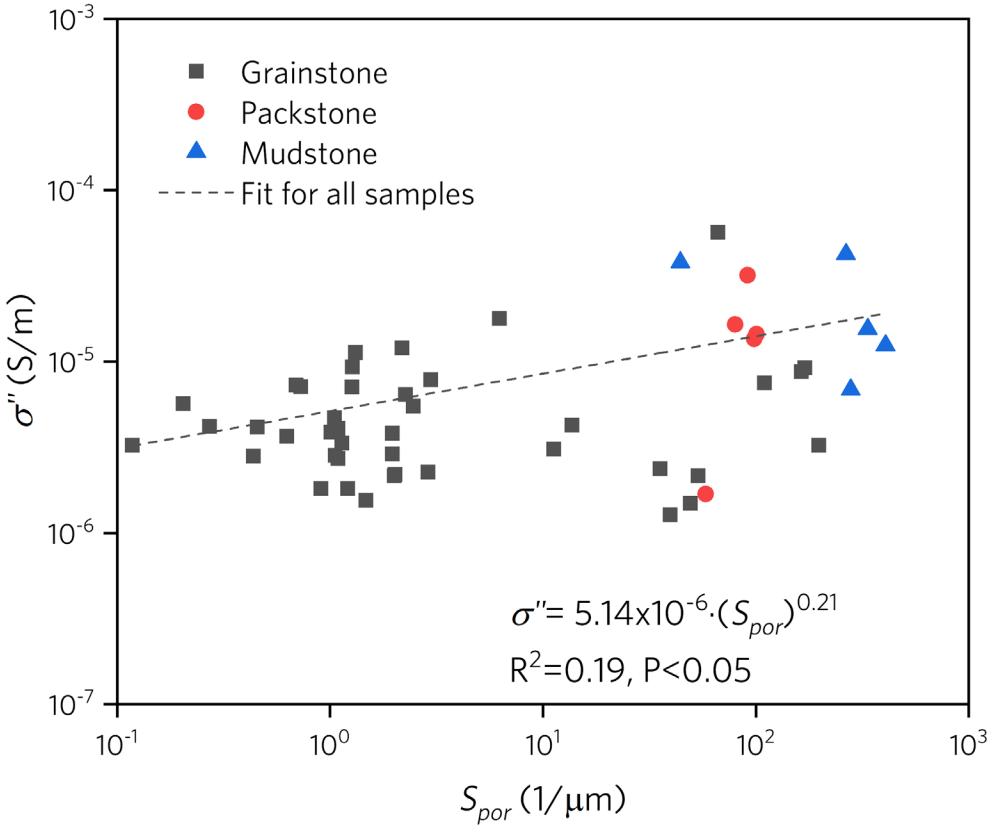

Figure 4.9. The relation between the surface-to-volume ratio S_{por} and imaginary part of conductivity σ"; both axes are plotted on a log scale. Note the power-law correlation of S_{por} and σ" (the linear trend in log-log space) (R^2=0.19, P <0.05). The best-fit line of the dataset is presented as a dashed line.

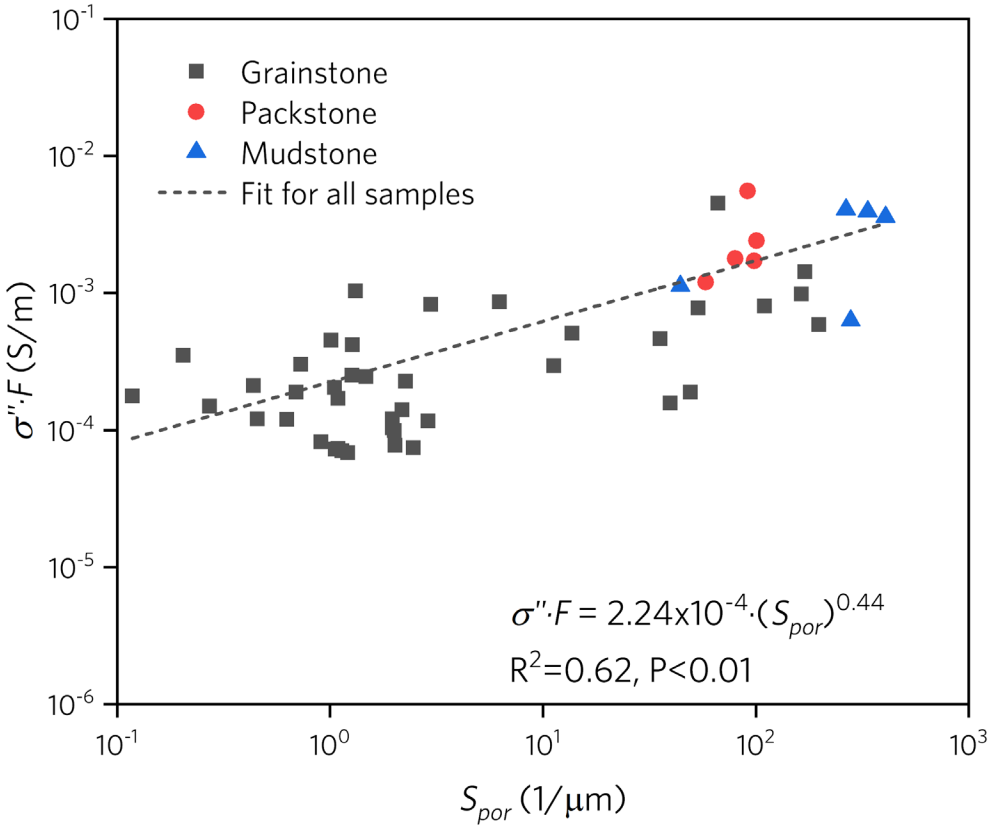

Figure 4.10. The relation between the surface to volume ratio S_{por} and imaginary part of conductivity σ'' multiplied by formation factor F. Note that, as in Figure 4.9, the best fit power-law relationship between S_{por} and $\sigma'' \cdot F$ is shown (dashed line) (R^2=0.62, P <0.01). Note the stronger correlation between S_{por} and $\sigma'' \cdot F$ than between S_{por} and σ''.

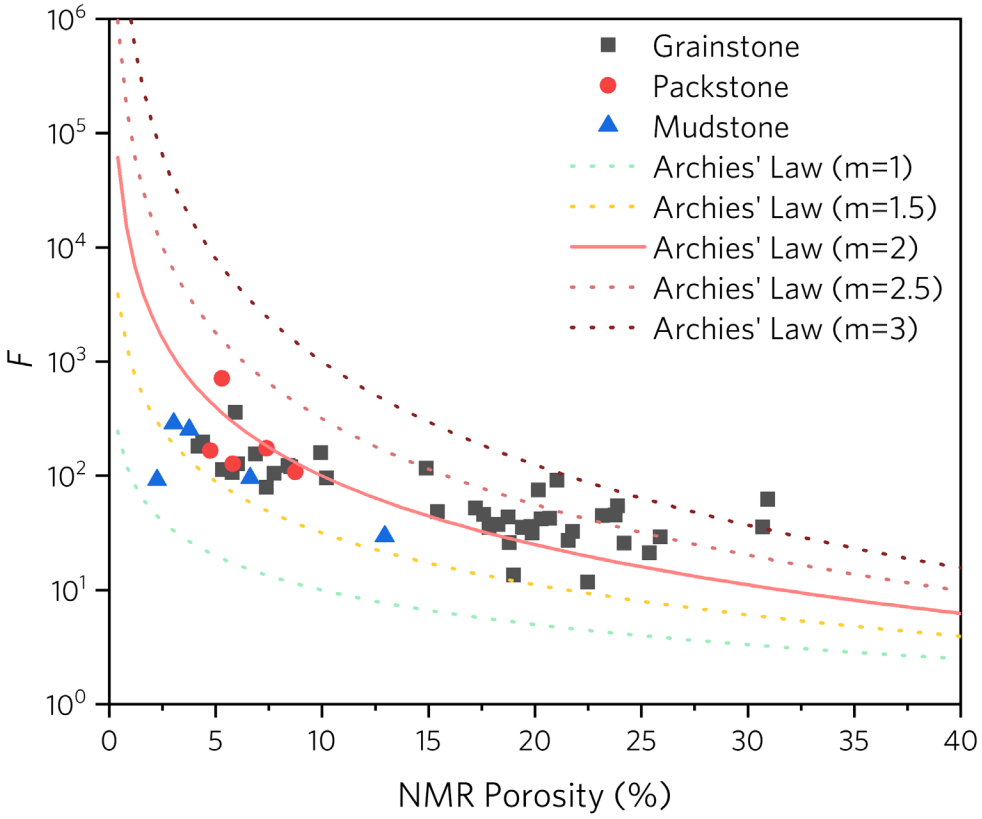

Figure 4.11. Cross plot of measured formation factor versus porosity; also superimposed are the theoretical formation factors calculated from conventional Archie's law with varying porosity exponent *m* (1 to 3). The solid line represents *m* calculated from Archie's law with the commonly applied porosity exponent *m* = 2. Dotted lines are Archie's law with alternate *m* values. Note that samples with lower porosities (<10%) have lower values than *F* that calculated from Archie's law with *m* = 2, whereas samples with higher porosities (>15%) have higher values than *F* that calculated from Archie's law with *m* = 2.

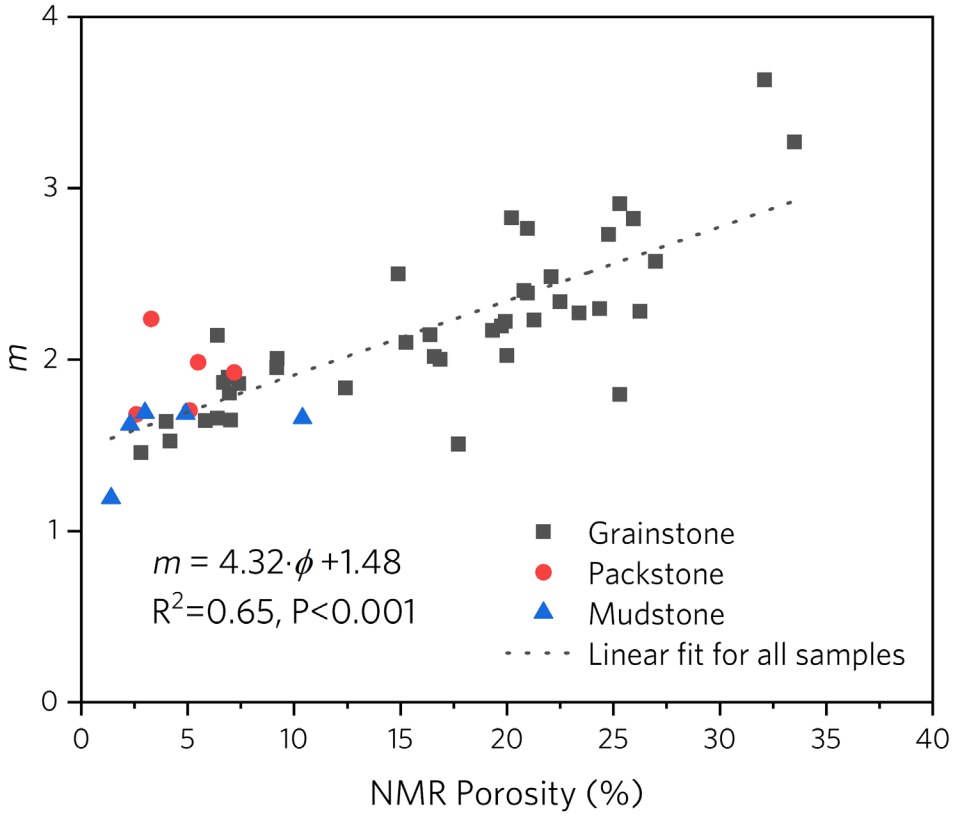

Figure 4.12. The relation between NMR porosity and measured porosity exponent *m* for all samples. Note the positive linear correlation between porosity exponent *m* and porosity. Note the solid curve on Figure 4.11 is equivalent to a straight line of *m* = 2 on this figure.

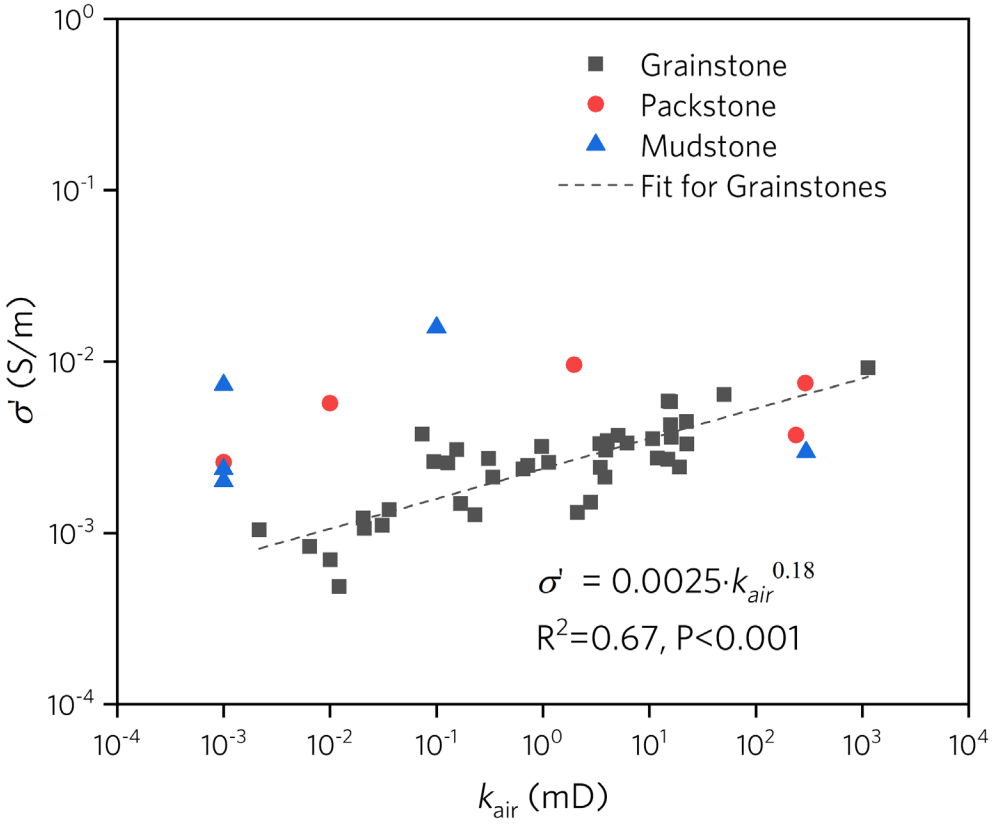

Figure 4.13. Cross plot illustrating relation between air permeability (corrected by Klinkenberg-correction factor) and real part of conductivity σ' (at 1 Hz) for grainstones, packstones and mudstones. Note the power-law correlation of S_{por} and σ' (the linear trend in log-log space) (R^2=0.67, P <0.001). The best-fit line of the grainstone samples is presented as a dashed line. Since S_{por} and σ' of mudstones and packstones have no significant correlations, only grainstone samples are used to fit the correlation equation.

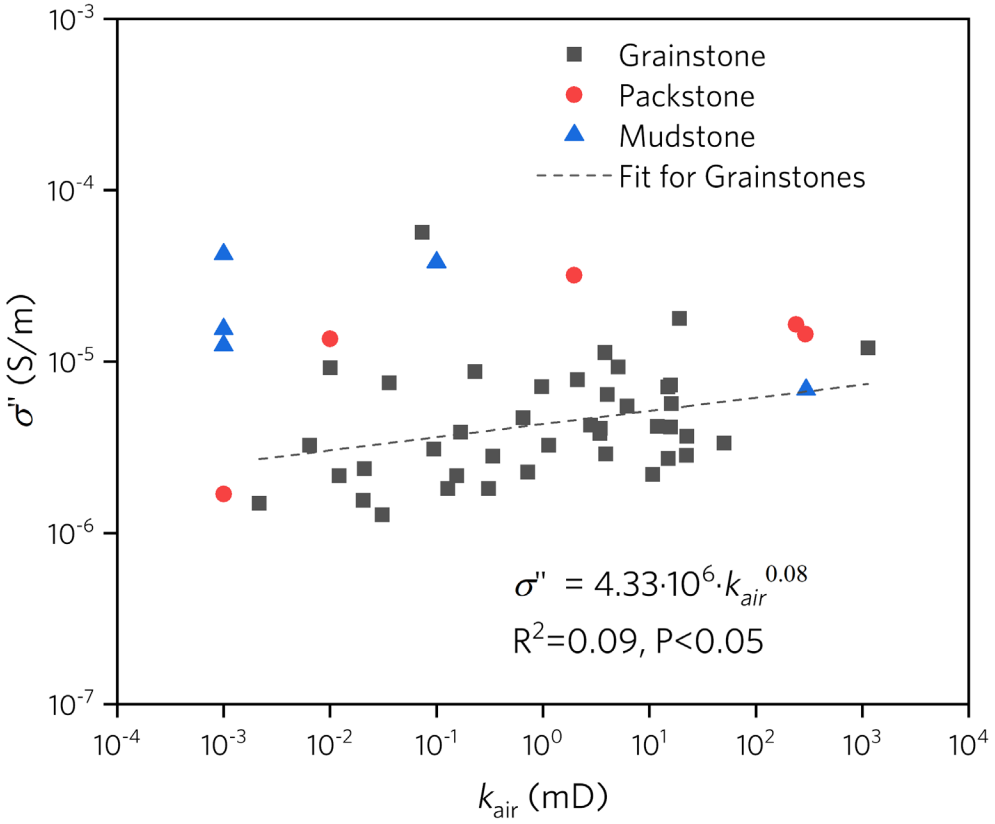

Figure 4.14. Cross plot illustrating relation between air permeability (corrected by Klinkenberg-correction factor) and the imaginary part of conductivity σ" (at 1Hz) for grainstones, packstones and mudstones. Note the power-law correlation of S_{por} and σ" (the linear trend in log-log space) (R^2=0.09, P <0.05). Since S_{por} and σ" of mudstones and packstones have no significant correlations, only grainstone samples are used to fit the correlation equation. The best-fit line of the grainstone dataset is presented as a dashed line.

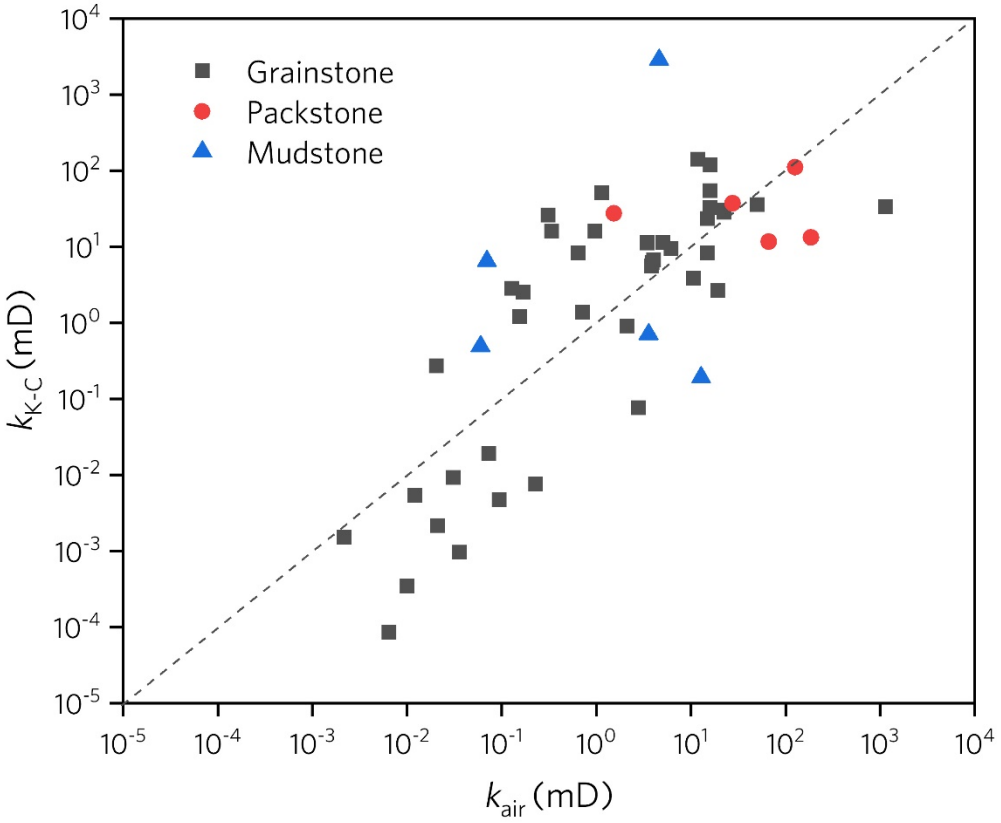

Figure 4.15. Measured air permeability (corrected by Klinkenberg-correction factor) , k_{air}, plotted against the permeability estimated by K-C equation k_{K-C}. The dashed line which is 1:1 line also shows in the figure with R^2=0.67, P<0.001. The high R^2 = 0.67 suggests a good agreement between the air permeability and K-C permeability.

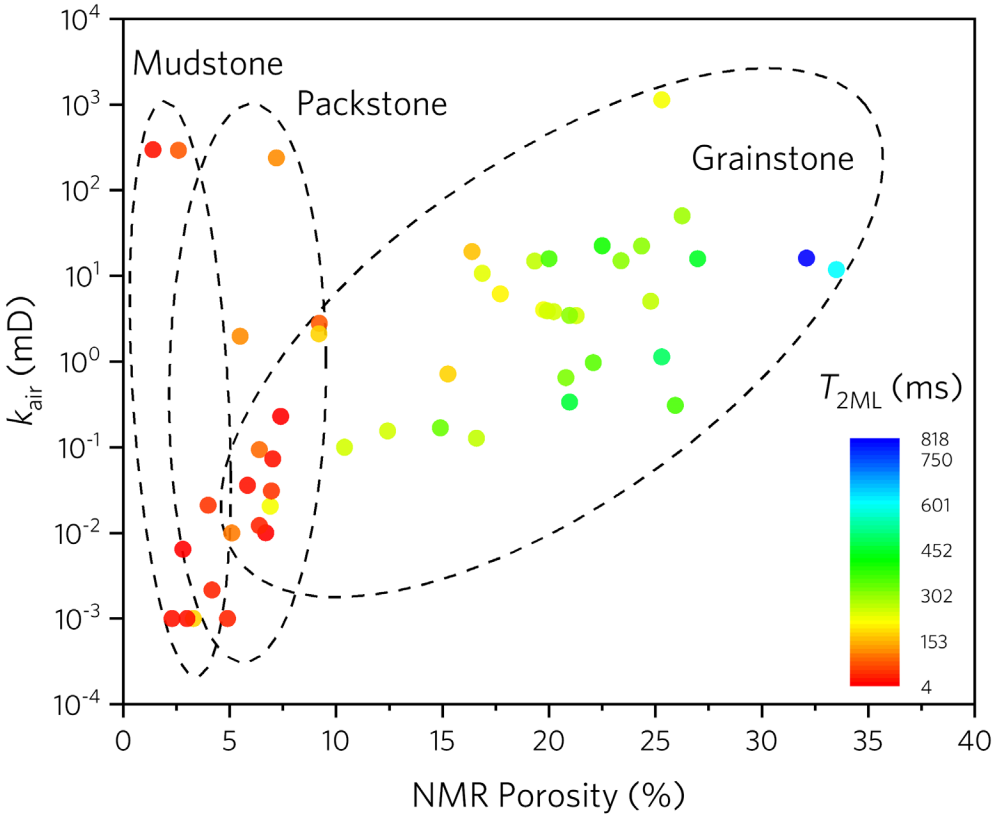

Figure 4.16. Cross plot of air permeability versus NMR porosity, with measured characteristic T_2 value T_{2ML} superimposed in color. Three ellipses outline samples of grainstone, packstone, and mudstone.

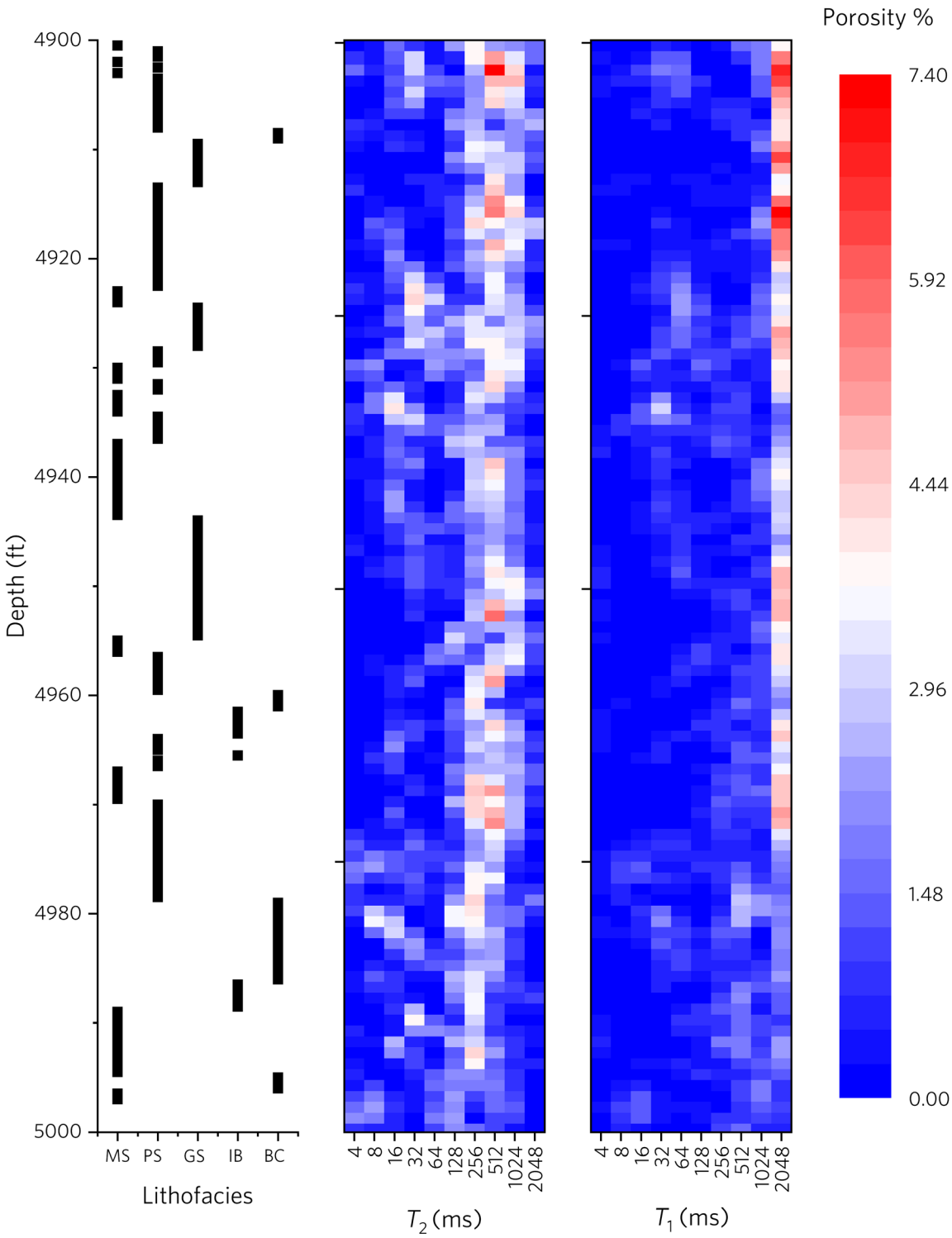
Porosity %
7.40
5.92
4.44
2.96
1.48
0.00
Depth (ft)
4900
4920
4940
4960
4980
5000
MS
PS
GS
IB
BC
Lithofacies
4
8
16
32
64
128
256
512
1024
2048
T_2 (ms)
T_1 (ms)

Figure 5.1. Lithofacies of samples (where MS = mudstone, PS = packstone, GS = grainstone, IB = incipient breccia, BC = breccia) from the interval of interest (4900-5000 ft) are listed in the order of depth along with the corresponding T_2 and T_1 distributions. Note that NMR relaxation data are subdivided into bins with 2^n ($n \epsilon [2,10]$) ms (as provided by the service company). Also note some samples are missing from the lithofacies (4901, 4920-4923, and 4997-5000 ft) which will be removed from the subsequent analyses.

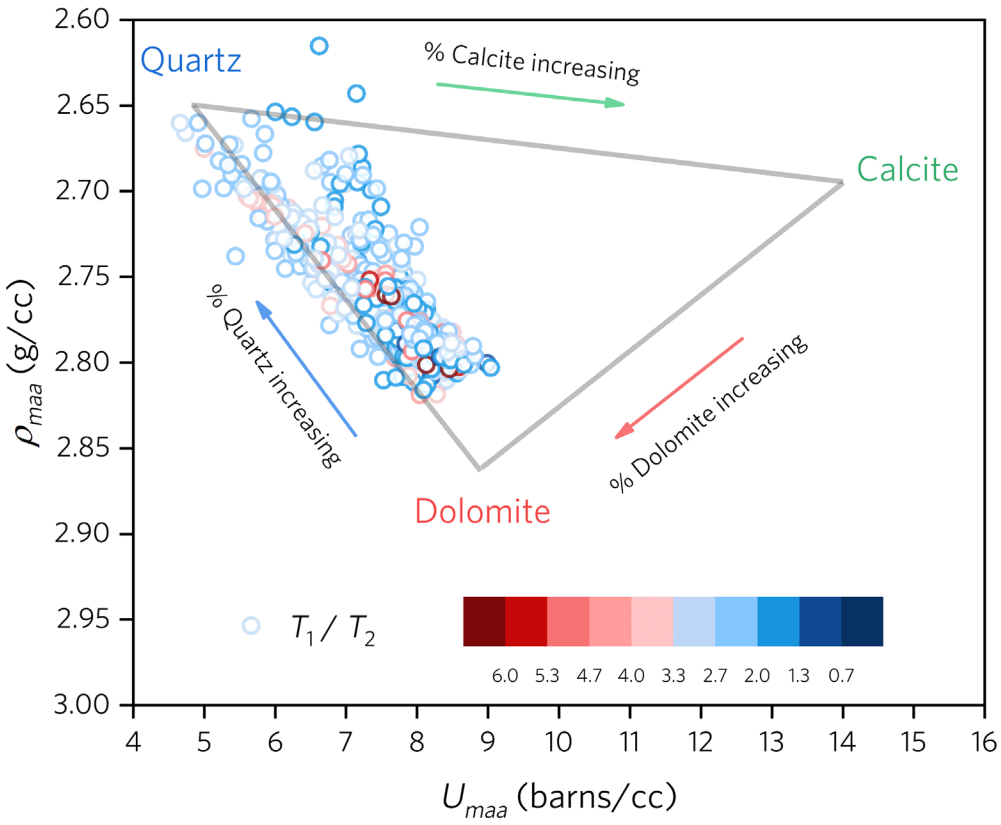
Quartz
% Calcite increasing
Calcite
% Quartz increasing
% Dolomite increasing
Dolomite
T_1 / T_2
6.0 5.3 4.7 4.0 3.3 2.7 2.0 1.3 0.7
ρ_{maa} (g/cc)
U_{maa} (barns/cc)
2.60
2.65
2.70
2.75
2.80
2.85
2.90
2.95
3.00
4 5 6 7 8 9 10 11 12 13 14 15 16

Figure 5.2 a)

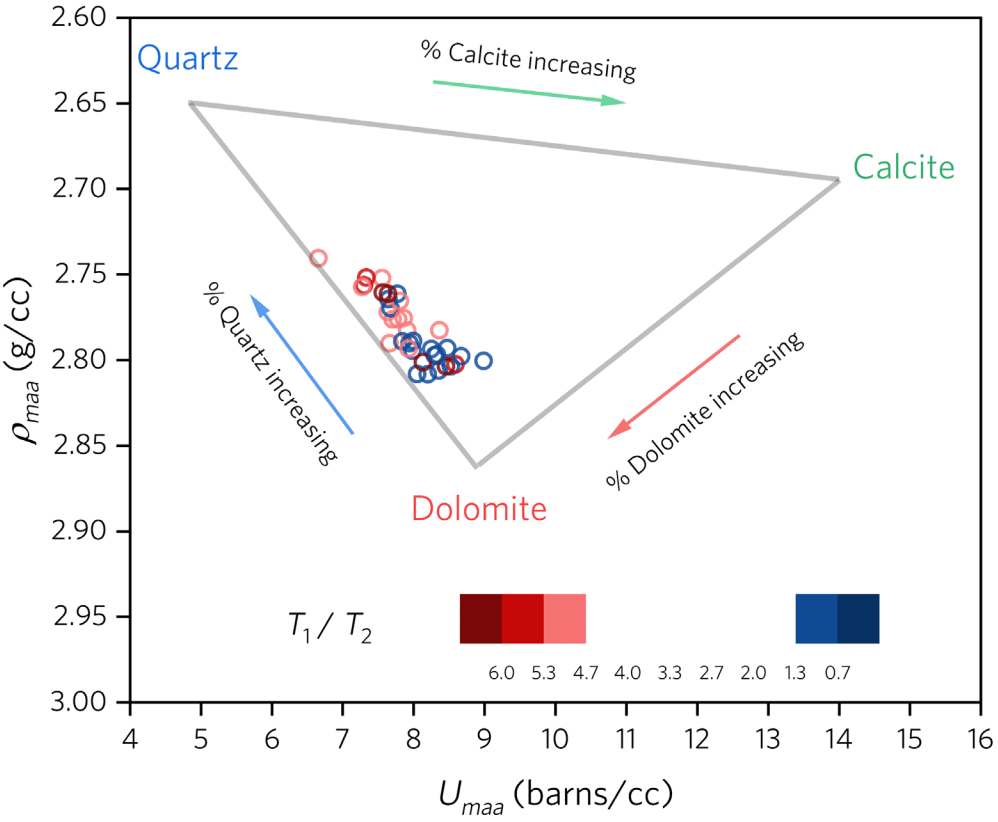

Figure 5.2 b)

Figure 5.2 a). $U_{maa} - \rho_{maa}$ crossplot (MID plot) with superimposed T_1/T_2. b) MID plot with only T_1/T_2 higher than 4.7 and lower than 1.3. T_1/T_2 ratios are presented by circles in color with a range from 0.66 to 7.44. Gray lines link mineral end members of a ternary mixture of quartz, calcite and dolomite. Arrows indicate an increasing percentage of the end-member minerals. Note the extreme values of high and low T_1/T_2 appear in high dolomite end.

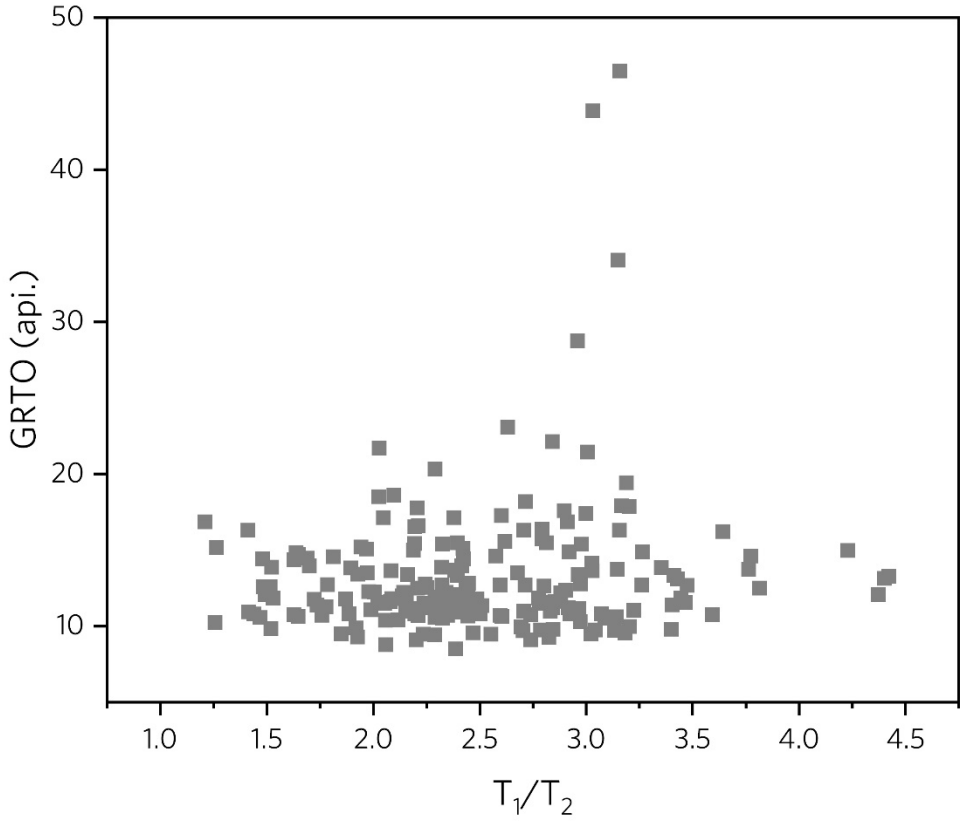

Figure 5.3 a).

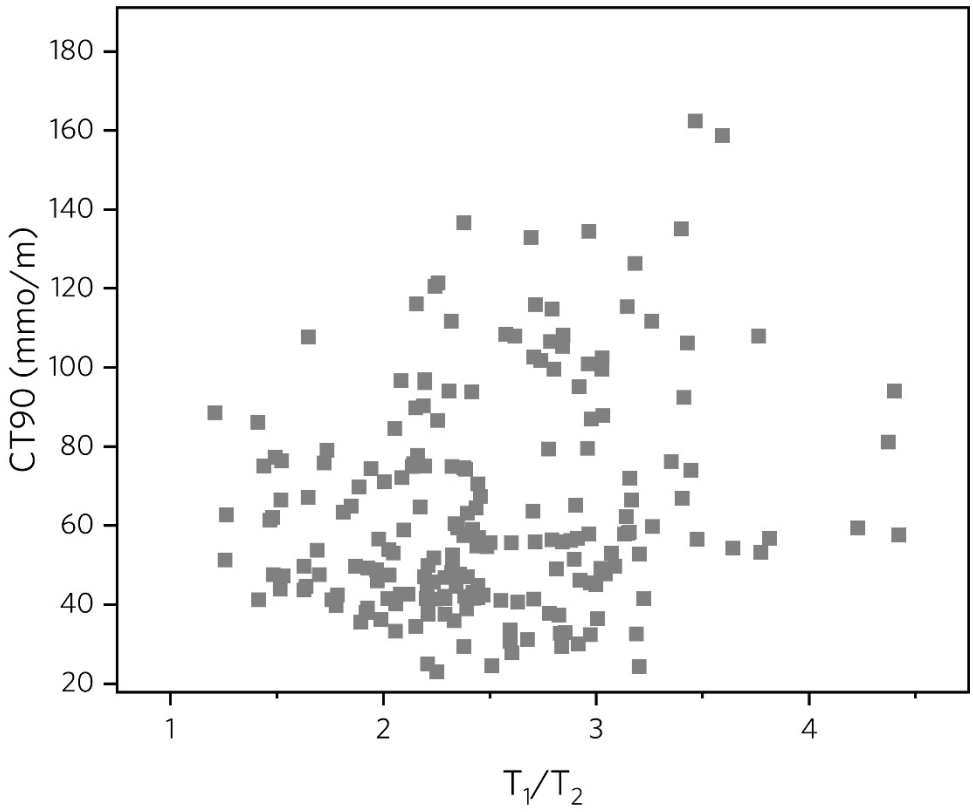

Figure 5.3 b)

Figure 5.3 a). Total gamma-ray (GRTO) plotted against T_1/T_2. Note that no general correlation between T_1/T_2 and GRTO can be visually recognized. b) 90 inches conductivity (CT90) plotted against T_1/T_2. Note that no general correlation between T_1/T_2 and GRTO or T_1/T_2 and CT90 can be visually recognized.

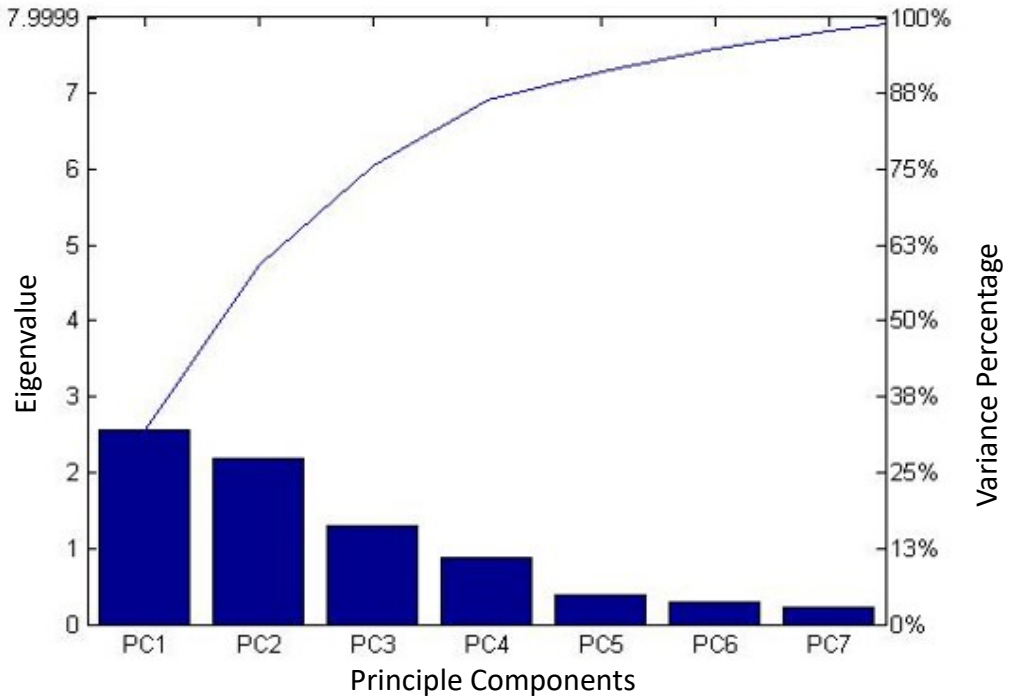

Figure 5.4. Pareto plot for PCA. Note that PC1 and PC2 only explain 59% of the total variation.

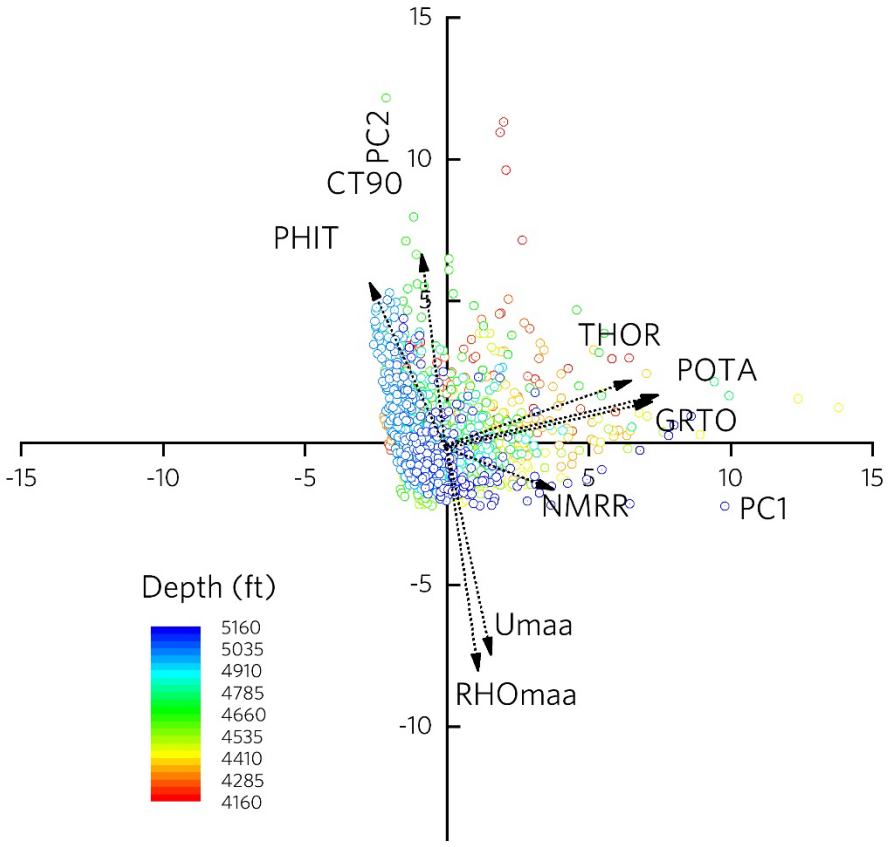

Figure 5.5. Cross plot of PC1 versus PC2, with depth of each point noted in color. Arrows are loading of eigenvectors for the dataset of the whole Arbuckle Group from (4160 ft to 5160 ft). Note that smaller angle between two loading vectors indicating the closer correlation between the input variables (logs) corresponding to loading vectors.

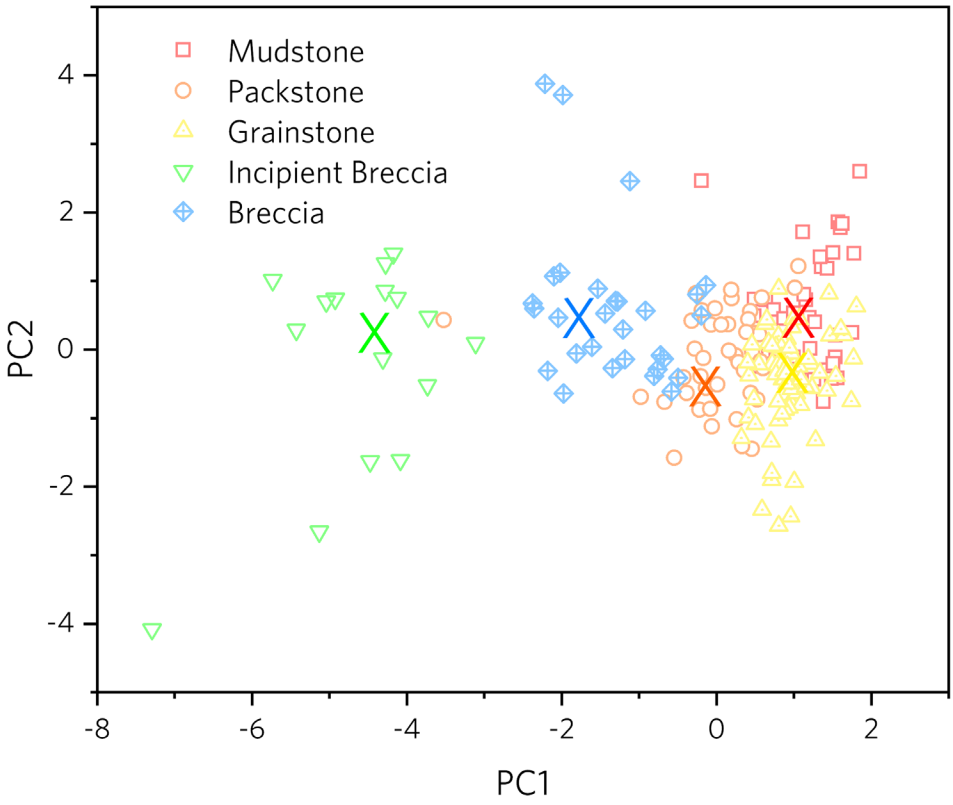

Figure 5.6. Score plot of PC1 and PC2 with classified clusters and cluster centers as the results of cluster analysis. Five clusters are marked in different colors and symbols. The cluster centers are presented as 'X' marks with the same color of belonging clusters. Interpreted electrofacies by the classification analysis are assigned to corresponding clusters. Note the clusters of mudstones, packstones and grainstones overlap considerably.

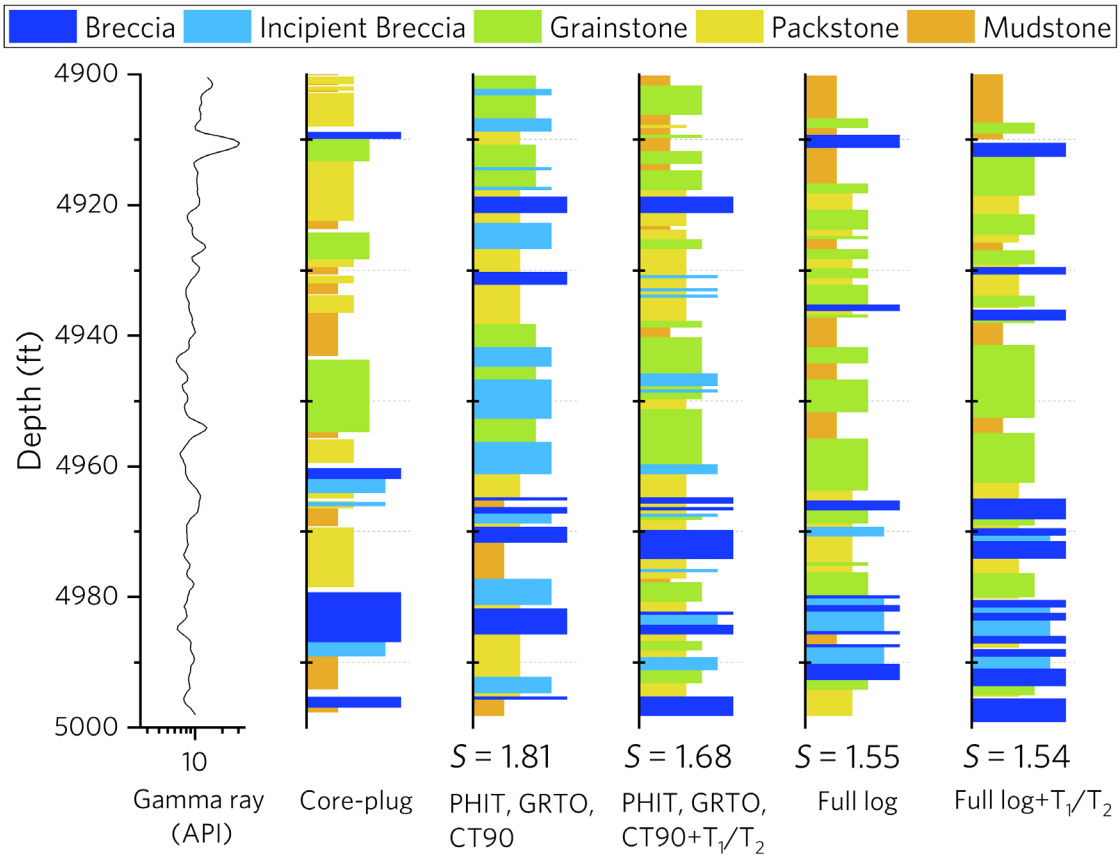

Figure 5.7. Comparison of Gamma-ray data, geologic lithofacies with eletrofacies predicted by alternative datasets, plotted against depth. a) Gamma-ray data. b) Geologic lithofacies determined from core observation. Note that all five lithologies are evident. c) Electrofacies predicted with Dataset 1 including PHIT, GRTO and CT90 with a recognition error S = 1.81. d - f) Electrofacies predicted with Dataset 2 (PHIT, GRTO, CT90, NMRR) with S = 1.68, 3 (PHIT, GRTO, CT90, *THOR, POTA,* ρ_{maa}, U_{maa}) with S = 1.55, and 4 (PHIT, GRTO, CT90, *THOR, POTA,* ρ_{maa}, U_{maa}, NMRR) with S = 1.54.

Table 4.1. Summary of whole data set. Information including lithofacies (grainstones, packstones, mudstones), depositional age (formation, period), range of drilling depth, sample size (diameter *d*, and height *h*), NMR estimated porosity, Air permeability with Klinkenberg-correction and total sample size of each lithofacies.

Lithofacies	**Formation**	**Period**	**Depth (feet)**	**Size as *d** *h*(mm)**	**Porosity (%)**	**K_{air} (mD)**	**Amounts**
Grainstone	Lancing-Kansas City	Upper-Pennsylvanian	2800.3-4600	2.54* 18.10-60.47	4.0-33.5	0.006-1134.3	41
Packstone	Arbuckle	Upper-Cambrian to	4299.1-5074.7	3.81* 19.58-50.38	1.4-10.4	0.001-297.2	5
Mudstone	Arbuckle	Lower Ordovician	4303-4446.5	3.81* 30.19-52.26	2.6-9.6	0.001-293.5	5

Table 4.2. The general geophysical data of all samples that have been tested. For each sample, the lithofacies, sample I.D., routine helium porosity and air permeability with Klinkenberg-correction (K_{air}) from special core analysis, NMR estimated porosity, characteristic T_2 value T_{2ML}, signal to noise ratio (SNR) of NMR test, real (σ') and imaginary (σ'') part of conductivity at 1Hz, recorded frequency range of SIP test are shown.

Lithofacies	Sample I.D.	Helium Porosity (%)	NMR Porosity (%)	Air Permeability (mD)	T_{2ML} (ms)	NMR SNR	Real conductivity (f=1Hz) (S/m)	Imaginary conductivity (f=1Hz) (S/m)	Frequency range (Hz)
	3	22.77	21.03	3.822	253.46	315.3	2.12E-03	1.13E-05	0.1-10k
	9	18.10	17.22	0.718	173.01	277.5	2.47E-03	2.26E-06	0.01-10k
	11	20.31	19.42	14.910	263.16	306.8	2.69E-03	7.10E-06	0.01-10k
	16	26.40	23.88	1.137	491.83	308.3	2.57E-03	3.25E-06	0.1-10k
	27	10.76	9.93	0.020	225.5	252.6	1.22E-03	1.55E-06	0.01-10k
Grainstones	37	19.99	20.17	0.338	457.6	319.6	2.11E-03	2.80E-06	0.01-10k
	38	24.55	18.27	0.128	274.73	261.2	2.57E-03	1.82E-06	0.01-10k
	39	23.87	22.47	1134.267	229.71	303	9.21E-03	1.20E-05	0.01-10k
	44	21.52	18.8	15.879	360.63	302.2	5.80E-03	7.28E-06	0.01-10k
	51	7.53	8.54	2.806	72.852	302.1	1.51E-03	4.26E-06	0.01-10k
	51b	5.98	15.43	0.012	37.397	267.6	4.87E-04	2.16E-06	0.01-10k

53	14.00	19.87	19.255	159.77	314.6	2.42E-03	1.79E-05	0.01-10k
57	20.11	10.21	3.447	254.9	300	3.31E-03	3.81E-06	0.01-10k
59	10.02	25.89	0.094	89.013	319	2.61E-03	3.08E-06	0.01-10k
64	26.68	19.51	15.891	438.26	311.2	4.27E-03	4.14E-06	0.1-10k
65	20.01	19.81	4.040	221.28	302.9	3.45E-03	6.42E-06	0.1-10k
66	21.02	19	3.906	255.06	315	3.04E-03	2.89E-06	0.01-10k
67	19.82	4.18	6.188	203.09	104.1	3.35E-03	5.49E-06	0.01-10k
69	2.46	7.75	0.006	5.066	301.2	8.30E-04	3.24E-06	0.01-10k
70	8.68	6.04	2.112	168.11	300.1	1.32E-03	7.83E-06	0.1-10k
71	4.15	5.32	0.002	40.603	320.8	1.04E-03	1.49E-06	0.01-10k
72	7.08	25.37	0.230	12.23	311	1.28E-03	8.75E-06	0.1-10k
81	25.58	17.85	50.360	292.83	311.5	6.43E-03	3.35E-06	0.1-10k
82	18.41	24.19	10.730	247.84	312.4	3.54E-03	2.20E-06	0.01-10k
85	24.08	21.56	22.369	315.14	334.5	4.46E-03	2.83E-06	0.01-10k
86	23.18	6.88	15.090	306.14	301.8	5.86E-03	2.71E-06	0.1-10k
89	5.73	30.7	0.010	11.047	276.6	6.95E-04	9.21E-06	0.1-10k
92	32.17	23.17	11.856	612.64	306.3	2.74E-03	4.18E-06	0.01-10k
101	25.32	30.94	5.076	261.94	292.7	3.71E-03	9.31E-06	0.01-10k
109b	22.46	18.74	22.538	398.22	263.9	3.29E-03	3.66E-06	0.01-10k
115	32.60	17.6	16.121	816.07	301.7	3.62E-03	5.65E-06	0.01-10k

	123	20.36	8.4	0.649	317.32	254.3	2.36E-03	4.70E-06	0.01-10k
	130	19.71	5.79	0.155	250	311.3	3.06E-03	2.16E-06	0.01-10k
	135	8.28	20.3	0.031	50.583	304.1	1.11E-03	1.28E-06	0.01-10k
	145	5.28	14.9	0.036	18.229	260.1	1.36E-03	7.49E-06	0.1-10k
	151	20.46	4.4	3.462	305.55	299.1	2.41E-03	4.08E-06	0.01-10k
	154	15.05	7.38	0.169	330.24	250.8	1.48E-03	3.87E-06	0.1-10k
	156	3.09	23.78	0.021	56.34	310.4	1.06E-03	2.37E-06	0.01-10k
	157	5.11	20.7	0.073	30.134	330	3.77E-03	5.68E-05	0.01-10k
	164	24.53	21.76	0.309	367.58	315.4	2.71E-03	1.82E-06	0.01-10k
	165	20.27	5.92	0.971	343.25	251.3	3.19E-03	7.12E-06	0.1-10k
	13-18	7.70	7.4	27.6	113.62	301	9.58E-03	3.19E-05	0.01-10k
	13-46	2.60	5.30	66.64	176.86	672	2.59E-03	1.68E-06	0.01-10k
Packstones	14-9	12.70	8.75	126.66	120.65	303.7	3.72E-03	1.64E-05	0.01-10k
	18-30	4.70	4.75	185.99	80.47	303.5	7.50E-03	1.45E-05	0.01-10k
	18-33	5.30	5.81	1.54	104.94	303.3	5.72E-03	1.36E-05	0.01-10k
	16-15	3.20	6.63	0.07	34.87	303	7.32E-03	4.24E-05	0.01-10k
	20-37	1.70	2.25	3.57	25.57	107	2.96E-03	6.87E-06	0.01-10k
Mudstones	30-4	3.40	3.76	0.06	23.18	302.1	2.36E-03	1.55E-05	0.01-10k
	30-24	2.80	3.03	12.82	19.03	300.7	2.01E-03	1.25E-05	0.01-10k
	33-25	11.80	12.94	4.62	253.69	426.8	1.58E-02	3.80E-05	0.01-10k

Table 4.3. The petrophysical properties that measured or calculated in this work. For the convenience of comparison, we repeat the lithofacies, sample I.D., NMR porosity and T_{2ML} here. Other petrophysical properties that discussed and listed here are the transverse surface relaxivity ρ_2 calculated from gas adsorption derived specific surface area, surface to volume ratio S_{por}, characteristic pore size Λ, tortuosity τ, formation factor F and cementation factor m and permeabilities calculated from K-C equation.

Lithofacies	**Sample I.D.**	**NMR Porosity** (%)	T_{2ML} (ms)	ρ_2 (μm/s)	S_{por} (/μm)	Λ (nm)	τ	F	m	**Permeability K-C equation** (mD)
Grainstones	3	21.03	253.46	2.57	1.32	1267.28	3.29	53.44	2.49	5.589
	9	17.22	173.01	2.24	2.89	865.04	2.81	51.81	2.10	1.368
	11	19.42	263.16	2.95	1.27	1315.82	2.61	35.34	2.17	8.213
	16	23.88	491.83	4.21	0.12	2459.13	3.71	54.35	2.91	51.429
	27	9.93	225.5	5.49	1.48	1127.51	2.18	68.92	1.58	0.272
	37	20.17	457.6	4.88	0.44	2288.00	3.97	75.19	2.77	15.845
	38	18.27	274.73	3.32	1.21	1373.67	2.49	37.47	2.02	2.837
	39	22.47	229.71	2.12	2.18	1148.56	1.73	11.80	1.80	33.620
	44	18.8	360.63	4.18	0.69	1803.14	2.28	25.89	2.02	32.665
	51	8.54	72.852	2.11	13.73	364.26	3.32	119.65	2.01	0.076
	51b	5.92	37.397	2.36	53.48	186.99	4.79	358.51	2.14	2.654
	53	15.43	159.77	2.76	6.26	798.87	2.81	48.32	2.14	11.254

57	19.87	254.9	2.12	1.96	1274.51	2.59	31.54	2.23	0.005
59	10.21	89.013	3.37	11.23	445.07	2.47	95.49	1.66	54.594
64	25.89	438.26	2.45	0.46	2191.28	2.80	29.10	2.57	6.701
65	19.51	221.28	2.78	2.26	1106.42	2.64	35.21	2.20	6.143
66	19.81	255.06	2.33	1.96	1275.28	2.68	36.04	2.22	9.540
67	19	203.09	0.31	2.46	1015.44	1.55	13.54	1.51	0.000
69	4.18	5.066	5.41	197.39	25.33	2.26	181.15	1.46	0.911
70	7.75	168.11	1.67	2.97	840.54	3.11	105.32	1.95	0.002
71	6.04	40.603	0.59	49.26	203.02	2.30	126.61	1.52	0.008
72	5.32	12.23	2.33	163.53	61.15	2.89	112.59	1.86	35.916
81	25.37	292.83	3.09	1.14	1464.17	2.35	21.08	2.28	3.850
82	17.85	247.84	2.67	2.02	1239.21	2.44	35.16	2.00	28.405
85	24.19	315.14	3.01	1.06	1575.72	2.50	25.66	2.30	23.398
86	21.56	306.14	0.40	1.09	1530.72	2.52	27.09	2.27	0.001
89	6.88	11.047	3.72	169.92	55.24	3.22	155.04	1.87	141.819
92	30.7	612.64	2.34	0.27	3063.22	3.46	35.79	3.27	11.257
101	23.17	261.94	4.94	1.27	1309.71	3.34	44.98	2.73	118.315
109b	21.76	398.22	3.74	0.63	1991.11	2.71	32.64	2.34	8.246
115	30.94	816.07	3.17	0.20	4080.36	4.46	62.08	3.63	1.201
123	18.74	317.32	1.50	1.05	1586.58	3.01	43.53	2.40	0.009

	130	17.6	250	0.83	2.00	1249.99	2.39	45.88	1.83	0.001
	135	8.4	50.583	3.26	39.54	252.92	2.92	122.81	1.81	11.257
	145	5.79	18.229	5.07	109.72	91.14	2.50	106.87	1.64	2.516
	151	20.3	305.55	3.34	1.09	1527.76	2.96	41.65	2.39	0.002
	154	14.9	330.24	1.00	1.01	1651.20	4.17	116.60	2.50	0.019
	156	4.4	56.34	3.20	35.50	281.70	2.80	195.82	1.64	26.118
	157	7.38	30.134	3.56	66.37	150.67	2.36	79.37	1.65	16.032
	164	23.78	367.58	3.86	0.91	1837.91	3.42	45.07	2.82	30.058
	165	20.7	343.25	1.61	0.73	1716.26	3.06	42.48	2.48	0.005
	13-18	7.4	113.62	0.69	13.20	54.52	3.59	174.34	1.98	37.352
	13-46	5.30	176.86	0.31	8.37	85.98	6.14	710.44	2.24	11.710
Packstones	14-9	8.75	120.65	0.79	11.52	62.47	3.08	108.40	1.92	110.255
	18-30	4.75	80.47	0.61	14.51	49.62	2.81	166.71	1.68	13.327
	18-33	5.81	104.94	0.58	14.14	50.91	2.71	126.87	1.70	27.579
	16-15	6.63	34.87	0.23	123.50	17.43	2.52	95.99	1.68	6.522
	20-37	2.25	25.57	0.08	168.41	12.78	1.44	91.71	1.19	0.707
Mudstones	30-4	3.76	23.18	0.16	185.79	11.59	3.10	255.08	1.69	0.493
	30-24	3.03	19.03	0.16	226.27	9.52	2.96	288.54	1.62	0.193
	33-25	12.94	253.69	0.08	16.97	126.84	1.96	29.63	1.66	2885.845

Table 5.1. Average values of calculated log responses including neutron porosity (*NPHI*), lateral log 90 inches conductivity (*CT90*), total gamma ray (*GRTO*), Potassium (*POTA*), Thorium (*THOR*), apparent matrix density (ρ_{maa}), matrix volumetric photoelectric absorption (U_{maa}), and T_1/T_2 (*NMRR*) for Arbuckle Group dolomite of interval 4900-5000 ft, well Wellington #1-32, Kansas. Lithofacies are discriminated based on core observation where MS=mudstone, PS=packstone, GS=grainstone, IB=incipient breccia, and BC=breccia.

Lithofacies (Based on core)	***NPHI* (%)**	***CT90* (.mmo/m)**	***GRTO* (.api)**	***POTA* (.ppm)**	***THOR* (.ppm)**	**ρ_{maa} (gm/cc)**	**U_{maa} (barns/cc)**	***NMRR***
MS	7.553	62.935	9.274	0.128	1.229	2.770	7.596	2.556
PS	7.847	63.429	9.659	0.144	1.096	2.774	7.786	2.502
GS	7.267	50.465	11.743	0.192	1.308	2.784	7.855	2.339
IB	6.272	76.566	9.238	0.150	1.381	2.764	7.492	1.834
BC	6.990	83.632	8.063	0.118	1.000	2.741	6.839	2.820

Table 5.2. Correlations (or loadings), eigenvalues and variances of Principal Component 1 to 8 referenced to neutron porosity (*NPHI*), lateral log 90 inches conductivity (*CT90*), total gamma ray (*GRTO*), Potassium (*POTA*), Thorium (*THOR*), apparent matrix density (ρ_{maa}), matrix volumetric photoelectric absorption (U_{maa}), and T_1/T_2 (*NMRR*) for Arbuckle Group dolomite of interval 4900-5000 ft, well Wellington #1-32, Kansas.

	Principal Components							
	PC1	**PC2**	**PC3**	**PC4**	**PC5**	**PC6**	**PC7**	**PC8**
NPHI	-0.200	-0.386	0.545	0.083	-0.626	0.227	-0.070	-0.242
CT90	-0.096	-0.451	0.514	0.012	0.687	0.049	0.028	0.219
GRTO	0.508	-0.161	-0.181	-0.194	0.064	0.799	-0.039	-0.044
POTA	0.538	-0.169	0.139	-0.070	-0.086	-0.330	0.713	-0.181
THOR	0.519	-0.204	0.096	-0.219	-0.118	-0.417	-0.651	0.140
$\boldsymbol{\rho_{maa}}$	0.113	0.531	0.420	-0.141	0.261	0.031	-0.172	-0.640
$\boldsymbol{U_{maa}}$	0.146	0.515	0.446	-0.080	-0.199	0.151	0.128	0.655
NMRR	0.316	0.070	0.042	0.936	0.048	0.040	-0.116	-0.012
Eigenvalue	2.616	2.162	1.326	0.824	0.374	0.301	0.218	0.179
Variance	0.327	0.270	0.166	0.103	0.047	0.038	0.027	0.022
Cumulative variance	0.327	0.597	0.763	0.866	0.913	0.950	0.978	1.000